A Digital Twin Development Framework for Fatigue Failure Prognosis of a Vertical Oil Well Drill String

by

© Mihiran Pathmika Galagedarage Don

(B.Sc., M.Sc., M.Eng.)

A Thesis submitted to the School of Graduate Studies in partial fulfillment of the requirement for the degree of

Doctor of Philosophy

October 2023

Memorial University of Newfoundland
Faculty of Engineering and Applied Science
Newfoundland and Labrador
Canada.

General Summary

Oil well drill strings, which are used to drill through the rock, are highly susceptible to sudden failure due to fatigue. This is caused by repetitive loading and unloading caused by excessive vibrations. Currently available technologies have some limitations in real-time detection of downhole vibrations to mitigate these conditions. The current study proposes a novel approach to identify the vibration types with their severities and estimate the remaining useful lifetime of the drill string based on various measurements made at the surface level. A computer algorithm is employed to classify them. Algorithms need to be trained to perform these types of tasks, ideally with real-world data. Nevertheless, these data are not widely available due to the limitations of the available technologies and various company policies. Therefore, the current study proposes using a simulation of the drill string to produce the necessary training data. This simulation is developed based on an approach called bond graphs which is very efficient in simulating dynamic systems. To make the bond graph ready to simulate a given drill string, it needs to be provided with certain parameters related to the geometry of the drill pipe, and the interaction with the drilling mud flow. They are determined through techniques called finite element method (FEM) and fluid-structure interaction (FSI) simulations, respectively. The customized Bond graph (BG) is then used to simulate the drill string for different 'what if' scenarios, and the synthesized data are used to train the aforementioned computer algorithm. Also, the bond graph provides the stress history that each drill pipe experiences during a particular period, and that stress history is used to estimate the remaining useful time of the drill string using an open-source software code. This entire workflow is termed a digital twin. This digital twin framework is applied for a laboratory-scale apparatus as a proof of concept and has also shown to be useful in decision-making to optimize the useful lifetime. This thesis presents three case studies. The first one emphasizes the benefit of using a non-linear fluid drag model over the static models currently used. The second case study uses a proposed fatigue damage estimation method as a tool to optimize the lifetime of drill collars by reducing fatigue damage. The third case study provides a proof of concept in using the proposed digital twin framework on a laboratory scale apparatus to determine fatigue damage by analyzing the surface level measurements.

Abstract

This thesis presents a novel methodology for fatigue life prognosis of vertical oil well drill strings through the development of a digital twin framework. A technique is proposed to classify vibration types with their severities and estimate the remaining useful lifetime of the drill string based on various indirect measurements made at the surface level. The classification was done using a machine learning algorithm developed based on a Hidden Markov Model (HMM). Training data for the algorithm were generated using a bond graph simulation of a vertical drill string. A three-dimensional lumped segment bond graph element and an interface element available in the literature were used to develop the simulation. The bond graph elements are developed based on a Newton-Eular formulation and body-fixed coordinates. The simulation was upgraded by introducing a fluid drag model and refining it with accurate element compliance values. Nonlinear fluid drag force statistical models were developed through the design of experiments (DoE) approach considering the nonlinear geometry of the drill pipes, the drilling fluid rheology, and fluid velocity. A series of fluid-structure interaction (FSI) simulations were employed to develop the statistical models for the lateral vibration damping and the axial drag force due to the drilling fluid flow through the pipe and the annular space. An apparatus was designed and fabricated to verify the FSI simulation. Further, a method was introduced to accurately determine the axial, shear, bending, and torsional compliances of geometrically-complex drill string segments represented by the bond graph elements. The trained HMM-based classifier using bond graph-generated training data selects the appropriate parameter set for the same bond graph to generate stress history for fatigue life prognosis. A generalized fatigue life estimation method was developed using SalomeMeca™, an open-source finite element analysis code. A detailed workflow for multi-axial, non-proportional, and variable amplitude (MNV) fatigue analysis is also provided. Three case studies are presented to demonstrate the significance of the nonlinear fluid drag models, the fatigue prognosis framework, and the digital twin development framework. In the first case study, the bond graph with the developed drag models showed higher stress fluctuations at the drill pipe threaded connection than the one with a static model. The second case study demonstrated the function of the proposed fatigue life prognosis framework as an optimization tool. In the case

study, the optimum placement of the stabilizers reduced the drill collar damage by 66% compared to the worst-case scenario. The third case study used a laboratory-scale vertical drillstring vibration simulator apparatus designed and fabricated to implement the framework as a proof of concept. It demonstrated the potential to use surface measurements to classify the vibration type and its severity for fatigue life prognosis.

keywords: *Bond graph, Cumulative fatigue, Oil well drill strings, Finite element method, Fluid-structure interaction, Digital twin*

Acknowledgements

My foremost sincere gratitude is expressed to my supervisor, Prof. Geoff Rideout, who gave me the opportunity, support, guidance, and encouragement to carry out this research. His vast wisdom and wealth of experience have inspired me throughout my studies and in my future career.

The invaluable feedback and encouragement given by Prof. Stephen Butt and the Drilling Technology Laboratory (DTL) members at Memorial University of Newfoundland (MUN) are also thankfully acknowledged, which greatly influenced my success. Thank you, Prof. Hodjat Shiri, for your support throughout by extending your kind advices and directions.

The financial support provided by the Natural Science and Engineering Research Council of Canada (NSERC) and MUN is also thankfully acknowledged. In addition to that, I would like to express my thanks to the Engineering Technical Services Team of MUN, for their immense support in fabricating the two apparatuses to conduct my experiments successfully.

A special thank goes to Mr. Maurizio Buggin, from Italy, who provided a magnificent support in getting familiar with the open-source Finite Element code.

Last but not least, I would like to convey my gratitude to Prof. Faisal Khan, Prof. George Mann, Prof. Oscar De Silva, Mr. Samith Rathnakayaka, Prof. Awantha Dewage Don, Prof. Thumeera Wanasinghe, and Mr. Dilhan Balage for their support at the beginning of my research journey.

I would like to also acknowledge that Chapter 3 and 4 of this thesis are already published content in International Conference on Bond Graph Modeling and Simulation (ICBGM) 2021, and Journal of Mathematical and Computer Modelling of Dynamical Systems respectively.

In conclusion, I would like to express my pardon if I have inadvertently omitted the name of those to whom thanks is due.

Mihiran Galagedarage Don

Dedication

To my loving parents, Somapala Galagedara & Indrani Colombage

To my loving wife, Lekshika

and my loving sons, Sanuka & Kenneth

Table of Contents

List of Figures

List of Tables

List of Abbreviations

ANN artificial neural network

API American Petroleum Institute

BHA bottom hole assembly

BG Bond graph

CFD computational fluid dynamics

DOE design of experiments

EM electromagnetic

FEA finite element analysis

FEM finite element method

FSI fluid-structure interaction

HMM hidden Markov model

ML machine learning

MP mud-pulse

MNV multi-axial, non-proportional, and variable amplitude

MWD measurement while drilling

ROP rate of penetration

RSM response surface method

WOB weight on bit

Chapter 1

Introduction

This chapter provides an overview of the problem addressed through this thesis and the solution approaches taken. The chapter begins with the motivation of the research, followed by the problem statement, the thesis statement, the list of contributions, and the organization of the thesis.

1.1 Motivation

Metallurgical and mechanical failures of drill strings are primarily due to fatigue crack propagation driven by severe vibrations [1]. Statistics show that fatigue causes more than 50% of drill string failures. As a result, drill string fatigue failure has drawn attention from academics worldwide [2, 3]. Threaded connections of the drill pipes and collars, shown in Figure 1.1, consist of high stress concentration sites due to their geometric features and hence are more susceptible to fatigue damage. Mechanical vibrations are the main cause of fatigue damage of drill strings. Although the commercially available down-hole measurement tools can pick up low-frequency vibrations, their limited bandwidth hinders the ability to rapidly detect high-frequency

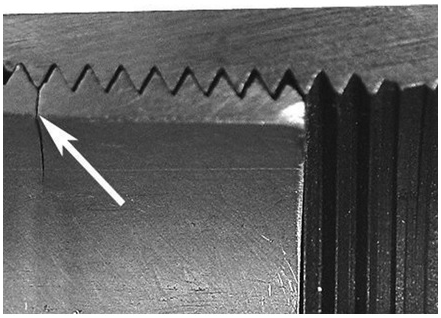

Figure 1.1: A fatigue crack initiated in an API pipe specimen [4]

vibrations. Moreover, the high-frequency content can get damped out while travelling to the surface along the drill string. Hence, there is a higher chance of misinterpreting a severe vibration as a smooth operation until a catastrophic failure occurs [5]. This leads to an increase in the overall risk of the drilling operation. On the other hand, drill string vibrations and shocks can limit the drilling performance, a critical problem in trajectory optimizing, wellbore design, and intelligent drilling [6, 7].

Although there are a number of attempts made to understand specific types of vibrations and how to avoid them [8], there is no evidence of a broader approach which simultaneously considers: well bore friction and impact; the influence of the drilling fluid on vibration damping; and fatigue life prognosis under multi-axial, non-proportional, and variable amplitude (MNV) load fluctuations. Despite the presence of discussions and numerous studies in the literature [9–11], an application of the digital twin concept for minimizing fatigue damage in a drill string, through the analysis of surface level measurements, has never been reported.

Figure 1.2 depicts a vertical well drill string. Mechanical vibrations occurring at the drill bit level can result in various indirect responses at the surface level. These responses include, but are not limited to, 1.) mechanical vibrations of the derrick, 2.) induction motor current, 3.) engine torque, 4.) rotary speed, and 5.) mud flow pressure fluctuations. In this thesis, they are designated as 'surface-level measurements'.

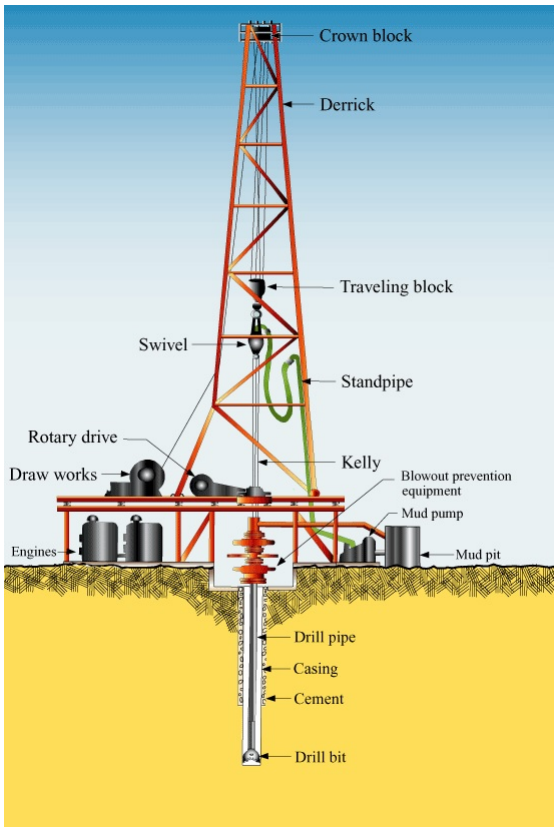

Figure 1.2: A vertical oilwell drillstring [12]

Assuming each response has three different characteristics A, B, and C, there is an opportunity to define the 3^5 number of different response combinations of the surface level measurements corresponding to different vibration states happening downhole. A technique that can distinguish between some combinations for critical vibration conditions has the potential to be developed into a useful tool that can rapidly detect downhole vibration conditions. This assists the driller in taking suitable mitigative actions to reduce the risk of a drill string failure.

This thesis addresses this challenge by developing a digital twin framework for vertical oil well drill strings, improving the parameterization of the simulation models required for digital twinning, and facilitating optimization of drillstring features such as stabilizer configuration for maximal fatigue life.

1.2 Problem statement

Fatigue is a significant cause of drill string failures [2, 3], drawing global attention from researchers. Rapid detection and estimation of the vibration type and its severity are essential because there is a risk of misinterpreting downhole severe vibrations as normal operation until a catastrophic failure happens [5]. However, existing downhole measurement tools have limitations in detecting high-frequency vibrations [13].

The inability to detect severe vibrations and avoid a drill string failure may cause the driller's financial loss of millions of dollars due to fishing operations, nonproductive time, bottom hole assembly lost in hole, and tool replacements. This affects the entire set of project stakeholders and hence must be avoided [14, 15].

The literature proposes indirect measurement approaches for rapid drill string vibration detection based on machine learning techniques [16]. Nevertheless, there is a very limited training data available to be used by the researchers as a result of the current industrial data sharing practices [17]. Training data can be generated using a drill string simulation model considering the well bore interactions, drilling fluid interactions, and other drill string dynamics. Analytical models have limitations due to the complexity of the phenomena [18–21] involved, while multi-physics FEM simulations suffer from the computational cost. BG simulations have been introduced to be efficient and successful in this context, with some potential upgrades, such as incorporating fluid drag models.

This thesis investigates the problem of simulation-enabled vibration characterization of drill strings, and subsequent fatigue failure prognosis, using practical surface-level measurements. The thesis will develop a digital twin framework to address this problem, using BG, fluid-structure interaction simulation, finite element modeling, and machine learning.

1.2.1 Thesis statement

To reach this goal, first, the high-level efficient BG simulations need to be employed with a systematic parameterization approach to refine them with realistic element compliance values. Secondly, the BG simulations need to be upgraded with fluid drag models in order to capture the spectrum of real-world vibration conditions. Thirdly, a fatigue life prognosis method needs to be introduced using BG and finite element method (FEM) combined approach for MNV loading conditions. Finally, a digital twin framework needs to be developed by integrating the first three solutions and further strengthened with the surface-level monitoring feature.

The following objectives were set with the defined tasks presented under each objective.

Objective 1 Develop 2D and 3D multi-body BG models with realistic drill string parameters.

- Task 1: Develop a methodology to quantify the structural properties of any given drill pipe with finer details based on a FEM based approach.
- Task 2: Develop a methodology to quantify the lateral vibration damping and axial drag effects exerted on a drill pipe by the drilling fluid based on a fluid-structure interaction (FSI) simulation approach with experimental verification.

Objective 2 Develop a methodology to estimate the cumulative fatigue damage of a drill pipe for MNV loading conditions.

- Task 3: Use the BG model to generate the stress history of a given drill pipe in a vertical well and the prognosis of the remaining lifetime using a FEM approach for MNV loading conditions.

- Task 4: Optimize the placement of the drillstring stabilizers to minimize the vibration damage of drill collars.

Objective 3 Create a digital twin for a laboratory-scale apparatus that can be adapted for a specific vertical well drillstring, enabling estimation of the remaining fatigue life of a drill pipe or drill collar.

- Task 5: Design and fabrication of an experimental apparatus to demonstrate stick-slip, bit bounce, and whirling vibrations.
- Task 6: Validation of the BG model using the experimental apparatus
- Task 7: Use the refined and validated BG to train a machine learning algorithm for real-time classification of vibration states of the drill string.
- Task 8: Develop a digital twin of the experimental apparatus which is adaptable to a given scenario and dynamically determine the stress history based on the vibration measurements taken at the 'surface level'.

1.2.2 Contributions

At the successful completion of the defined tasks in Section 1.2.1, the following main contributions were made.

- Contribution 1: A digital twin framework to predict the type and severity of downhole vibrations using practically-available surface level measurements. The framework used a BG simulation model to generate training data for a machine learning algorithm developed based on HMM.
- Contribution 2: a 'cascaded modelling' approach to improve the parameter estimation for simulation models that are required for the digital twinning process.

High-order models of complex components generated improved stiffness and fluid damping parameters, which were then used in computationally efficient reduced-order top level models.

- Contribution 3: A simulation-based fatigue prognosis and optimization method. Efficient lumped-segment BG simulations were coupled with design of experiments (DOE) to determine optimal stabilizer location for improved vibration response and fatigue life

1.3 Organization of the thesis

This is a manuscripts-based thesis and the first two chapters are allocated for the introduction and the literature survey. Chapter 2 provides the essence of the in-depth literature surveys presented in future chapters. The main contributions are presented from Chapter 3 to Chapter 6 while the conclusion and further research opportunities are presented in Chapter 7.

Figure 1.3 illustrates the overview of the content and the respective publication. The contributions of Chapters 3 to 5 are utilized in the digital twin framework development in Chapter 6 in addition to the introduction of surface monitoring feature using the vibration simulator apparatus. Chapters 3, 5, and 6 also present case studies of the respective contributions of the chapter.

1.4 Publications

(1) M. Galagedarage Don and G. Rideout, "*An experimentally-verified approach for enhancing fluid drag force simulation in vertical oilwell drill strings*", Mathematical and Computer Modelling of Dynamical Systems, vol. 28, no. 1, pp. 197–228, 2022.

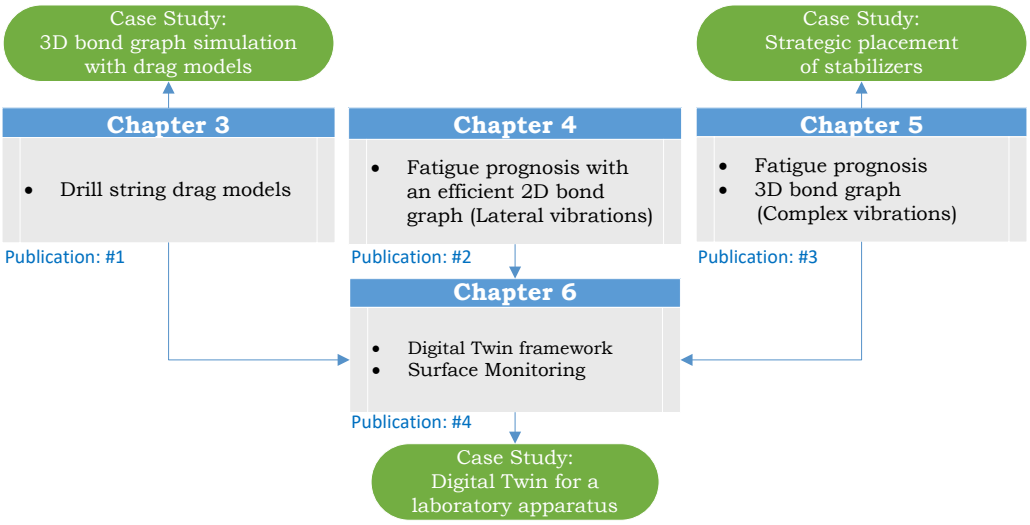

Figure 1.3: The organization of the thesis

(2) M. Galagedarage Don and Geoff Rideout, "*Fatigue Failure Prognosis of an Oil Well Drill String Using a Lumped Segment BG Model and Finite Element Method*". 14th International Conference on BG Simulations (ICBGM')2021 Nov 8-10, 2021- San Diego, California USA.

(3) M. Galagedarage Don and Rideout, G., "*Fatigue Life Prognosis of an Oil Well Drill String Using Cascaded Dynamic Models*". Engineering Failure Analysis, Elsevier [Under review]

(4) M. Galagedarage Don and Rideout, G., "*A digital twinning methodology for vibration prediction and fatigue life prognosis of vertical oil well drillstrings*". IEEE Access, [Under review]

References

[1] M. Albdiry and M. Almensory, "Failure analysis of drillstring in petroleum industry: a review," *Engineering Failure Analysis*, vol. 65, pp. 74–85, 2016.

[2] C. Bu, J. Xiao, S. He, and M. Wiercigroch, "Theoretical study on fatigue damage of sonic standing wave resonant drill-string," *Journal of Petroleum Science and Engineering*, vol. 220, p. 111160, 2023.

[3] K. Macdonald and J. Bjune, "Failure analysis of drillstrings," *Engineering Failure Analysis*, vol. 14, no. 8, pp. 1641–1666, 2007.

[4] J. Van Wittenberghe, T. Galle, W. De Waele, and P. De Baets, "Experimental analysis of the fatigue life of threaded pipe connections under cyclic bending," *International Journal of Sustainable Construction and Design*, vol. 3, no. 2, 2012.

[5] Z. Zhang, Y. Shen, W. Chen, J. Shi, W. Bonstaff, K. Tang, D. Smith, Y. Arevalo, B. Jeffryes, *et al.*, "Continuous high frequency measurement improves understanding of high frequency torsional oscillation in north america land drilling," in *SPE Annual Technical Conference and Exhibition*, Society of Petroleum Engineers, 2017.

[6] G. Dong and P. Chen, "A review of the evaluation, control, and application technologies for drill string vibrations and shocks in oil and gas well," *Shock and Vibration*, vol. 2016, 2016.

[7] M. Kapitaniak, V. V. Hamaneh, J. P. Chávez, K. Nandakumar, and M. Wiercigroch, "Unveiling complexity of drill–string vibrations: Experiments and modelling," *International Journal of Mechanical Sciences*, vol. 101, pp. 324–337, 2015.

[8] V. Vaziri, M. Kapitaniak, and M. Wiercigroch, "Suppression of drill-string stick–slip vibration by sliding mode control: Numerical and experimental studies," *European Journal of Applied Mathematics*, vol. 29, no. 5, pp. 805–825, 2018.

[9] M. Samnejad, M. Gharib Shirangi, R. Ettehadi, *et al.*, "A digital twin of drilling fluids rheology for real-time rig operations," in *Offshore Technology Conference*, Offshore Technology Conference, 2020.

[10] M. Gholami Mayani, R. Rommetveit, S. I. Oedegaard, M. Svendsen, *et al.*, "Drilling automated realtime monitoring using digital twin," in *Abu Dhabi International Petroleum Exhibition & Conference*, Society of Petroleum Engineers, 2018.

[11] M. G. Mayani, M. Svendsen, S. Oedegaard, *et al.*, "Drilling digital twin success stories the last 10 years," in *SPE Norway One Day Seminar*, Society of Petroleum Engineers, 2018.

[12] M. Khalifeh, A. Saasen, M. Khalifeh, and A. Saasen, "Different categories of working units," *Introduction to Permanent Plug and Abandonment of Wells*, pp. 137–163, 2020.

[13] H. Mostaghimi, J. R. Pagtalunan, B. Moon, S. Kim, and S. S. Park, "Dynamic drill-string modeling for acoustic telemetry," *International Journal of Mechanical Sciences*, vol. 218, p. 107043, 2022.

[14] O. Ozguc, "Analysis of fatigue behaviour of drill pipe on pin-box connection," 2021.

[15] A. Ambrus, P. Ashok, D. Ramos, A. Chintapalli, A. Susich, T. Thetford, B. Nelson, M. Shahri, J. McNab, and M. Behounek, "Self-learning probabilistic detec-

tion and alerting of drillstring washout and pump failure incidents during drilling operations," *Society of Petroleum Engineers - IADC/SPE Drilling Conference and Exhibition, DC 2018*, vol. 2018-March, pp. 6–8, 3 2018.

[16] Y. Zha and S. Pham, "Monitoring downhole drilling vibrations using surface data through deep learning," in *SEG Technical Program Expanded Abstracts 2018*, pp. 2101–2105, Society of Exploration Geophysicists, 2018.

[17] T. R. Wanasinghe, L. Wroblewski, B. K. Petersen, R. G. Gosine, L. A. James, O. De Silva, G. K. I. Mann, and P. J. Warrian, "Digital twin for the oil and gas industry: Overview, research trends, opportunities, and challenges," *IEEE Access*, vol. 8, pp. 104175–104197, 2020.

[18] B. J. J. and I. Finnie, "An analytical study of drill-string vibration," *Journal of Engineering for Industry*, vol. 82, pp. 122–127, 5 1960.

[19] S. Chen, "Fluid damping for circular cylindrical structures," *Nuclear Engineering and Design*, vol. 63, no. 1, pp. 81–100, 1981.

[20] W. Tucker and C. Wang, "An integrated model for drill-string dynamics," *Journal of sound and vibration*, vol. 224, no. 1, pp. 123–165, 1999.

[21] M. P. Paidoussis, *Fluid-structure interactions: slender structures and axial flow*, vol. 1. Academic press, 1998.

Chapter 2

Literature Review

This chapter overviews the detailed literature surveys presented in Chapters 3 to 6. Fatigue failure of drill strings, bond graph approach in drill string simulation, fatigue life estimation techniques, and digital twins are discussed in this chapter.

2.1 Fatigue failure

Metal components experience repeated loading and unloading or cyclic stresses in numerous engineering applications. Despite being exposed to stresses below the yield stress, this increases the chances of component failure. Such failures are commonly known as 'fatigue failures'.

Fatigue failure occurs in three main stages: initiation, propagation, and failure. When a component has areas with high stress concentration, either due to design flaws or geometry, those areas become more susceptible to developing cracks. Imperfections in the material, such as voids; inclusions; or hard particles, can also create stress fields. Residual stresses can result from uneven heating and cooling during manufacturing, while surface damages can be caused by improper handling and corrosion, leading to

crack initiation. During operation, the crack propagates through repeated loading and unloading, with tensile loads accelerating its growth by facilitating crack opening. If the stress on the component exceeds its endurance limit, the component will fail after a certain number of cycles. In the context of a rail, the stages of fatigue failure are illustrated in Figure 2.1, with point A representing the fracture initiation region and regions B and C showing crack propagation and sudden failure regions, respectively [1, 2].

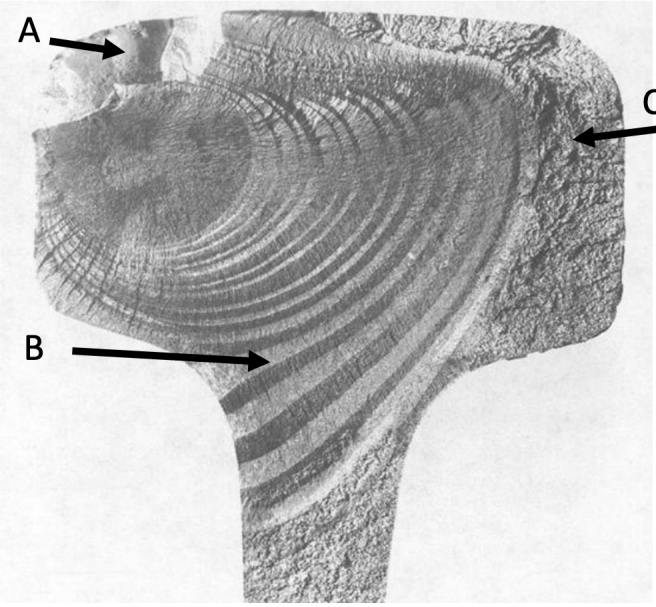

Figure 2.1: Nature of fatigue failure fracture surface [3]

2.1.1 Fatigue failure of oil well drill strings

Drill strings are widely used in industries such as oil and gas and geothermal energy. Rotary drilling is the most common type of drilling technique used in the oil and gas industry [4]. Severe vibrations of the drill string create complex stress fluctuations, which lead to structural failure due to fatigue. Drill pipe and collar failure carry enormous risks to the overall project due to the high degree of consequences [5]. Drill pipe

threaded connectors are particularly vulnerable to high stress concentration leading to initiation and propagation of fatigue cracks [6–8] which can get accelerated due to various downhole chemical and physical conditions [9]. A drill pipe failure may result in a costly fishing operation, side-tracking or re-drilling to follow an alternative path, completing the well at a shallower depth than originally planned, or even abandoning the well. Therefore, taking precautions to avoid drill string fatigue failure is essential. Consequently, preventive techniques are highly demanded in the industry [10].

2.1.2 Different drill string simulation approaches

The determination of the stress history that a drill string has been exposed to is a crucial step in fatigue life prognosis. Several types of attempts are reported in the literature and can be categorized under mathematical models [11–13], numerical models [14–17], and physical models [18, 19].

Mathematical models often use simplifying assumptions; hence including the entire complexity of the drill string vibration may not always be feasible. Also, the complex interactions with the well bore and complex damping phenomena [20] cannot be conveniently integrated. On the other hand, numerical techniques such as transient FEM also carry a large computational burden, making them inefficient to apply in design applications [14]. On the other hand, physical modelling involves costly initial investments and additional operational costs in running experiments for different drill pipes. Considering all those facts, the drill string simulation using the bond graph approach is identified as an efficient alternative [14, 15].

2.1.3 Drill string simulation using bond graph

2.1.3.1 The bond graph formalism

Bond graph simulation environment provides a common platform for the natural phenomena to represent them in terms of interactions of generalized elements such as energy storage C and dissipators R, inertia I, transformers TF, gyrators GY, and power conserving junctions. Energy plays the role of 'common currency' [21] hence the mechanical, electrical, thermal, and hydraulic systems can be unified by the fact that their components exchange energy [22] through 'Energy Ports'. The system interacts with its surroundings using sources of effort Se and flow Sf ports. In other words, bond graph modelling can be considered as an analogous approach to solve technological problems in various domains as mentioned in [23]. There are two generalized power variables, $effort(e)$ and $flow(f)$ which are the time derivatives of generalized $momentum(p)$ and $displacement(q)$, the product of which is power.

Further, the power conserving $0-junction$ and $1-junction$ model Kirchoff's node and loop laws, respectively. Efforts at $0-junctions$ sum to zero while flows are identical along all the bonds connected to the $1-junction$ and vice versa. The algebraically positive power flow is indicated with a half arrow while the short perpendicular line segment to the bond indicates the causal stroke which means whether the effort or flow is the input or output from the constitutive law of the connected element. The powerless signal flow is denoted by a full arrow such as angular speeds and orientation angles. A systematic learning aid of the bond graph concepts is presented in [22].

2.1.3.2 Currently available bond graph drillstring models and their potential improvements

Accurate determination of element stiffness values

Several drill string simulation contributions are available in the literature developed using the bond graph approach [14, 15, 24, 25]. They are highly efficient in simulating wellbore interactions and other vibration types in comparison with most of the currently available numerical drillstring simulations. A three-dimensional bond graph element is employed with an interface element, illustrated in Figures 2.2 and 2.3, to develop the lumped segment models of vibrating drill strings in three-dimensional space. The Newton-Euler formulation and body-fixed coordinate system are the foundation of the two sub-models. The lumped segment model is developed by introducing compliance (reciprocal of the stiffness) values in between two three-dimensional elements which are conceptually illustrated in Figure 2.4. The axial, bending, and shear compliances are illustrated while the torsional compliance can be illustrated in a similar manner to the bending compliance but with the spiral spring fixed in an orthogonal plane. The bond graph models are currently parameterized based on the theoretical calculations of stiffness values, shear; bending; axial; and torsional, approximating the drillstring to a tubular structure [26, 27]. This introduces an error in the simulation which makes the simulation less accurate in determining the vibration characteristics.

Usually, the manufacturer specification of a drill pipe contains details on Elastic Modulus, Yield Point, Tensile Strength, Impact Strength, and Hardness only. Theoretical calculations can be performed to evaluate the compliance values using the equations 2.1 to 2.4 respectively which becomes impractical when it comes to threaded

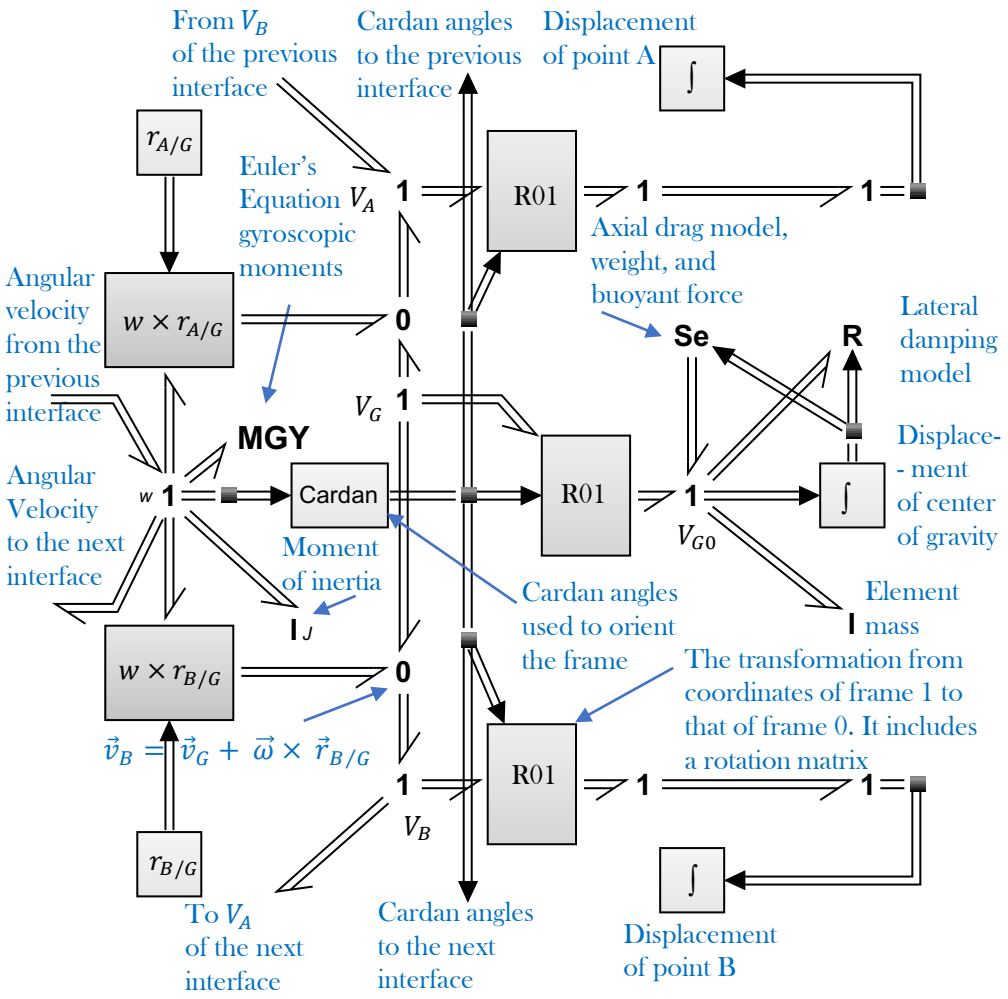

Figure 2.2: 3D bond graph element

connections and the transition region between the connection and the pipe.

$$C_s = \frac{l}{\kappa G A} \tag{2.1}$$

$$C_a = \frac{l}{EA} \tag{2.2}$$

$$C_b = \frac{l}{EI} \tag{2.3}$$

$$C_T = \frac{l}{GJ} \tag{2.4}$$

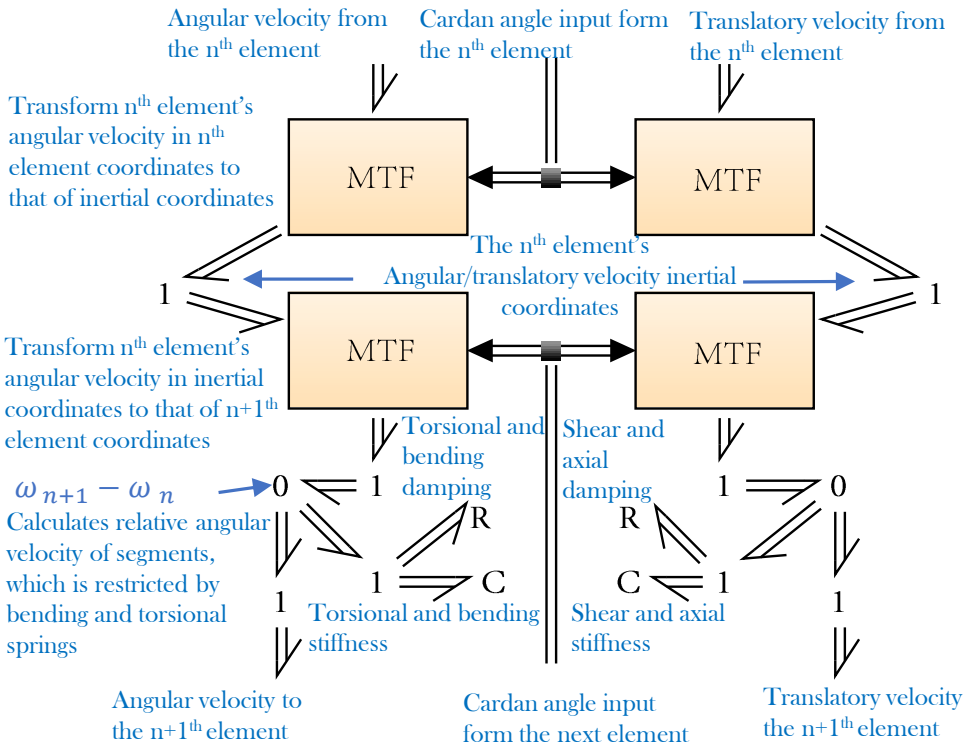

Figure 2.3: Interface between elements

where C_s, C_a, C_b, C_T are shear, axial, bending, and torsional compliances respectively; l is the length of the beam, κ is the shear coefficient, G is the shear modulus, E is the Young's Modulus, A is the cross-sectional area, I is the area moment of inertia, and J is the polar moment of inertia.

The threaded joint regions consist of complex geometries and frictional contacts, which may cause deviations from the theoretical results with simplifying assumptions. The effect of these factors needs to be investigated, and the bond graph parameters need to be refined accordingly. Further, a systematic procedure that can be adapted to determine the stiffness parameters of any slender structure with complex geometries, such as drill pipes and collars, needs to be introduced. Further background information is presented in Chapters 4 and 5.

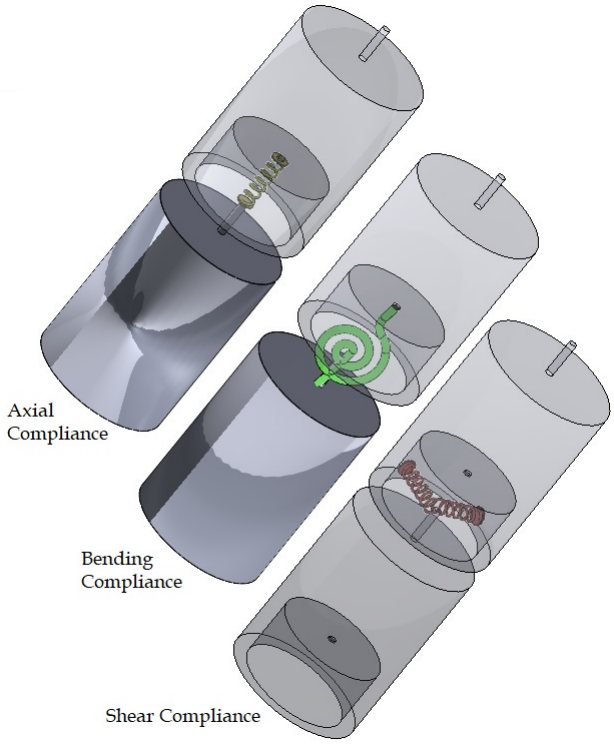

Figure 2.4: BG element compliances

Modelling of fluid drag phenomena on drill string

There are numerous studies available in the literature on dynamic models of drill strings [28–30]. A common feature of the available models is that they simulate a selected limited number of phenomena using mathematical or simulation approaches. None of them provide a methodology to determine the damping coefficient for a given Newtonian or non-Newtonian fluid and a drill pipe geometry. Hence a detailed study of the fluid damping due to drilling fluid and its variations due to other parameter changes is an open research topic.

As stated above, almost all the mathematical and numerical models available in the literature either do not consider the fluid drag effect or use a constant value of fluid drag to represent it. Nevertheless, [31–34] have shown that the drilling mud

flowing through the drill string and the annular space governs the lateral vibration damping of the drill string. This factor has to be considered in further developing the bond graph. An experimental and/or simulation-based statistical drag model needs to be developed to incorporate the lateral vibration damping and the axial drag effects into the bond graph. Lateral vibration is directly related to drill string fatigue life. In contrast, weight on bit (WOB) is indirectly related to stick-slip and bit bounce vibration, which contribute to fatigue damage of the drill string. A FSI simulation can be employed to investigate this damping phenomenon [35]. The drilling fluid can be modelled as a Herschel Bulkley fluid in a commercial multi-physics software [36]. The Herschel Bulkley model is given in Equation 2.5.

$$\tau = \tau_0 + \kappa \dot{\gamma}_c^n \tag{2.5}$$

where τ is the shear stress, τ_0 is the yield stress, n is the power law index, κ is the consistency index, and $\dot{\gamma}_c$ is the critical shear rate.

The damping effect depends on a variety of factors such as flow speed, radial clearance, well-depth, and the rheology of the drilling fluid. These changing parameters can cause a mass effect or a stiffness effect on the drill pipe. For example, the presence of drilling fluid creates an added mass effect compared to dry conditions. Hence the natural frequency will be lower when the pipe is immersed in a stationary drilling fluid. On the other hand, when a fluid flow is established, the pipe will experience a resistance to displace from the equilibrium state. This introduces a spring effect which increases the natural frequency. A displacement-time graph of a vibrating mass, illustrated in Figure 2.5, can be taken through a physical experiment or an FSI simulation from which the natural frequency (ω_n) and damping ratio (ζ) can be determined using the Equations 2.6 to 2.9.

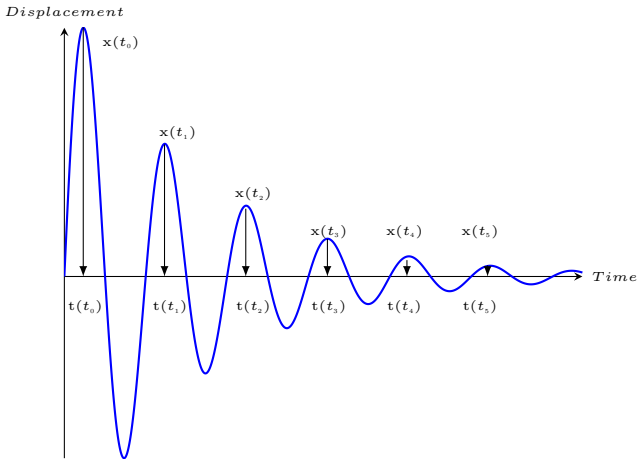

Figure 2.5: Decaying oscillation of a spring mass damper system

$$T = \frac{t_n - t_0}{n} \tag{2.6}$$

$$\delta = \frac{1}{n} \log \left(\frac{x(t_0)}{x(t_n + 1)} \right) \tag{2.7}$$

$$\zeta = \frac{\delta}{\sqrt{4\pi^2 + \delta^2}} \tag{2.8}$$

$$\omega_n = \frac{\sqrt{4\pi^2 + \delta^2}}{T} \tag{2.9}$$

where T is the periodic time, δ is the logarithmic decrement, ζ is the damping ratio, and ω_n is the natural frequency.

A design of experiment (DoE) approach can be employed to develop the mathematical model to be implemented in the bond graph model. Further detailed background information is presented in Chapter 3.

2.1.4 Fatigue life prediction methods for multi-axial, non-proportional, and variable amplitude (MNV) loading

The very first experimentally validated variable amplitude, multi-axial and non-proportional fatigue estimation is presented by [37]. Their study is based on the critical plane concept. The input data is taken from strain gauge rosettes and analytical strain data. A computer model is developed to identify the plane with maximum damage called the critical plane. The damage that occurs in an arbitrary plane is quantified by Rainflow counting on the respective plane. Critical multi-axial damage models are used appropriately, and finally, the damage is accumulated throughout the total loading history.

A technique for monitoring and detecting the critical planes is presented by [38]. The method they introduce, 'Multi-axial Rainflow', does not limit the user to examine the rain flow on the coordinate system but in any direction.

A software tool is developed by [39], which can handle fatigue life (N_f) estimations due to multi-axial, random, and non-proportional loading conditions. This method is named 'IS Method' and has been verified with the Mansion-Coffin Equation.

All three techniques mentioned above are not practical to use in the current study due to the unavailability of software codes in the public domain. Meanwhile, the commercial finite element analysis (FEA) codes with the ability to accept MNV loading conditions for fatigue analysis are not accessible to most of the researchers. Therefore, the use of open-source software is an ideal alternative.

Using open-source software is advantageous in many ways. The main strength is that they are freely available and can be used for any commercial or research work without cost. Also, they can run on cloud servers, so a lot of computation power can be used. Concurrently, there are some challenges in going open source because the

user has to identify the source code and understand how to make it run, which is not straightforward. SalomeMeca™ is an open-source FEA code which has the capability to estimate fatigue damage due to MNV loading conditions. Salome™ is the facilitator of a generic platform for pre-and-post processing of numerical simulations. It does not provide any codes related to calculations. On the other hand, CodeAster™ is an open-source FEA Code. In CodeAster™, the modules are coded in Python™, while the software's core is developed on FORTRAN™. SalomeMeca™ hosts CodeAster™ and Salome™ to create a standalone application. Here, the CodeAster™ solver gets integrated with the Salome™ platform. SalomeMeca™ is equipped with tools for creating the geometry (Geometry module), meshing (Mesh Module), Solving (Aster Study), and post-processing (ParaVis™) [40].

Considering the above facts, SalomeMeca™ can be identified as the most suitable option to carry out the fatigue life prognosis based on performance and availability. The stress fluctuation can be given in as a time series for bending in two orthogonal planes, shear in two orthogonal planes, torsion, and axial tension and compression. The load fluctuation data in each plane is subjected to 'rain flow counting', and the sum of the fatigue damage is calculated.

SalomeMeca™ offers a diverse range of options to calculate fatigue damage. Among the other fatigue calculation methods such as: `MANSON_COFFIN; TAHERI_MANSON;` and `TAHERI_MIXTE`, `WOHLER` method stands out as a suitable option for high cycle and multi-axial fatigue calculations. Wöhler's Diagram (S-N Curve) can be defined at the point of the definition of the material and used to evaluate the remaining lifetime in number of cycles. For a stress-type loading history, the number of cycles to failure is determined by interpolating the Wöhler curve of the material at a given level of alternating stress. Each elementary cycle corresponds to a specific stress amplitude ($\Delta\sigma = |\sigma_{max} - \sigma_{min}|$) and an alternating stress ($S_{alt} = 1/2\Delta\sigma$). To introduce the

Wöhler curve of the material, it needs to use the `DEFI_MATERIAU` operator. There are three possible forms for specifying the Wöhler curve: Discretized point-by-point function; Analytical form of Basquin; and "Current zone" form. These forms allow defining the Wöhler curve for the material, which is necessary for calculating the number of cycles to failure and determining the damage for a given stress-type loading history. Further detailed information is presented in Chapter 5 [41].

2.1.5 Digital twins

According to [42], the concept of 'digital twin' was first introduced by Michael Grieves at the University of Michigan in 2003. As mentioned in [43], a digital twin is

"an integrated multi-physics, multi-scale, probabilistic simulation of an as-built system, enabled by digital thread, that uses the best available models, sensor information, and input data to mirror and predict activities or performance over the life of its corresponding physical twin".

Meanwhile, [44] confirms that this is the currently available broadest definition of the term 'digital twin'.

A digital twin concept is presented by [45], highlighting potential opportunities and challenges associated with digital twin applications in the civil aerospace industry. The prediction of the structural life of specific aeroplane parts based on sensor data and other inputs while in operation is further explained. This concept can be employed in predicting the remaining fatigue life of a drill string.

Currently, there are some major limitations in near real-time high-frequency vibration data logging while drilling due to bandwidth limitations [46, 47]. Real-time, or more realistically 'near real-time data', in a wide frequency spectrum is one of the most essential factors required to implement a digital twin of a drill string with the

ability of fatigue life prognosis. A digital twin that assists in surface-level response monitoring of a drillstring has the potential to solve this problem.

Many researchers have attempted surface-level monitoring of drill string vibrations since the 1960s [48]. The bit wear estimation through surface-level monitoring has been explored by [49] and [50], which requires downhole measurement data for algorithm training. The studies presented in [51] and [52] also require the downhole measurements at some point in the training process. There is no evidence available in the literature on training algorithms for surface monitoring using drillstring simulations which considers dynamics and interactions with the drilling fluid and wellbore.

Among the numerous possible options for machine learning algorithms, hidden Markov model (HMM) is a suitable option to be used as a classification algorithm of different downhole vibrations through surface-level monitoring. The measurements, such as axial and lateral accelerations, motor current fluctuation, rotational speed, and drilling fluid flow rate and pressure pulses, can be used as inputs to a trained HMM algorithm to classify different vibration scenarios. The algorithm training can be done using the drillstring simulation for different vibration conditions and their severity levels. Further detailed background information is presented in Chapter 6.

References

[1] R. I. Stephens, *Case studies for fatigue education*, vol. 1250. ASTM International, 1994.

[2] W. F. Smith, J. Hashemi, and F. Presuel-Moreno, *Foundations of materials science and engineering*, vol. 509. McGraw-hill New York, 2006.

[3] R. Rice and R. Rungta, "Fatigue analysis of a rail subjected to controlled service

conditions," *Fatigue & Fracture of Engineering Materials & Structures*, vol. 10, no. 3, pp. 213–221, 1987.

[4] A. Sapińska-Śliwa, R. Wiśniowski, M. Korzec, A. Gajdosz, and T. Śliwa, "Rotary-percussion drilling method-historical review and current possibilities of application," *AgH Drilling, oil, gas*, vol. 32, no. 2, pp. 313–323, 2015.

[5] A. Ambrus, P. Ashok, D. Ramos, A. Chintapalli, A. Susich, T. Thetford, B. Nelson, M. Shahri, J. McNab, and M. Behounek, "Self-learning probabilistic detection and alerting of drillstring washout and pump failure incidents during drilling operations," *Society of Petroleum Engineers - IADC/SPE Drilling Conference and Exhibition, DC 2018*, vol. 2018-March, pp. 6–8, 3 2018.

[6] W.-C. Chen, "Drillstring fatigue performance," *SPE drilling engineering*, vol. 5, no. 02, pp. 129–134, 1990.

[7] G. Grondin and G. Kulak, "Fatigue testing of drillpipe," *SPE Drilling & Completion*, vol. 9, no. 02, pp. 95–102, 1994.

[8] M. Knight and F. Brennan, "Fatigue life improvement of drill collars through control of bore eccentricity," *Engineering Failure Analysis*, vol. 6, no. 5, pp. 301–319, 1999.

[9] S. M. Zamani, S. A. Hassanzadeh-Tabrizi, and H. Sharifi, "Failure analysis of drill pipe: A review," *Engineering Failure Analysis*, vol. 59, pp. 605–623, 2016.

[10] J. D. Cearley, "Fishing techniques for drilling operations," 1999.

[11] J. Tian, C. Wu, L. Yang, Z. Yang, G. Liu, and C. Yuan, "Mathematical modeling and analysis of drill string longitudinal vibration with lateral inertia effect," *Shock and Vibration*, vol. 2016, 2016.

[12] L. Khajiyeva, Y. Sabirova, A. Kudaibergenov, and A. Kudaibergenov, "Application of the lumped-parameter method for modeling nonlinear vibrations of drill strings with stabilizers in a supersonic gas flow," *Applied Mathematical Modelling*, vol. 110, pp. 748–766, 2022.

[13] A. Ghasemloonia, G. Rideout, and S. Butt, "Analysis of multi-mode nonlinear coupled axial-transverse drillstring vibration in vibration assisted rotary drilling," *Journal of Petroleum Science and Engineering*, vol. 116, pp. 36–49, 2014.

[14] D. G. Rideout, A. Ghasemloonia, F. Arvani, and S. D. Butt, "An intuitive and efficient approach to integrated modelling and control of three-dimensional vibration in long shafts," *International Journal of Simulation and Process Modelling*, vol. 10, no. 2, pp. 163–178, 2015.

[15] M. Sarker *et al.*, *Modeling and simulation of vibration in deviated wells*. PhD thesis, Memorial University of Newfoundland, 2017.

[16] A. Ghasemloonia, D. Geoff Rideout, and S. D. Butt, "Vibration analysis of a drillstring in vibration-assisted rotary drilling: finite element modeling with analytical validation," *Journal of Energy Resources Technology*, vol. 135, no. 3, 2013.

[17] V. Vaziri, M. Kapitaniak, and M. Wiercigroch, "Suppression of drill-string stick–slip vibration by sliding mode control: Numerical and experimental studies," *European Journal of Applied Mathematics*, vol. 29, no. 5, pp. 805–825, 2018.

[18] M. Kapitaniak, V. V. Hamaneh, J. P. Chávez, K. Nandakumar, and M. Wiercigroch, "Unveiling complexity of drill–string vibrations: Experiments and mod-

elling," *International Journal of Mechanical Sciences*, vol. 101, pp. 324–337, 2015.

[19] G. Y. Grondin and G. Kulak, *Fatigue of drill pipe*. Department of Civil Engineering, University of Alberta, 1991.

[20] M. Galagedarage Don and G. Rideout, "An experimentally-verified approach for enhancing fluid drag force simulation in vertical oilwell drill strings," *Mathematical and Computer Modelling of Dynamical Systems*, vol. 28, no. 1, pp. 197–228, 2022.

[21] A. Mukherjee, R. Karmakar, and A. K. Samantaray, *Bond graph in modeling, simulation and fault identification*. IK International New Delhi, 2006.

[22] D. C. Karnopp, D. L. Margolis, and R. C. Rosenberg, *System dynamics: modeling, simulation, and control of mechatronic systems*. John Wiley & Sons, 2012.

[23] E. Szücs, *Fundamental Studies in Engineering 2- Similitude and modelling*. Elsevier, 1980.

[24] D. Rideout, F. Arvani, S. Butt, and E. Fallahi, "Three-dimensional multi-body bond graph model for vibration control of long shafts-application to oilwell drilling," *Proc. Integrated Modeling and Analysis in Applied Control and Automation*, pp. 25–27, 2013.

[25] M. Sarker, G. Rideout, and S. Butt, "Dynamic model for longitudinal and torsional motions of a horizontal oilwell drillstring with wellbore stick-slip friction," *Journal of Petroleum Science and Engineering*, vol. 150, pp. 272–287, 2017.

[26] M. H. Jalali and G. Rideout, "Development and validation of a numerical model for vibration of power lines," 2018.

[27] R. A. Reyes, D. G. Rideout, and S. D. Butt, "Dynamic analysis of a deep water marine riser using bond graphs.," in *ICBGM@ SummerSim*, pp. 204–211, 2016.

[28] H. Qiu, J. Yang, and S. Butt, "Investigation on bit stick-slip vibration with random friction coefficients," *Journal of Petroleum Science and Engineering*, vol. 164, pp. 127–139, 2018.

[29] E. Omojuwa, R. Ahmed, and J. Acquaye, "Mathematical modeling of axial oscillation tools in high-angle wells," *J Appl Mech Eng*, vol. 7, p. 316, 2019.

[30] X. Liu, N. Vlajic, X. Long, G. Meng, and B. Balachandran, "State-dependent delay influenced drill-string oscillations and stability analysis," *Journal of Vibration and Acoustics*, vol. 136, no. 5, 2014.

[31] C. S, W. M.W, and J. JA, "Added mass and damping of a vibrating rod in confined viscous fluids," *American Society of Mechanical Engineers*, 1976.

[32] M. Paı, T. Luu, S. Prabhakar, *et al.*, "Dynamics of a long tubular cantilever conveying fluid downwards, which then flows upwards around the cantilever as a confined annular flow," *Journal of Fluids and Structures*, vol. 24, no. 1, pp. 111–128, 2008.

[33] M. P. Paidoussis and N. Issid, "Dynamic stability of pipes conveying fluid," *Journal of sound and vibration*, vol. 33, no. 3, pp. 267–294, 1974.

[34] M. P. Paidoussis, *Fluid-structure interactions: slender structures and axial flow*, vol. 1. Academic press, 1998.

[35] S. Scampoli, "High-Fidelity Fluid-Structure Interactions," 2012.

[36] M. M. Huque, S. Imtiaz, S. Zendehboudi, S. Butt, M. A. Rahman, P. Maheshwari, *et al.*, "Experimental study of cuttings transport with non-newtonian fluid in an

inclined well using visualization and ert techniques," in *SPE Annual Technical Conference and Exhibition*, Society of Petroleum Engineers, 2020.

[37] J. A. Bannantine, *A variable amplitude multiaxial fatigue life prediction method*. PhD thesis, University of Illinois at Urbana-Champaign, 1989.

[38] B. A, D. K, K. H, K. W, M. B, and J. Petersen, "Multiaxial rainflow: A consequent continuation of professor tatsuo endo's work," in *The rainflow method in fatigue*, pp. 31–40, Elsevier, 1992.

[39] T. Morishita, F. Ogawa, and T. Itoh, "Evaluation and visualization of multiaxial fatigue behavior under random non-proportional loading condition," *Frattura ed Integrità Strutturale*, vol. 11, no. 41, pp. 45–53, 2017.

[40] SalomeMeca, "Structures and thermomechanics for studies & research," 2021.

[41] P. Sarah, "Operator calc-fatigue." https://code-aster.org. Accessed on May 20, 2023.

[42] M. G. Mayani, M. Svendsen, S. Oedegaard, *et al.*, "Drilling digital twin success stories the last 10 years," in *SPE Norway One Day Seminar*, Society of Petroleum Engineers, 2018.

[43] DAU, "Defense acquisition glossary." https://www.dau.edu/glossary/Pages/Glossary, 02 2021. (Accessed on 02/15/2021).

[44] T. R. Wanasinghe, L. Wroblewski, B. K. Petersen, R. G. Gosine, L. A. James, O. De Silva, G. K. I. Mann, and P. J. Warrian, "Digital twin for the oil and gas industry: Overview, research trends, opportunities, and challenges," *IEEE Access*, vol. 8, pp. 104175–104197, 2020.

[45] J. Domone, "Digital twin for life predictions in civil aerospace," *Atkins White Paper. Digital twin can potentially integrate all the data between previous generation vehicles and current vehicle concept in its digital model*, 2018.

[46] M. E. Cobern, "Downhole vibration monitoring & control system," tech. rep., APS Technology, Inc.(US), 2005.

[47] H. Mostaghimi, J. R. Pagtalunan, B. Moon, S. Kim, and S. S. Park, "Dynamic drill-string modeling for acoustic telemetry," *International Journal of Mechanical Sciences*, vol. 218, p. 107043, 2022.

[48] V. Dubinsky, H. Henneuse, and M. Kirkman, "Surface monitoring of downhole vibrations: Russian, european, and american approaches," in *European Petroleum Conference*, OnePetro, 1992.

[49] H. Rafezi and F. Hassani, "Drilling signals analysis for tricone bit condition monitoring," *International Journal of Mining Science and Technology*, vol. 31, no. 2, pp. 187–195, 2021.

[50] M. Klaic, Z. Murat, T. Staroveski, and D. Brezak, "Tool wear monitoring in rock drilling applications using vibration signals," *Wear*, vol. 408, pp. 222–227, 2018.

[51] R. W. Spencer, "Detection of downhole vibrations using surface data from drilling rigs," Apr. 1 2014. US Patent 8,688,382.

[52] Y. Zha and S. Pham, "Monitoring downhole drilling vibrations using surface data through deep learning," in *SEG Technical Program Expanded Abstracts 2018*, pp. 2101–2105, Society of Exploration Geophysicists, 2018.

Chapter 3

An Experimentally-Verified Approach for Enhancing Fluid Drag Force Simulation in Vertical Oilwell Drill Strings

Abstract

The oilwell drilling fluid flows cause viscous and hydrodynamic forces on drill strings. This effect is ignored or treated as a constant in most drill string models. The present study introduces mathematical models for lateral vibration damping and axial drag forces that are employable in lumped segment drill string models. First, the variables to which drilling fluid-generated forces are most sensitive were identified and the Response Surface Method was applied to design the experiment matrix. The lateral vibration-damping experiments, which were validated using a scaled-down physical model, and the axial drag experiments were done using Fluid-Structure Interaction simulations. The results were statistically analyzed to acquire the models and were implemented in a 3D lumped segment bond graph developed using the Newton-Euler formulation and body-fixed coordinates. The results indicate a considerable effect of the extended treatment of damping and axial drag on bending moment fluctuation, wellbore interactions, and weight on bit.

Keywords: *Drill string damping; Bond graph; Fluid-structure interaction*

Co-authorship Statement

This chapter is a manuscript of a full paper that is published in Journal of Mathematical and Computer Modelling of Dynamical Systems. The co-authorship statement for this chapter follows:

The declaration applies to the following article
M. Galagedarage Don and G. Rideout, "*An experimentally-verified approach for Enhancing Fluid Drag Force Simulation in Vertical Oilwell Drill Strings*", Mathematical and Computer Modelling of Dynamical Systems, vol. 28, no. 1, pp. 197–228, 2022. **Article status: Published** The PhD student analyzed the literature, performed the experiments, collected the data, developed the codes and prepared the manuscript. The supervisor edited, helped organize the manuscript, and contributed to the choice of case studies.

3.1 Introduction

Vibrating slender structures such as fluid conveying pipes are not rare in engineering applications. Therefore, many researchers have investigated the vibration and stability of a tubular beam system subjected to internal and external axial flows [1–5]. Oil well drill strings are special among them as they transmit fluids and highly complex loads. Therefore, pure mathematical modelling of a drill string to the near realistic level is quite cumbersome. Numerous attempts have been made to model this problem using both mathematical and simulation-based approaches [6]. Although most studies have adequately modelled the drill-string dynamics, the bulk of the literature makes simplifying assumptions about fluid damping and axial drag effects. For example, some models use Stokes friction [2, 3, 7] while others use viscoelastic mechanical

models such as Maxwell, Rayleigh, or Kelvin–Voigt [8–10]. Most of the simulation models either do not consider the damping effect or treat it as a constant or a linear viscous damper [11–14].

This study specifically targets the development of a lateral vibration damping model that can be implemented in drill string lumped segment simulation models. A series of FSI simulations and the Design of Experiments (DoE) approach are used to develop the statistical model. Being a simulation-based statistical model, it has the privilege of assessing most of the contributing variables within their respective ranges. Therefore, it has the potential to capture the effects of fluid rheological properties as well as the geometry and position of the drill string. In addition, a separate statistical model is presented to estimate the viscous and hydrodynamic forces using the same approach.

Along with estimating the buoyant force acting on the structure, this study provides a complete solution to estimate the overall effect of drilling fluid on lateral vibration damping and the WOB. The FSI simulations are partially validated for lateral vibration damping using an experimental apparatus for a non-Newtonian fluid. Finally, the developed statistical models are implemented in a 3D lumped segment bond graph to assess the importance of having such a model in a lumped segment model.

A Background Study is provided in Section 3.1 to explore a variety of analytical and numerical drill string models. This provides a thorough insight into the variables to consider in developing the damping and drag models. Further, it describes the tools and techniques that can be used in developing them. Section 3.2 provides the methodology followed in developing both lateral damping and axial drag force models. The screening process to identify the most contributing variables, assumptions, simulation approach, analysis of results, and the experimental validation are presented in this section. In Section 3.3, a case study is presented to evaluate the significance of

the two mathematical models when employed in a lumped segment model, followed by a Discussion, Conclusion, and Further Work.

3.1.1 Background study

Analytical, experimental, and numerical approaches have been used to understand drill string vibrations and damping. This section highlights previous attempts to model drill string dynamics and the damping effect. Further, it provides background information on FSI simulations, statistical model development, and 3D lumped segment bond graph simulations.

3.1.1.1 Analytical modelling of fluid conveying pipe dynamics and damping

As mentioned by Païdoussis [5], the first-ever studies regarding the dynamics of fluid conveying pipes, supported at both ends, were done by Feodos'ev [15], Housner [16], and Niordson [17] in 1951, 1952, and 1953 respectively. They have developed linear equations and drawn conclusions on stability.

Drill string vibrations are primarily damped by the viscous drilling fluid passing through the drill string as well as the annular space between the drill string and the wellbore. As mentioned in [18], the drilling fluid generates a reaction force on the vibrating structure. This reaction force can be interpreted as an added mass and a damping contribution to the dynamic response of the component. Based on that concept, they have presented a closed-form solution for a cylindrical rod vibrating in a viscous fluid that was validated using experimental results. They have concluded that both the added mass factor and the damping coefficient depend on the kinematic viscosity. As further mentioned in [18], this behaviour has also been mentioned in [19]

which motivates to consider the rheological properties and the density of the drilling fluid in modelling the damping ratio of the vibrating structure.

Further to that, [1] explains that the fluid flow-related forces acting on cylindrical rods may switch from damping to destabilization. Also, [1] describes the effect of the eccentricity of the inner cylindrical rod on the added mass factor (C_M) and the viscous damping coefficient (C_V). This study has been done using the Finite Element Method (FEM) and indicates that both (C_M) and (C_V) increase with the eccentricity. This motivates us to consider that the eccentricity of the drill string in the wellbore is an important variable in modelling the damping effect.

The behaviour of added mass and damping of cylindrical structures in confined fluids is presented in [20]. A finite element analysis approach has been taken and continuously deforming space-time finite elements are used to capture the effect of moving cylinders and changing shapes of the fluid domain. It is further reported that the fluid damping coefficients tend to rise with increasing vibration amplitude. This indicates that the wall effect has a considerable influence on the damping ratio and should be included. On the other hand, the added mass coefficient can either increase or decrease with increasing vibration amplitude.

A flow-velocity-dependent damping, in addition to the damping associated with fluid friction, is presented by [1]. The overall damping is considered as the summation of the two variants. This suggests that the velocity through the pipe and the annulus has an effect on the damping ratio of the drill string. According to [8], the dynamics are mainly governed by the inner pipe flow when the annulus is wider. The damping effect increases with increasing inner pipe flow velocities. Narrow annuli flows can overcome the effect of the inner pipe flow and destabilize the system. The model presented in [8] is limited to laminar flow, while the drill pipe is considered a simple hollow cylindrical structure.

Based on the linearized equation of motion introduced by [4], Kjolsing and Todd [21] presented a modified version of the equation, introducing the annulus fluid effects. The analytical developments were limited to small vibration amplitude and steady plug-flow conditions. The damping ratio increased with increasing conveyed fluid velocity through the pipe. This is yet to be further studied for different velocity ranges with both Newtonian and non-Newtonian fluids.

A Coriolis force gets established when the fluid conveying pipe is under vibration [1, 22]. This force becomes a damping mechanism if the tube is movable at the ends, causing energy dissipation due to work done. Conversely, if the two ends are non-movable, there will be no effect from the Coriolis force, especially at lower speeds [23]. Therefore, disregarding the effect of the Coriolis force will still give a reasonable approximation in modelling a drill string in operation.

In summary, the analysis of the above-mentioned analytical modelling approaches shows that the damping ratio of a drill string depends on the drilling fluid rheology, density, velocity, and position of the drill string in the wellbore.

3.1.1.2 Drill string numerical simulation models

In addition to the above-mentioned analytical approaches, several numerical model developments to study the vibration behaviour of drill strings are also available in the literature.

Nonlinear three-dimensional lumped segment shaft models are presented in [9, 24], which resemble a vertical drill string. They have used the bond graph-based approach to simulate axial, torsional, and lateral vibrations with wellbore contact. The damping effect is modelled as a resistive element with a constant damping ratio which requires further improvements in order to capture the nonlinearities. The developed model is used to investigate the use of an active lateral vibration control with a closed-

loop control system targeting drilling performance optimization.

Based on the bond graph simulation infrastructure presented by [9], the longitudinal motion, torsional motion, and combinations thereof in a horizontal oilwell drill string were developed by [13]. The model contains the dynamic wellbore friction in the 'built' and 'horizontal' sections. The effects from the drilling fluid are incorporated with Newtonian flow formulations.

Several finite element method (FEM) based models are also available in the literature. The model presented in [25] studies the combined axial-torsional vibration of a drill string under combined deterministic and random excitations. The damping matrix is considered a linear combination of mass and stiffness matrices. Also, drill string vibrations in 3D space were analyzed by [26] with finite shaft elements consisting of 12 degrees of freedom. As further investigations, [27] proposed a coupled lateral-torsional elastodynamic model with consideration of string–borehole interaction. It was later experimentally validated by their study presented in [28]. As mentioned in [9], although those finite element models can be easily reconfigured, they are not time-efficient to be used in closed-loop dynamic response simulations.

In summary, in the area of drill string simulation, analytical models need simplifying assumptions; hence the ability to capture the effect of all the variables is restricted to some extent. The FEM approaches contribute generously, but the available computation power limits their usage in simulating dynamic responses. On the other hand, a lumped segment Newtonian approach can be a good compromise. Accurate results can be obtained with fewer degrees of freedom than a finite element model and less formulation difficulty than an analytical elastodynamic model. As such, it has numerous strengths over the former two as it requires comparatively less computation power, making it suitable to be used in applications where rapid results are required. Also, it is convenient to use the bond graph approach in modelling and integrating

different domains such as fluid, structural, and external contacts. The effect of the drilling fluid is not yet modelled such that it can be employed in a computationally efficient model such as a lumped segment bond graph model. This will be addressed in this paper.

3.1.1.3 Fluid structure interaction (FSI) simulation

Drill string vibrations are subjected to damping due to the flow through the annular space and the pipe. An FSI simulation can be used to investigate this phenomenon as it allows a large number of virtual experiments to be conducted with low cost and high repeatability to quantify the effect of multiple variables on fluid-related damping [5, 29].

ANSYS® Workbench provides the necessary tools for these kinds of simulations. The 'Transient Structural' (TS) software in Workbench facilitates the simulation of the structural component in the domain of FEM, while the 'Fluid Flow (Fluent) package' is equipped with the necessary tools for the fluid flow simulation [29].

In TS, a fluid-solid interface on surfaces is defined, identifying surfaces in the structural model that will accept fluid forces from the computational fluid dynamics (CFD) code (i.e. Fluent). On the other side, Fluent defines a system coupling dynamic mesh zone, which identifies surfaces in the CFD model that will accept the motion from the calculated structural deformations. The coordination of the data transfer between TS and Fluent is done by the 'System Coupling' software. It provides one-way and two-way force-displacement coupling between ANSYS® Fluent and ANSYS® Mechanical software for FSI simulations. Further, system coupling synchronizes the individual solvers, manages data transfers between solvers, and monitors the overall convergence of the FSI solution [29]. The FSI simulation can be used to determine the vibration amplitude decay for a given impulse.

3.1.1.4 Damping ratio determination

As described in [30], if a system can be modelled as a spring-mass-damper system, the damping ratio (ζ) can be calculated from the time response using logarithmic decrement. Equations 3.1 and 3.2 can be used to determine the damping ratio. The damping ratios determined through this approach can be used in the design of experiments (DoE) process to develop a mathematical model with variables such as pipe eccentricity, fluid velocity, and fluid rheology.

$$\delta = \frac{1}{n} \log \left(\frac{x(t_0)}{x(t_{n+1})} \right) \tag{3.1}$$

$$\zeta = \frac{\delta}{\sqrt{4\pi^2 + \delta^2}} \tag{3.2}$$

where δ is the logarithmic decrement, t_0 is the time corresponding to the first peak, n is the number of peaks considered after t_0, x is the displacement, and ζ is the damping ratio.

3.1.1.5 Design of experiments (DoE)

The 'best-guess' (with engineering judgment) is a commonly-used approach in engineering, while the one-factor-at-a-time (OFAT) approach is considered the standard and systematic strategy for experimentation. Nevertheless, according to [31], both of these approaches are identified as less efficient for a higher number of variables. More efficient methods such as factorial design and RSM were introduced in the early 1920s, based on statistics theories. Currently, they are called the design of experiment (DoE) methods in general [32].

DoE, in essence, is a way of using statistics for experimentation in a methodical manner. It enables researchers to build mathematical models that predict how input

factors interact to produce output variables of a system or a process. Moreover, this approach can be used to: understand the process, filter out important parameters, understand the interactions of each parameter, and optimize the response variable. Hence, DoE is recognized as the most suitable and efficient method in experimentation [32].

The RSM provides experimental designs for fitting models of arbitrary order [33]. The second-order design facilitates the approximation of a response surface relationship with a fitted second-order regression model to include nonlinearities [32]. The procedure presented in Figure 3.1 must be followed in order to accurately use the RSM method [34]. Problem identification is crucial at the beginning of the process, where all the variables involved are identified. Next, those variables should be sorted into two categories: independent variables (factors) and dependant variables (responses). Then the most important variables are to be selected through a screening process. After that, the appropriate design should be selected which suits the problem. Box-Behnken Designs (BBD), Central Composite Design (CCD), Central Composite Rotatable Design (CCRD), and Face Central Composite Design (FCCD) are some of the available options. Once the proper design is selected, the experiments can be performed accordingly to get the responses.

3.1.1.6 Drilling fluid generated forces

There are mainly four types of forces acting on a drill pipe in operation due to the presence of the drilling fluid: 1) viscous forces 2.) inertial forces due to the upset construction 3.) Coriolis forces and 4.) upthhrust.

The tangential viscous forces acting on the drill string surfaces generate an axial load. By intuition, it can be roughly estimated that the drag force acting on the

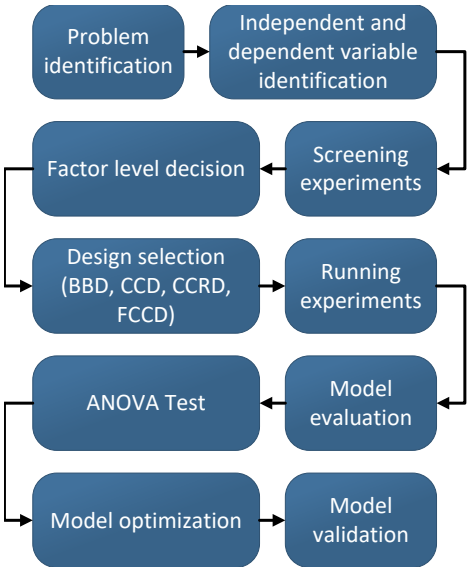

Figure 3.1: Procedure for RSM

inner surface is less than that of the outer surface because the outer surface has a comparatively higher surface area. In addition to that, the outer surface has an upset construction at the threaded joint that creates a higher resistance to flow hence a higher thrust. If the drilling fluid is sent down through the pipe and rises through the annular space, the drill string will experience this upward hydrodynamic force. Thirdly, a Coriolis force acts in the system if the drill string vibrates off the ground. The Coriolis effect can be neglected when the drill bit is connected with the rock [1] as explained in Section 3.1.1.1. Finally, the upthrust or the buoyant force due to the immersion in the drilling fluid also plays a role. One should consider these forces carefully when determining the WOB. The density ratio between the drilling fluid and the drill string material, which is usually steel, determines the buoyancy factor that relates the weight of the drill string in the air to the weight when suspended in the drilling fluid [35].

3.2 Materials and methods

This section presents the methodologies followed to develop the lateral vibration damping and axial drag models. An FSI simulation was employed in developing each model with different boundary conditions and excitations. After identifying the governing variables, a screening process was carried out using the FSI simulation following a 'one factor at a time' approach. After identifying the most contributing variables, the design of experiments (DoE) approach was used to reduce the required number of FSI simulations. Based on the simulation results, the mathematical models were developed through statistical analysis which can be employed in lumped segment drill string models.

The detailed methodology followed in developing the lateral damping model is presented in Sub-section 3.2.1. The methodology for drag-model development is presented in Section 3.2.2. Further, the experimental validations of the FSI simulation used for both Newtonian and non-Newtonian fluids are presented in Section 3.2.3.

3.2.1 Lateral vibration damping model

In finding a mathematical model of the lateral damping ratio (ζ), as a function of the most contributing variables, the initial step was to determine all the variables that considerably influence the damping constant. The variables identified are presented in Table 3.1 and Equation 3.3.

$$\zeta = f(\kappa, n, \tau, v, \dot{\gamma}_c, d_{min}, \rho) \tag{3.3}$$

Through further simulations, it was identified that the damping ratio also depends on the combined effect of eccentricity (e) and the wellbore diameter (r_{well}). The

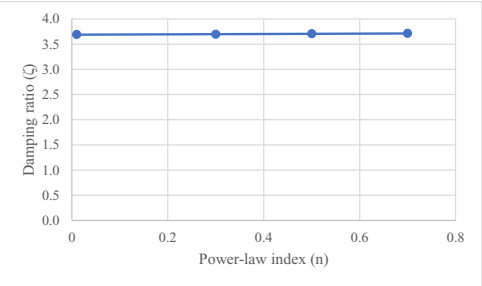

(a) ζ vs. n

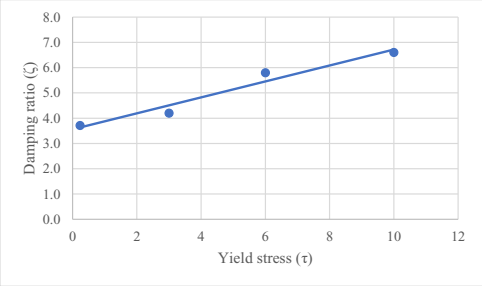

(b) ζ vs. τ (Pa)

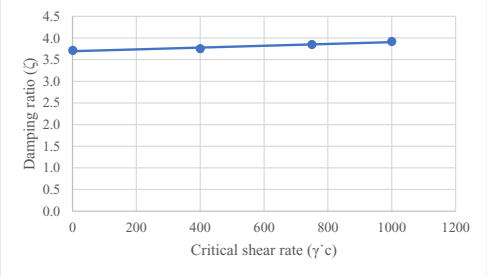

(c) ζ vs. γ (Pa)

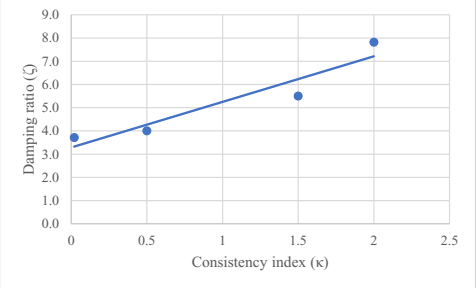

(d) ζ vs. $\dot{\kappa}$ (1/s)

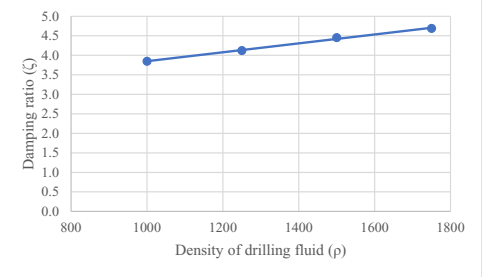

(e) ζ vs. ρ (kg/m^3)

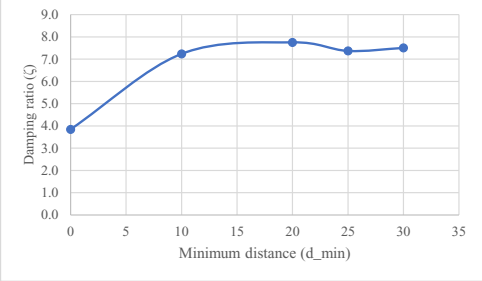

(f) ζ vs. e (mm)

Figure 3.2: Damping ratio (ζ) vs. individual variables

minimum distance between the drill pipe and the wellbore (d_{min}), which is a derived variable of (e) and (r_{well}), was considered important. It is presented in Equation 3.5. The individual effect on the damping ratio of each variable is illustrated in Figure 3.2. They were evaluated through FSI simulations for non-Newtonian fluids.

$$\zeta = f(\kappa, \tau, v, d_{min}, \rho) \tag{3.4}$$

$$d_{min} = r_{well} - r_{pipe} - e \tag{3.5}$$

In summary, the simulations were performed according to Table 3.2, and the results

Table 3.1: Variables that affect the damping ratio

Variable of control	**Minimum**	**Maximum**	**Symbol**	**Units**
Consistency index	0	2	κ	kg/ms
Power law (Flow behaviour) index	NA	NA	n	-
Yield stress	0	10	τ	Pa
Velocity through pipe	0.1	1.5	v	m/s
Critical shear rate	NA	NA	$\dot{\gamma}_c$	$1/s$
Minimum distance between wellbore and pipe	6.46	36.46	d_{min}	mm
Density of drilling fluid	1000	2000	ρ	kg/m^3

for ζ and ω_n were determined using the method described in Section 3.1.1.4. The FSI simulations were done using ANSYS® Workbench, while the RSM was used to analyze the data statistically. Design-Expert™ 13 software was used to design the experiment grid and analyze the results. All the FSI simulations were done using the high-performance computing resources provided by ACENET Canada. The results are presented in the last two columns of Table 3.2. A similar approach was taken in developing the axial drag model. Therefore, only the results of axial drag, and not the detailed steps, are presented in the interest of brevity.

3.2.1.1 Approximation of the continuous FSI simulation element to a lumped segment system element

The FSI simulation and the lumped segment model, illustrated in Figure 3.3.*a* and *b* respectively, can be considered as approximately equivalent for lateral vibration damping. Figure 3.3.*a* represents a flexible body while Figure 3.3.*b* represents a rigid body. Both the bodies oscillate with small amplitudes in comparison with their lengths. For example, the length of the beam is approximately 10 m while the maximum amplitude is around 10 mm. Therefore, the movement of the two ends can be neglected and hence can be approximated to a fixed-fixed case.

Table 3.2: Experiments and the respective results

Sim	d_{min}	τ	κ	ρ	v	e	ζ	F
1	36.46	10	0	1750	1.5	0	14.02	12.91
2	21.46	5	1	1000	0.8	15	11.54	9.34
3	36.46	0	0	1000	0.1	0	4.45	0.00
4	6.46	10	2	1750	1.5	30	23.49	65.19
5	6.46	0	2	1750	0.1	30	17.30	11.50
6	6.46	10	0	1750	0.1	30	16.96	8.51
7	21.46	5	1	1750	0.8	15	11.86	9.03
8	21.46	5	1	1375	0.8	15	11.83	9.15
9	36.46	0	2	1000	1.5	0	7.93	162.14
10	6.46	10	2	1750	0.1	30	22.14	20.08
11	21.46	5	0	1375	0.8	15	9.34	2.76
12	6.46	0	2	1750	1.5	30	19.47	81.20
13	21.46	10	1	1375	0.8	15	13.90	5.14
14	36.46	10	2	1750	0.1	0	14.02	29.59
15	36.46	10	0	1000	0.1	0	8.95	12.82
16	36.46	10	0	1000	1.5	0	12.69	17.25
17	6.46	0	2	1000	0.1	30	17.34	11.52
18	36.46	0	0	1750	1.5	0	8.37	2.97
19	21.46	5	1	1375	0.8	15	11.83	9.22
20	6.46	10	2	1000	1.5	30	15.58	62.52
21	6.46	0	0	1750	1.5	30	8.37	2.97
22	21.46	5	1	1375	0.8	15	11.83	9.23
23	6.46	10	2	1000	0.1	30	23.20	20.08
24	6.46	0	2	1000	1.5	30	14.47	67.26
25	21.46	5	1	1375	0.8	15	11.83	9.23
26	36.46	0	2	1000	0.1	0	17.34	11.52
27	36.46	0	0	1750	0.1	0	8.33	0.02
28	36.46	5	1	1375	0.8	0	14.45	20.91
29	21.46	5	1	1375	0.1	15	14.07	7.65
30	21.46	5	1	1375	0.8	15	11.83	9.23
31	6.46	5	1	1375	0.8	30	14.45	20.93
32	36.46	0	2	1750	0.1	0	17.30	11.51
33	6.46	0	0	1000	1.5	30	7.26	1.70
34	6.46	10	0	1000	1.5	30	12.69	17.27
35	36.46	10	0	1750	0.1	0	16.96	8.52
36	21.46	5	1	1375	0.8	15	11.83	9.23
37	6.46	0	0	1750	0.1	30	8.33	0.02
38	36.46	10	2	1750	1.5	0	11.91	178.88
39	36.46	0	2	1750	1.5	0	9.51	175.48
40	21.46	5	1	1375	0.8	15	11.83	9.23
41	36.46	10	2	1000	1.5	0	7.59	165.65
42	21.46	5	2	1375	0.8	15	14.28	23.30
43	36.46	10	2	1000	0.1	0	13.57	28.84
44	21.46	5	1	1375	0.8	15	11.83	9.23
45	6.46	0	0	1000	0.1	30	7.25	0.01
46	6.46	10	0	1750	1.5	30	12.94	26.18
47	6.46	10	0	1000	0.1	30	17.74	8.53
48	36.46	0	0	1000	1.5	0	4.21	0.71
49	21.46	0	1	1375	0.8	15	11.54	9.37
50	21.46	5	1	1375	1.5	15	11.00	9.23

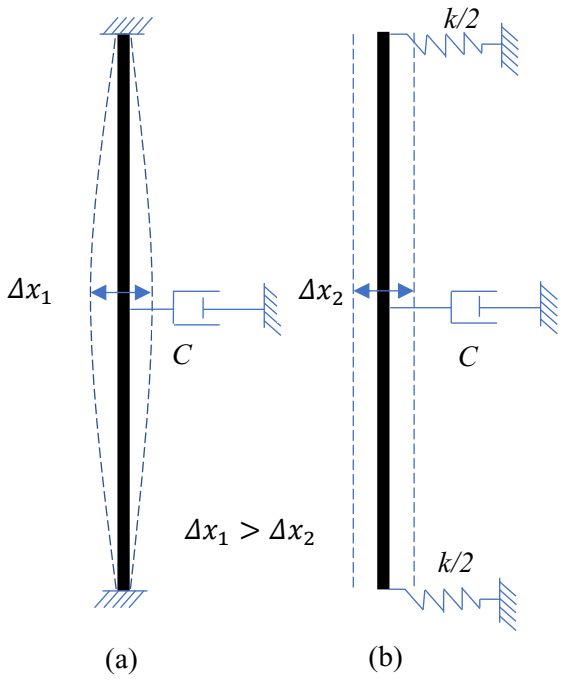

Figure 3.3: The approximation to a spring-mass-damper system

3.2.1.2 The FSI simulation

The maximum angular oscillation is approximately 1 degree for a given drill pipe in operation. This is applicable for most of the drill pipe-wellbore radii combinations and was verified through calculations. Therefore, the angular orientation effect on lateral damping can be neglected. Hence, this small vibration amplitude assumption allows the flexible body oscillation to be approximated to a translational lumped segment spring-mass-damper system. Based on this approximation, the damper with damping constant C is employed to represent the damping experienced by the flexible body, while the effective stiffness of the springs (k) represents the bending stiffness of the flexible body. This approximation is further justified in Section 3.4.

The bending stiffness is defined as the force required to laterally displace the mid-point of the flexible beam by a unit displacement. One can argue that the fixed-fixed

boundary condition may be too rigid to simulate the actual dynamics of the drill pipe, and instead, a flexible boundary condition is more appropriate. Nevertheless, the fixed-fixed boundary conditions were introduced to establish the computational stability of the FSI simulation as there are still some limitations that exist in commercial software, in the domain of FSI simulations, at the time of these experiments.

The structural part of the FSI simulation consists of a threaded connection of two drill pipes and two half lengths of the respective pipe as shown in Figure 3.4. This is taken as the 'repeating unit' of the BG lumped segment simulation presented in Section 3.3. The fixed-fixed boundary condition provides a sufficient approximation to actual scenarios where the clearance between the wellbore and the drill string is small in comparison with the length of the structure as described in Section 3.4. The material assigned is Structural Steel with Young's Modulus of 2×10^{11} Pa. The time step for the simulation was 0.03 s. Grid dependency tests were done for the structural and fluid simulation meshes separately. The number of elements was doubled and was checked for the consistency of the damping ratio (ζ). Hex dominant method was used for both the domains while keeping the element quality above 0.5. As excitation, an impulse was given at the mid-span of the beam with a maximum amplitude of 100 N. On the other hand, there are two separate fluid bodies in the fluid flow simulation: the pipe flow and the annular flow. The two flows are concurrent, resembling the fluid flow in an actual drilling process. In Fluent®, the k-omega viscous model was used, and a new fluid was defined to meet the rheology of the drilling fluid. The density (ρ), Consistency Index (κ), and Yield Stress Threshold (τ) were defined according to the respective experiment listed in Table 3.2. The Power-law Index (n) was kept at 0.7, while the Critical Shear Stress ($\dot{\gamma}_c$) was kept at 10 due to the lack of contribution to the damping effect in the range considered. The Herschel Bulkley model was used to simulate the drilling fluid by activating the turbulent non-Newtonian feature of

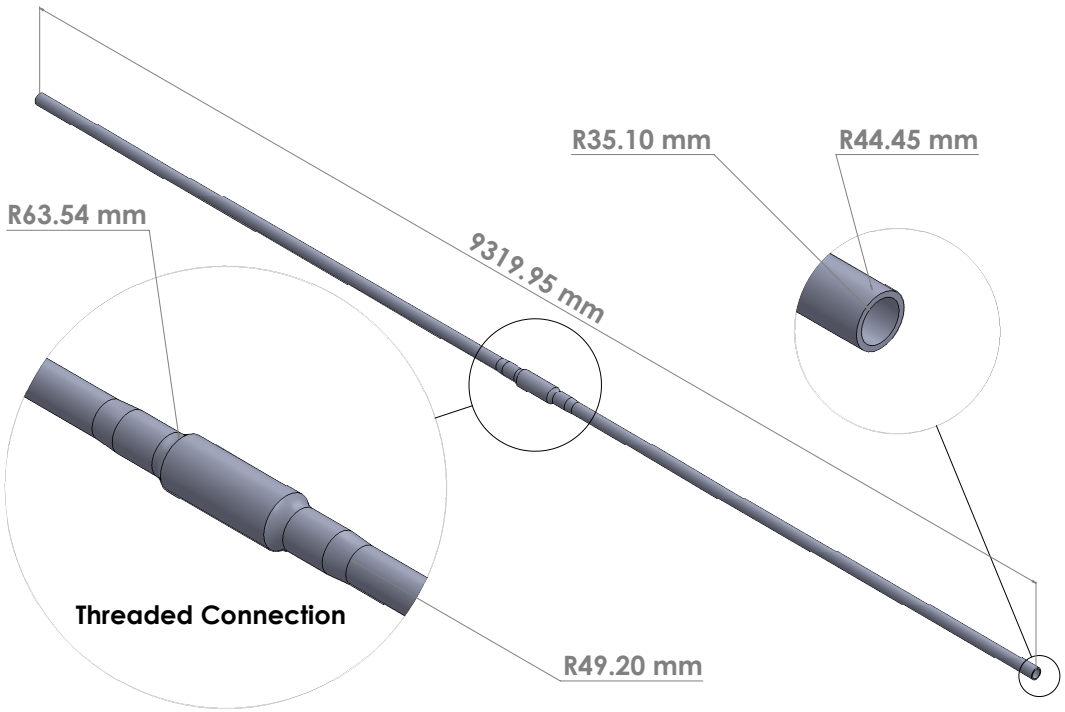

Figure 3.4: Repeating unit of the lumped segment model

ANSYS® Fluent (i.e. `turb-non-newtonian`) [36].

In defining the boundary conditions of the fluid domains, the inlets of both the pipe and the annulus were given velocity inlet conditions while the outlets were set as pressure outlets. Also, the structural body's inner and outer surfaces were set as stationary walls with no-slip shear conditions. The surfaces that touch the structural body's inner and outer surfaces were defined as dynamic mesh zones.

After setting up the structural and fluid simulations, System Coupling is used to communicate between the two domains. Setting up the data transfer between the domains is the key step of this section. Here a two-way data transfer should be implemented: between the annular flow and the outer surface of the structural body, and between the pipe flow and the inner surface of the structural body. Further, the time step must be consistent between the structural and fluid simulations.

Finally, the setup applications of TS and Fluent are connected to the setup of System Coupling to synchronize the individual solvers, manage data transfers between solvers, and monitor the overall convergence of the FSI solution.

In summary, a fluid-solid interface on surfaces is defined in ANSYS® Structural, and it identifies surfaces in the structural model that accept fluid forces from the CFD analysis. Meanwhile, in ANSYS® Fluent, a dynamic mesh zone is defined while it identifies surfaces in the CFD model that accept the motion from the calculated structural deformations. The System Coupling also plays a major role by synchronizing the individual solvers while managing data transfers between solvers and monitoring the FSI solution's overall convergence.

3.2.1.3 Analysis of data

The most important application of Design Expert software is the statistical analysis of the experimental results. The quality of the model is evaluated based on the analysis of variance (ANOVA) including R^2 and lack of fit. These results are presented in Table 3.3. Figure 3.5 illustrates the scatter plot of the predicted values versus the actual values. According to the analysis results, R^2 was 0.97 while the Predicted R^2 is 0.80. The latter is in reasonable agreement with the Adjusted R^2 of 0.94 as their difference is less than 0.2. The Adequate Precision Ratio measures the signal-to-noise ratio. It was estimated as 20.5, where a ratio greater than 4 is desirable. In other words, it indicates an adequate signal. The backward elimination method was used in refining the model terms to get a better approximation. Equation 3.6 and Figure 3.6 represent the mathematical model generated through the statistical analysis using Design-Expert™.

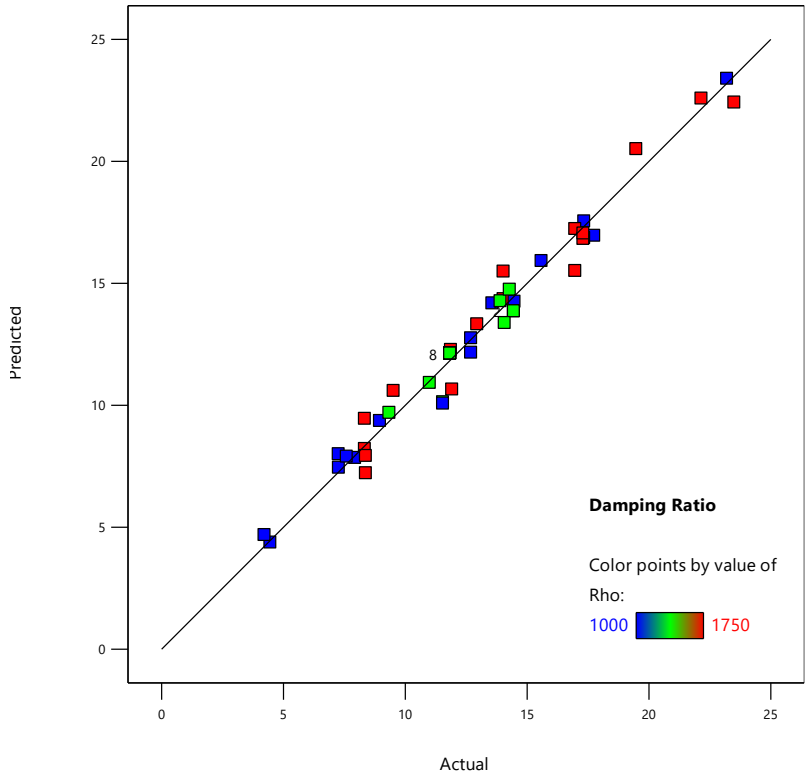

Figure 3.5: ζ- Predicted vs. actual

$$\begin{aligned}\zeta = {} & +12.54627 - 0.693954\ d_{min} - 0.084\ \tau + 4.24983\ \kappa - 0.001892\ \rho - 2.20353 v \\ & + 0.042799\ d_{min}\ \tau + 0.184160\ d_{min}\ \kappa + 0.000276\ d_{min}\ \rho + 0.157667\ d_{min}\ v \\ & - 0.115017\ \tau\ \kappa - 0.357980\ \tau\ v + 0.000089\ \kappa\ \rho - 3.34267\ \kappa\ v + 0.001447 \\ & + \rho\ v + 0.006495\ d_{min}^2 + 0.109795\ \tau^2 - 0.007902\ d_{min}\ \tau\ \kappa \\ & + 0.014765\ d_{min}\ \tau\ v - 0.000118\ d_{min}\ \kappa\ \rho - 0.083163\ d_{min}\ \kappa\ v \\ & - 0.000127\ d_{min}\ \rho\ v + 0.002956\ \kappa\ \rho\ v - 0.005616\ d_{min}\ \tau^2\end{aligned} \tag{3.6}$$

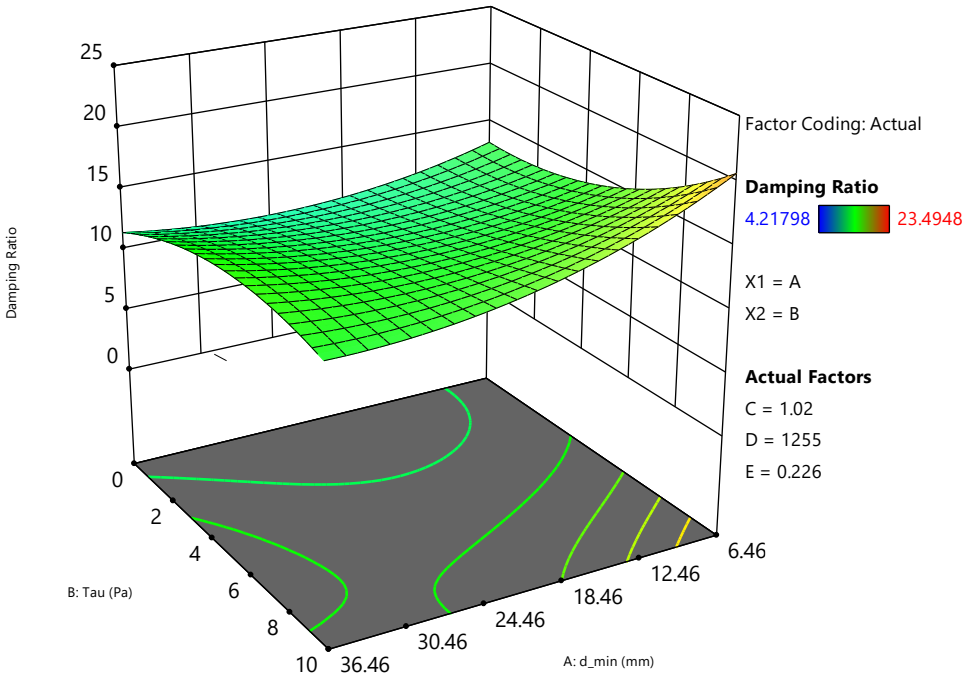

Figure 3.6: Damping ratio model

3.2.2 Axial drag model

The DoE with a statistical analysis approach used to develop the lateral damping model was utilized to establish the axial drag force model. The same set of FSI simulations was utilized to extract the axial drag force using a Probe tool in ANSYS® Transient Structural. Figure 3.7 illustrates the scatter plot of the predicted values versus the actual values. The mathematical model generated through the statistical analysis using Design-Expert™ is presented as Equation 3.7 and Figure 3.8. As depicted in Figure 3.8, the increasing τ has a considerably high effect on the axial drag. In refining the model terms, the Backward Elimination Method was followed to get the best-fit statistics. The R^2 was 0.99 while the Predicted R^2 of 0.97 was in reasonable agreement with the Adjusted R^2 of 0.99. The Adequate Precision Ratio was estimated as 67 which indicates an adequate signal. Equation 3.7 and Figure 3.8

represent the axial drag model.

Table 3.3: ANOVA for reduced cubic model

Source	Sum of Squares	df	Mean Square	F-value	p-value
Model	882.42	23	38.37	39.83	<0.0001
A-d_min	1.137E-13	1	1.137E-13	1.180E-13	1.0000
B-Tau	142.48	1	142.48	147.92	<0.0001
C-K	225.37	1	225.37	233.98	<0.0001
D-Rho	41.36	1	41.36	42.94	<0.0001
E-v	56.25	1	56.25	58.40	<0.0001
AB	16.07	1	16.07	16.69	0.0004
AC	50.65	1	50.65	52.59	<0.0001
AD	3.28	1	3.28	3.41	0.0764
AE	2.36	1	2.36	2.45	0.1294
BC	64.79	1	64.79	67.27	<0.0001
BE	0.6626	1	0.6626	0.6880	0.4144
CD	0.0250	1	0.0250	0.0260	0.8732
CE	17.73	1	17.73	18.41	0.0002
DE	6.25	1	6.25	6.49	0.0171
A^2	7.76	1	7.76	8.05	0.0087
B^2	0.2610	1	0.2610	0.2709	0.6071
ABC	11.24	1	11.24	11.67	0.0021
ABE	19.23	1	19.23	19.96	0.0001
ACD	14.05	1	14.05	14.59	0.0007
ACE	24.40	1	24.40	25.33	<0.0001
ADE	7.96	1	7.96	8.27	0.0079
CDE	19.26	1	19.26	20.00	0.0001
AB^2	8.35	1	8.35	8.67	0.0067
Residual	25.04	26	0.9632		
Lack of Fit	25.04	19	1.32		
Pure Error	0.0000	7	0.0000		
Cor Total	907.46	49			

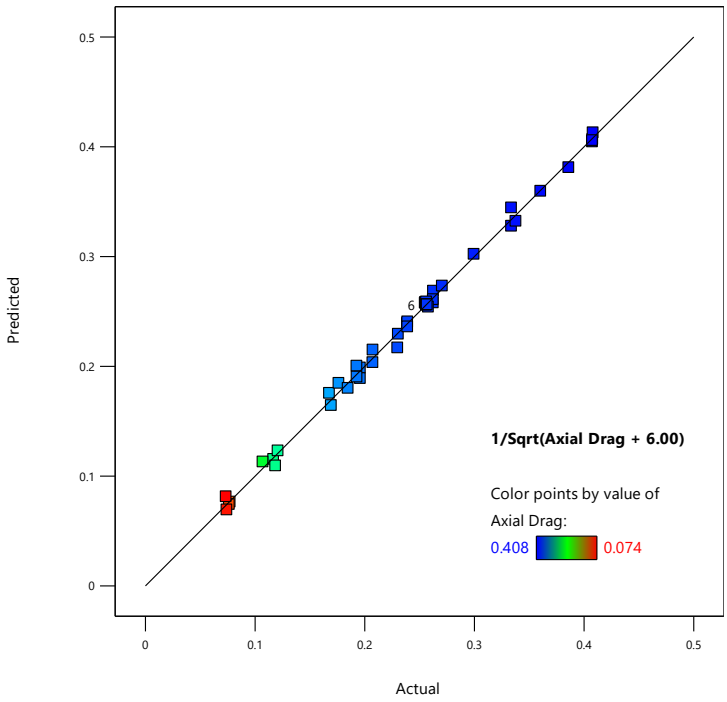

Figure 3.7: Drag force: predicted vs. actual

$$\sqrt{\frac{1}{F_{axial}+6}} = 0.458515 - 0.008247\ d_{min} - 0.038522\ \tau - 0.082539\ \kappa + 1.1 \times 10^{-6}\ \rho$$
$$- 0.091565\ v + 0.002308\ d_{min}\ \tau - 0.000031\ d_{min}\ \kappa - 2.1 \times 10^{-7}\ d_{min}\ \rho$$
$$+ 0.009765\ d_{min}\ v + 0.006870\ \tau\ \kappa + 1.01 \times 10^{-6}\ \tau\ \rho - 0.000888\ \tau\ v$$
$$+ 1.4 \times 10^{-6}\ \kappa\ \rho - 0.035233\ \kappa\ v - 0.000028\ \rho\ v + 0.000201\ d_{min}^2$$
$$+ 0.000949\ \tau^2 + 0.020037\ v^2 + 1.1342110^{-7}\ d_{min}\ \tau\ \rho + 0.000058\ d_{min}\ \tau\ v$$
$$- 0.000650\ d_{min}\ \kappa\ v - 1.6 \times 10^{-6}\ \tau\ \kappa\ \rho + 0.001970\ \tau\ \kappa\ v + 0.000012\ \kappa\ \rho\ v$$
$$- 0.000059\ d_{min}^2\ \tau - 0.000219\ d_{min}^2\ v \tag{3.7}$$

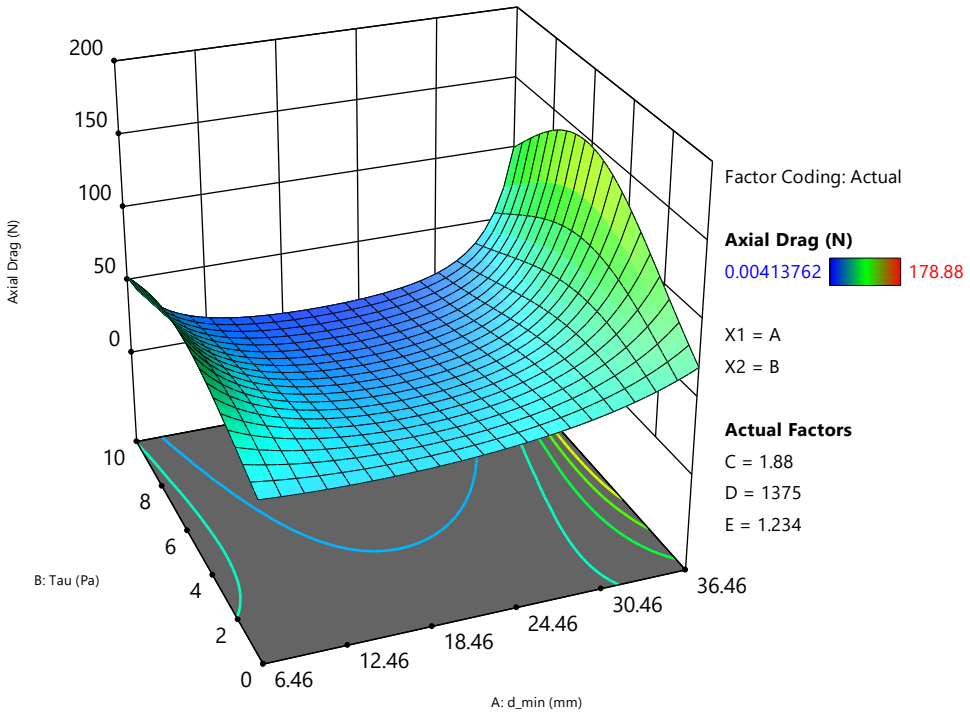

Figure 3.8: Axial drag model

3.2.3 Validation of the FSI simulation

The main goal of this experiment is to improve the confidence of the FSI simulation, which is used to develop the lateral damping and axial drag models. The simulation was scaled down to match the laboratory scale model, and the experimental results were compared with the simulation results.

3.2.3.1 Laboratory apparatus and experiment procedure

The apparatus used in the experimental work was first designed in SolidWorks® as shown in Figure 3.9 while the fabricated model is shown in Figure 3.10. Fluid driven by a centrifugal pump enters the inner vertical pipe through the inlet (A) at the top, fills the chamber at the bottom (C) and rises through the annulus. The inner pipe

can be excited using a permanent magnet placed at the steel fitting (F), which resembles the drill string threaded connection. The oscillation is captured using a laser displacement sensor (i.e. Acuity™ AR 200) and the data acquisition system.

The experiment was performed for Newtonian and non-Newtonian fluids separately.

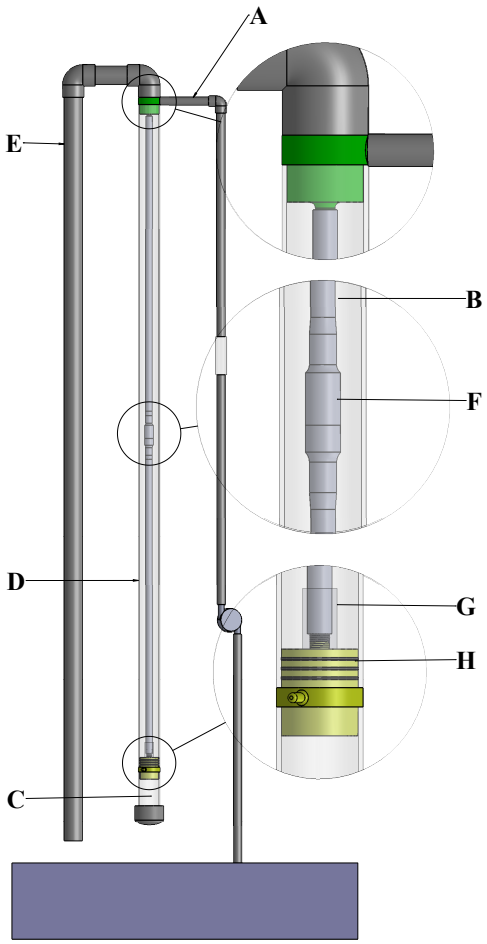

Figure 3.9: The 3D CAD model of the apparatus

For the Newtonian fluid case, the apparatus was directly connected to the laboratory water supply, which can drive water with a maximum rate of $3.7 \times 10^{-4}\ m^3/s$. The method presented in 3.1.1.4 was used to estimate the damping ratios while the

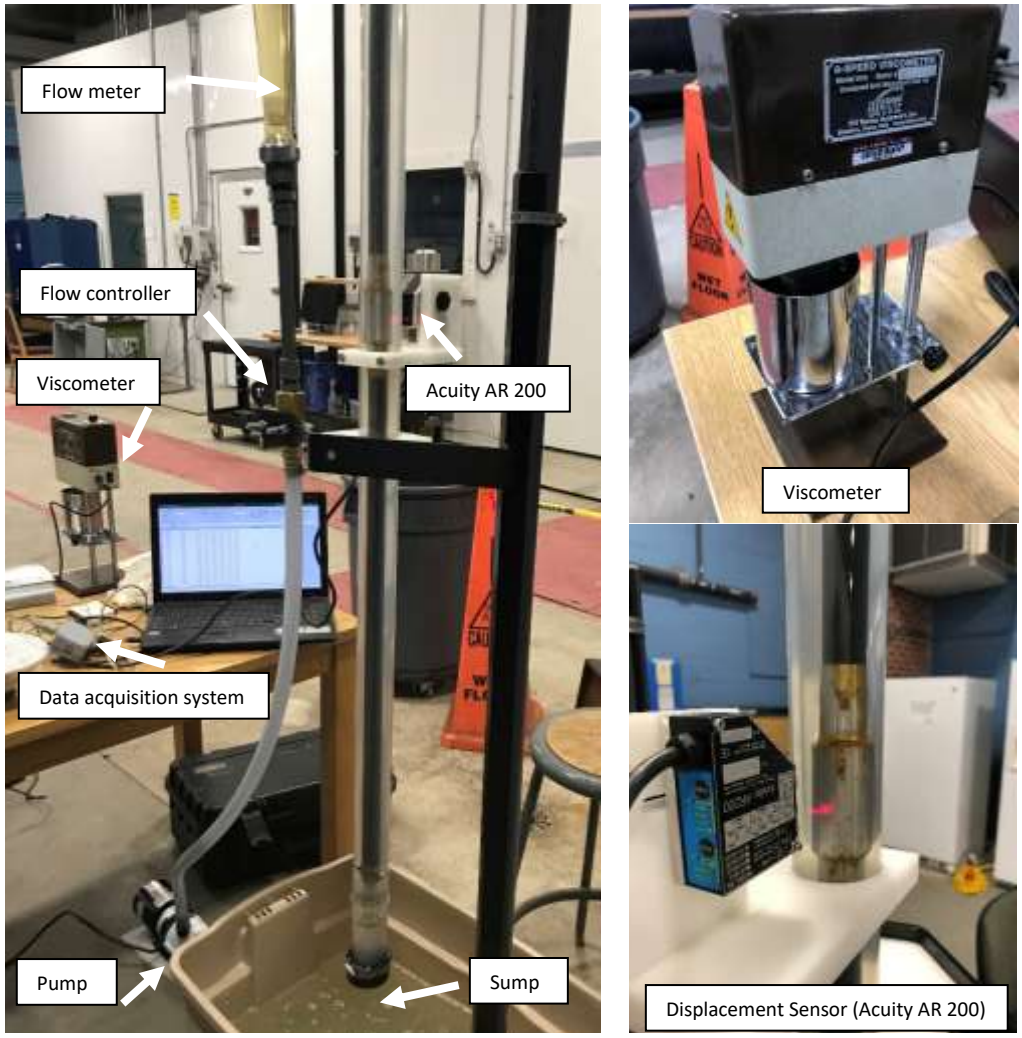

Figure 3.10: Laboratory scale apparatus

respective steady flow velocities were determined using the flow meter reading. A sample reading taken using Acuity AR 200 is shown in Figure 3.11. The results are illustrated in Figure 3.12 along with the simulation results.

The non-Newtonian fluid was made using 30 g of Xanthan Gum dissolved in 100 litres of water. The rheological properties of the fluid were determined using the OFITE model 800 viscometer shown in Figure 3.10. The shear stress versus shear rate curve determined using the viscometer is illustrated in Figure 3.13. A centrifugal

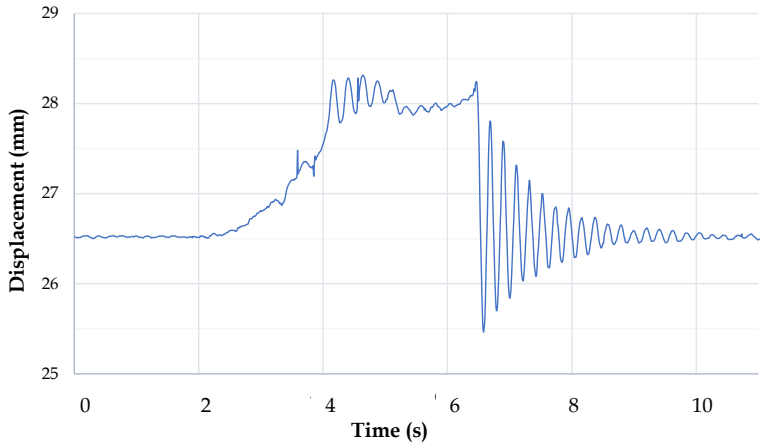

Figure 3.11: Sample experimental data

pump of 372 W was used to drive the fluid through the apparatus. Damping measurements were taken following the same procedure used in the Newtonian fluid case. The experimental and simulation results are presented in Figure 3.14.

The experimental and the simulation results are in reasonable agreement for both Newtonian and non-Newtonian fluids as shown in Figures 3.12 and 3.14. The experimental curves in both cases at lower speeds show a reduction of the damping ratio with increasing flow speed which is also reflected in the simulation result. However, the experimental results corresponding to the second half of the speed range indicate an increase of the damping ratio, which is not evident in the simulation results. Nevertheless, the simulation can capture the overall reduction of the damping ratio with increasing fluid speed. The technical difficulties faced in FSI simulations and techniques used to overcome them are discussed in Section 3.4.

3.3 Case study and results

The damping and drag models were implemented in a 3D multi-segment bond graph. The damping ratio (ζ) changes continuously depending on the respective values of

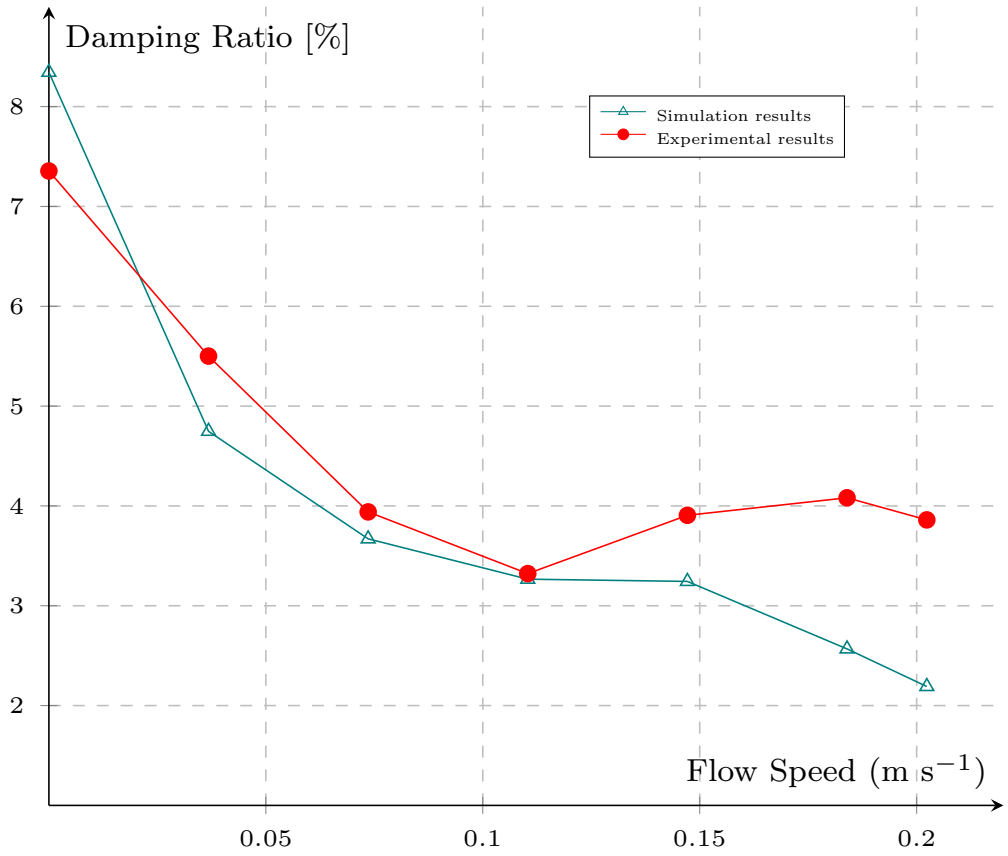

Figure 3.12: Damping ratio change in Newtonian fluid

κ, τ, v, d_{min}, and ρ. The lateral damping model presented in Equation 3.6 was implemented in the bond graph model as a modified 'R' element. The drag force model presented in Equation 3.7 and the upthrust were also implemented in the effort source (Se) as a modification to the weight.

The bond graph consists of 22 of the repeating units depicted in Figure 3.4. The drill string is fixed at both ends through stiff lateral displacement springs with damping in parallel to remove high frequency transients. An expanded bond graph element is illustrated in Figure 3.15 while Figure 3.16 illustrates the bond graph construction at the interface of two elements. The function of each sub-model is described in the figures, while the simulation files can be accessed through the author's online

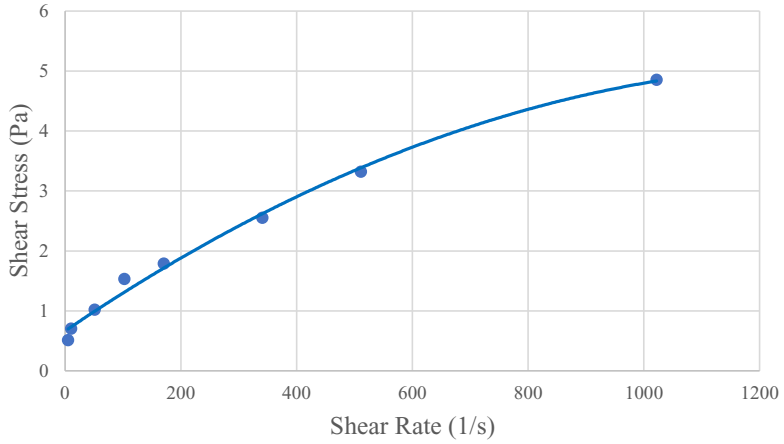

Figure 3.13: Viscometer test results of the non-Newtonian fluid

repository [37]. The three different compliances (i.e. axial, bending, and shear) and the points A, B, and C of a given BG element are illustrated in Figure 3.17. Further information on the development of the bond graph is available in [9] and [6].

The bond graph has a mass imbalance created at the 11^{th} element while an impulse is given at the 10^{th} element. The drill string is rotated with a modified effort source with a PID controller to generate the top drive speed at the first element. Therefore, this bond graph represents a rotating drill string connected to the top drive, which interacts with the wellbore wall. This helps to identify the effect of the damping constant on the bending movement fluctuation.

The interaction with the well bore is detected using a modified capacitive element which resembles stiff springs come in to contact with the BG element when it reaches the well bore. The schematic of a contact spring with a stiffness of k_w is illustrated in Figure 3.18. The stiff spring with discontinuous constitutive laws provide no effort until the eccentricity e exceeds the radial clearance between the well bore and the drill pipe. Further details and relevant equations are presented in [9].

The minimum distance d_{min} is a real-time measurement calculated using the lateral

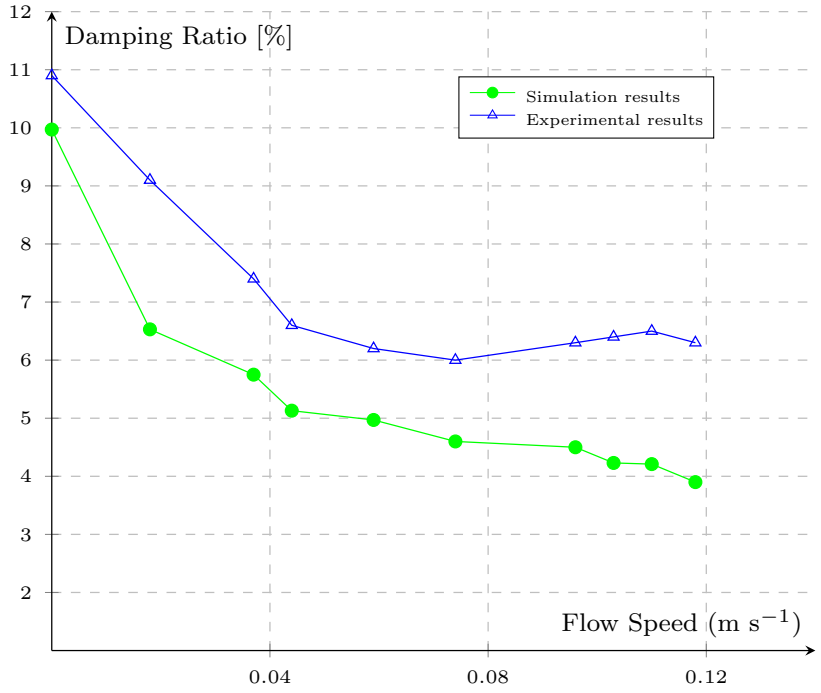

Figure 3.14: Damping ratio change in non-Newtonian fluid

displacement of the respective element. As illustrated in Figure 3.3, the damper ('R' element) was connected at the center of the bond graph element. The lateral displacement is determined by integrating the midpoint velocity. Here the damping constant is the multiplication of the critical damping constant (C_c) and the damping ratio determined by the model. The critical damping constant $(C_c) = 2\sqrt{km}$ where k is the bending stiffness and m is the element's mass. A separate bond graph was developed with constant damping and drag forces. A comparison of the bending moment and axial drag force fluctuations of the models is provided in Figure 3.19 and Figure 3.20 respectively.

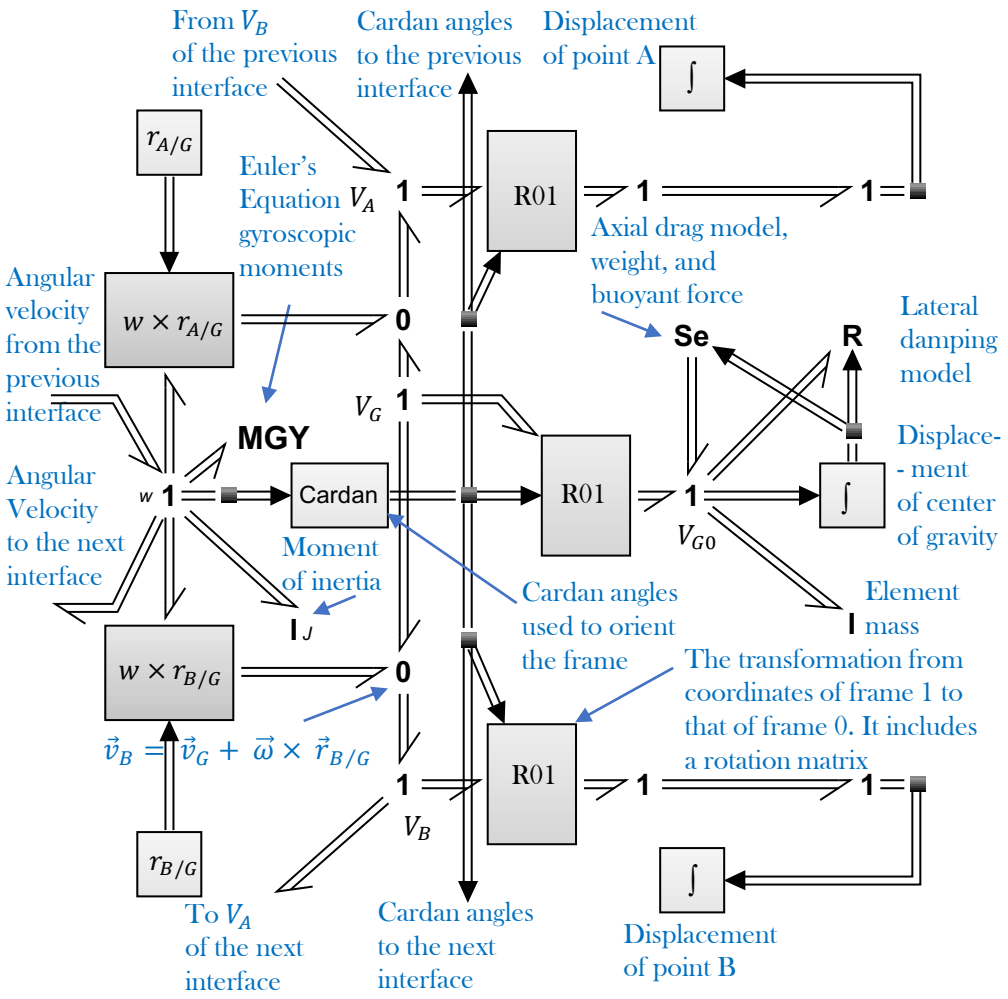

Figure 3.15: 3D bond graph element

3.3.1 Buoyant force model

To complete the evaluation of forces due to drilling fluid, the upthrust or the buoyant force is determined using the fundamental equation of Archimedes' principle (i.e. U=Vρg) where V is the immersed volume of the element, ρ is the density of the drilling fluid, and g is the gravitational acceleration. If the drill string element is fully immersed, V will be constant. It states that the buoyant force is equal to the weight of the displaced fluid by a fully or partially immersed body. Therefore, the change

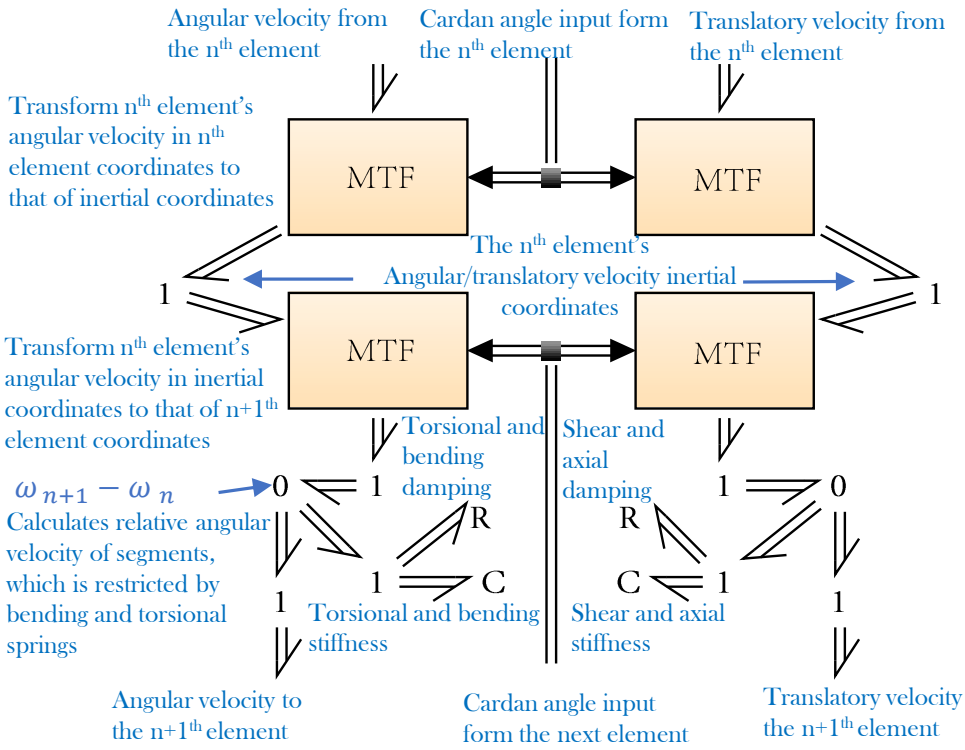

Figure 3.16: Interface between elements

in density of the drilling fluid is the only variable as the change in gravity g with the depth is insignificant with reference to the other forces.

3.4 Discussion

Although there are numerous examples of drill string models in the literature, a study regarding the effect of fluctuating fluid forces on drill strings is rare. Most of the available models do not consider all the contributing variables to the lateral damping and axial drag effects. This study develops and implements a damping model and an axial drag model, considering drilling fluid rheology and the location of the drill string in the wellbore.

Lumped segment models in general consist of rigid bodies connected together with

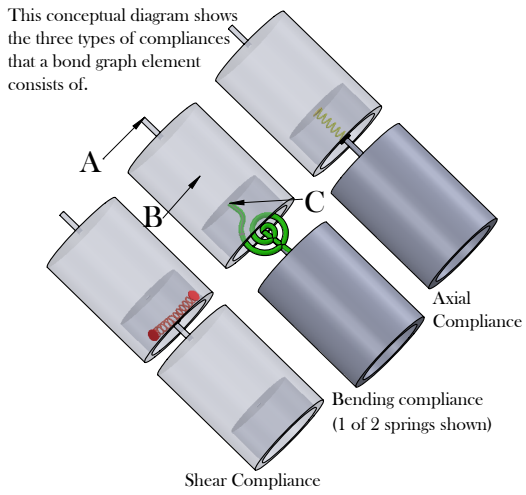

Figure 3.17: Bond graph element compliances

springs and dampers. The FSI simulation used in this study consists of an elastic beam with fixed-fixed end conditions which is still a fair approximation for the following reasons. The lumped segment model element is 10 m in length which resembles an API 5D drill pipe connection beneath two half pipe segments. It is the repeating unit of the lumped segment model shown in Figure 3.4. The wellbore radial clearance is 36 mm in the case study. Therefore, the rotation of the segment about a lateral axis is approximately 1° and can be neglected. Also, the angle is less than 10° for most of the well bore-drill pipe combinations. Furthermore, lateral damping occurs due to the sweeping action of the drill pipe through the drilling fluid. Being a low amplitude vibration, the amount of fluid with which the string interacts in both Figures 3.3.*a* and 3.3.*b* are almost equal. In other words, the sum of distance travelled against the fluid friction by each of the small elements in the respective segment in Figures 3.3.*a* and 3.3.*b* are approximately equal which leads to a similar energy dissipation given that Δx_1 is greater than Δx_2.

The drilling fluid is assumed to behave according to the Hershel-Bulkley model in

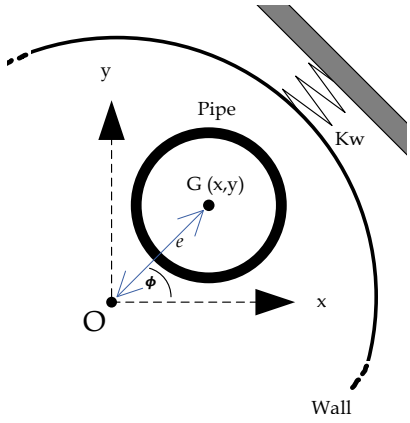

Figure 3.18: Contact spring schematic [9]

the FSI simulations used. The viscometer test results indicate that the fluid used in the physical experiment also follows the same model as shown in Figure 3.13. Nevertheless, the presence of the rock cuttings is considered neither in the simulation nor in the physical experiment, and the drilling fluid is considered a continuum. The relationship between the cutting size distribution and the damping ratio is an open research topic.

The numerical simulation has some limitations when a softer material is used in the structural domain. When the structure material is softer than steel and the density is comparatively low, the added mass effect on the structure's vibration makes the solver unstable, leading to the termination of the simulation. This is a known limitation of the CFD code [38, 39] as of the time of this publication. Note that the link of the citations [38, 39] can be accessed through ANSYS® help only. Therefore, the structural material was selected as steel, and its elastic modulus was manually decreased gradually to find the critical stiffness of the material, which is case-specific, that can run a stable simulation for the current model. It was found that the critical stiffness is 7.5 GPa, nearly 7.5 times that of the physical model made out of Polyethylene (PE). An approximate damping ratio can then be determined from the FSI simula-

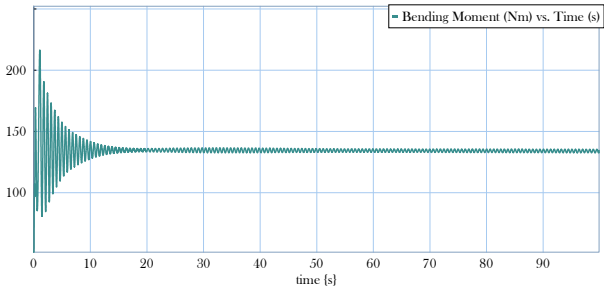

(a) With a fixed damping constant

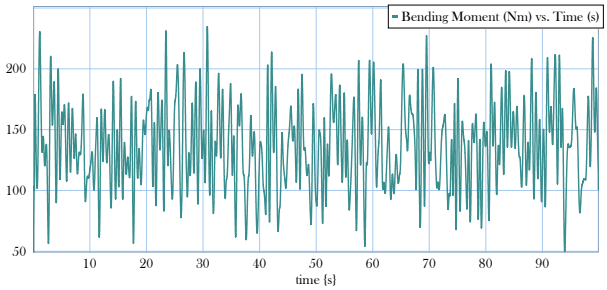

(b) With the developed damping model

Figure 3.19: Bending moment fluctuation

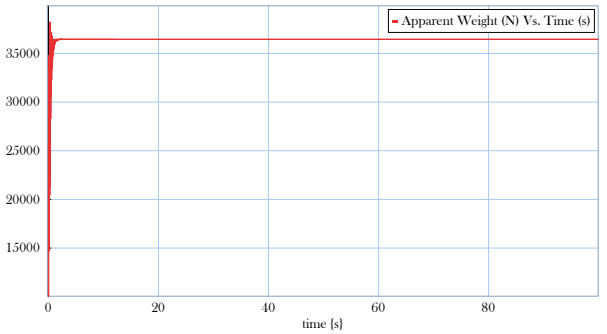

(a) Without an axial drag model

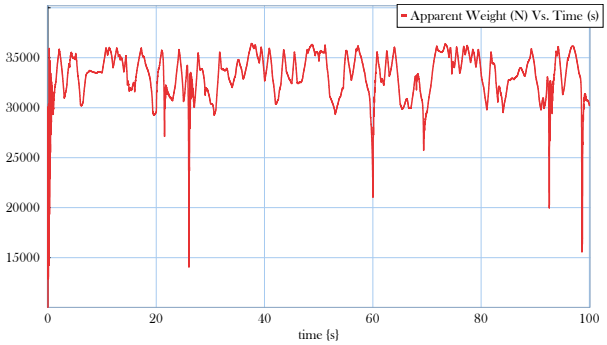

(b) With the developed axial drag modell

Figure 3.20: Drill string's apparent weight fluctuation

tion using logarithmic decrement. As the lateral damping is mainly governed by the work done against the fluid friction, and given that the geometry of the stiffer pipe is identical to that of the actual, the damping ratio was assumed to be approximately equal for lower amplitude vibrations. To improve the confidence of this assumption, the damping ratio of a steel drill pipe connection with a stiffness of 200 GPa was compared against a steel drill pipe with a modified stiffness of 1500 GPa. The stiffer pipe showed a 5-10 % reduction in damping ratio compared to the other. This can be due to the shear-thinning nature of the drilling fluid and the excessive vibration frequency of the stiffened structure.

As a solution for this technical limitation of FSI simulations with softer materials, the use of the Quasi-Newton Stabilization Algorithm and Solution Stabilization option is recommended [38, 39]. Instead of using ANSYS® Workbench for the coupling analysis, the command prompt was used to integrate Transient Structural, Fluent, and System Coupling applications where the Quasi-Newton Stabilization Algorithm is accessible. Alternatively, a manual tuning using the Solution Stabilization option was done. Both attempts were not successful in ANSYS® 2021 R2, and ANSYS® 2022.

Although there is not much effect on the vibration amplitude decay, the elastic modulus increase causes mismatches in the damping ratio and natural frequencies. When the vibration amplitude is in the 0 to 1 mm range, the effect of the boundary layer adjacent to the pipe's outer surface becomes considerable compared to higher amplitude cases. It can cause differences between the experimental and simulation results. On the other hand, the stiffer structure shows a higher natural frequency as expected. Therefore, the natural frequency of the simulation results shows a higher value compared to that of the experimental results. Further, as shown in Figure 3.21, the natural frequency becomes stable after 0.075 ms^{-1}. This transition occurs when the

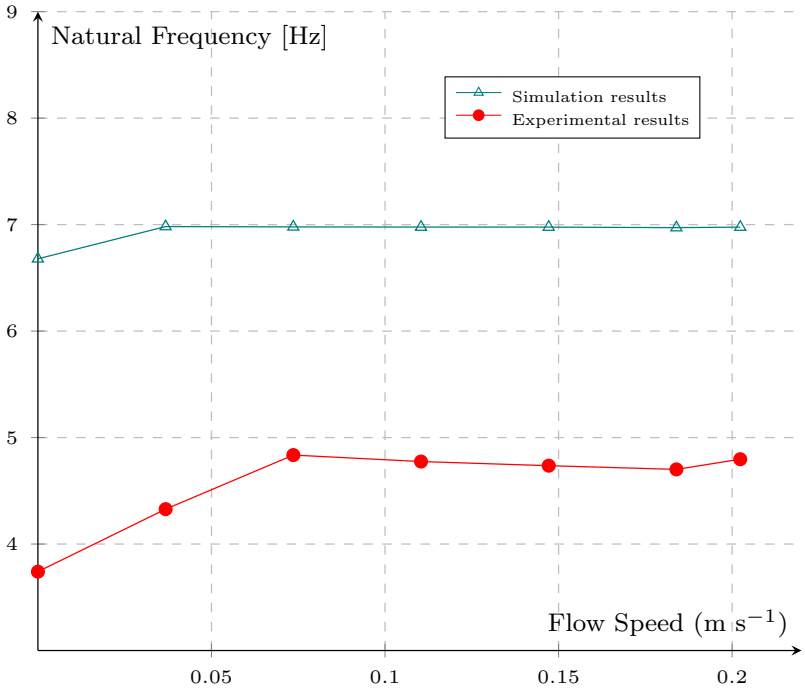

Figure 3.21: Natural frequency vs. fluid velocity

annular flow reaches the critical Reynold's number that can be verified based on the findings of [40]. According to [40], the critical Reynold's number for the radius ratio can be approximately estimated as 2350, referring to Figure 3.22. On the other hand, Reynold's number for the flow velocity of 0.075 ms^{-1}, where the transition occurs, can be calculated using Equation 3.8. It was found that both Reynold's numbers are almost equal. This verifies that the variation of natural frequency is due to the transition from laminar to turbulent flow.

$$Re = \frac{2U\rho(R_1 - R_2)}{\mu} \tag{3.8}$$

Figure 3.23 depicts that the variation of fluid velocity inside the annular space with reducing d_{min} or increasing eccentricity e. The maximum velocity in the annular region varies with eccentricity, creating changes in the viscous and inertial fluid forces

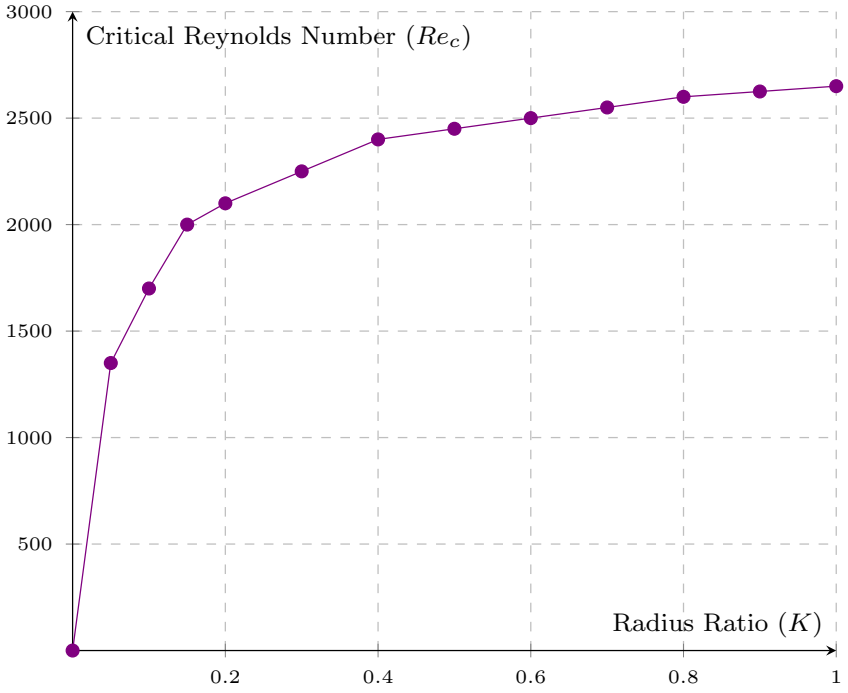

Figure 3.22: Radius ratio vs. Reynolds number [40]

acting on the drill pipe. This verifies the importance of incorporating d_{min} into the damping and drag models. As shown in Figure 3.19, models with fixed damping constants underestimate the bending moment fluctuation at lower speeds. This becomes critical when the drill string is under stick-slip vibration because the speed goes to the lower extreme periodically. On the other hand, at speeds around 50 rpm, the bond graph model with a fixed damping constant showed greater well bore interaction than the bond graph model with variable damping. This indicates that the implemented damping model captures the effect of the lateral displacement and the drilling fluid properties and brings it into the drill string vibration response. This shows the potential to improve the prediction accuracy of stress fluctuations and wellbore interaction for a given drill pipe, if a continuously variable damping model is used. It will benefit applications such as fatigue life prognosis of drill strings.

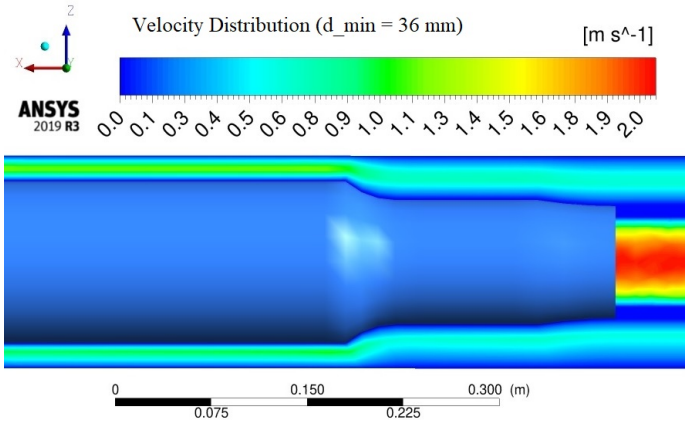

(a) Concentric with the well bore

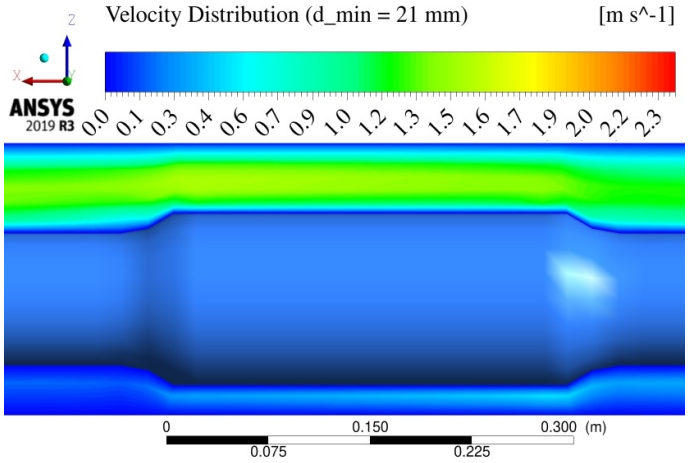

(b) Eccentricity: 15 mm

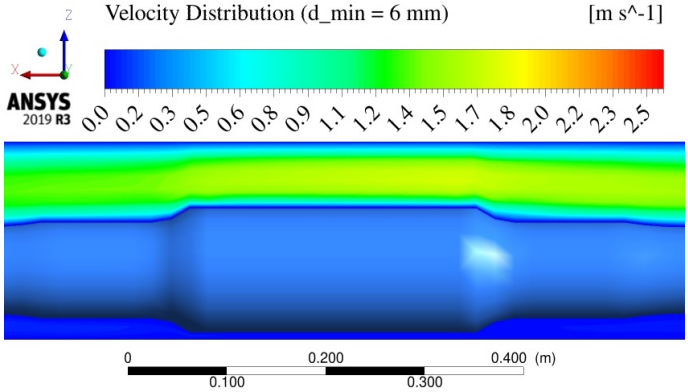

(c) Eccentricity: 15 mm

Figure 3.23: Velocity distribution with the changing eccentricity
(Figures illustrate the change in maximum velocity with increasing eccentricity)

Also, this model can estimate the apparent fluctuating weight of the drill string due to the drilling fluid flow. This facilitates estimating fluctuating WOB of a vertical drill string. For deviated well applications, a friction model can be implemented to bring the contact forces' contribution into the equation.

In Figure 3.19.a, it can be seen that the amplitude of vibration gradually decays and approaches a fixed value. This is because the drill string is pin joined at the ends, and a mass imbalance comes into action with the implementation of the angular velocity. The mass imbalance pulls the drill string laterally, creating a consistent bend on the entire drill string. Also, the periodic vibration is due to the external impulse given at the 10^{th} element. Although the same conditions are provided, the second bond graph with the damping model shows a different bending moment fluctuation with a lower decay.

3.5 Conclusions

A detailed methodology is presented to develop models to determine the instantaneous damping constant and the axial drag force for a given oilwell drill string. The damping models were developed for a drill string with API 5D drill pipes using a series of FSI simulations followed by statistical analysis. The models were implemented in a lumped segment multibody model to demonstrate the importance of treating fluid damping effects with greater complexity than is typical in the literature. Both bending moment fluctuation and the overall axial force is affected by the properties and velocity of the drilling fluid and the instantaneous location of the drill string in the well bore. It was observed that the bending moment fluctuation is underestimated at lower rotational speeds, and the well bore interaction is exaggerated at higher rotational speeds. Therefore, fixed values for the damping constant and axial

drag may underestimate important predictions such as remaining useful fatigue life and WOB. Damping and axial drag models developed using the methods of this paper are recommended in drill string lumped-segment simulation models, taking in to account the drilling fluid rheology, instantaneous location of the drill string in the wellbore, drill pipe geometry, and the drilling fluid velocity.

3.6 Further work

The numerical values in damping models presented in this study apply only to the geometry of an API 5D drill pipe. Further studies can be made to develop a technique to adopt the current models to other drill pipe geometries without requiring a total re-derivation of the model. This can be achieved by performing a series of simulations for different diameters. The outcome may be a chart that can determine a modifying factor for the current models, eliminating or reducing the FSI simulations, which are highly time-intensive.

The shape of the damping curve for increasing velocity indicates a characteristic shape for both Newtonian and non-Newtonian fluids as shown in Figures 3.21 and 3.14 respectively, which can be further explored. Also, investigating the effect of rock cuttings with different size distributions on the drill string damping will be a valuable contribution. Further, the damping and the axial drag models can be implemented in a directional well model to investigate the changes in vibration behaviours.

3.7 Acknowledgments

The authors thankfully acknowledge the financial support provided by the Natural Sciences and Engineering Research Council (NSERC) of Canada and Memorial Uni-

versity of Newfoundland, Canada.

References

[1] S. Chen, "Fluid damping for circular cylindrical structures," *Nuclear Engineering and Design*, vol. 63, no. 1, pp. 81–100, 1981.

[2] W. Tucker and C. Wang, "An integrated model for drill-string dynamics," *Journal of sound and vibration*, vol. 224, no. 1, pp. 123–165, 1999.

[3] B. J. J. and I. Finnie, "An analytical study of drill-string vibration," *Journal of Engineering for Industry*, vol. 82, pp. 122–127, 5 1960.

[4] M. P. Paidoussis and N. Issid, "Dynamic stability of pipes conveying fluid," *Journal of sound and vibration*, vol. 33, no. 3, pp. 267–294, 1974.

[5] M. P. Paidoussis, *Fluid-structure interactions: slender structures and axial flow*, vol. 1. Academic press, 1998.

[6] M. Sarker *et al.*, *Modeling and simulation of vibration in deviated wells*. PhD thesis, Memorial University of Newfoundland, 2017.

[7] Q. Qian, L. Wang, and Q. Ni, "Vibration and stability of vertical upward-fluid-conveying pipe immersed in rigid cylindrical channel," *Acta Mechanica Solida Sinica*, vol. 21, no. 5, pp. 331–340, 2008.

[8] M. Paı, T. Luu, S. Prabhakar, *et al.*, "Dynamics of a long tubular cantilever conveying fluid downwards, which then flows upwards around the cantilever as a confined annular flow," *Journal of Fluids and Structures*, vol. 24, no. 1, pp. 111–128, 2008.

[9] D. G. Rideout, A. Ghasemloonia, F. Arvani, and S. D. Butt, "An intuitive and efficient approach to integrated modelling and control of three-dimensional vibration in long shafts," *International Journal of Simulation and Process Modelling*, vol. 10, no. 2, pp. 163–178, 2015.

[10] X. hua Zhu and B. Li, "Numerical simulation of dynamic buckling response considering lateral vibration behaviors in drillstring," *Journal of Petroleum Science and Engineering*, vol. 173, no. September 2018, pp. 770–780, 2019.

[11] R. T. G., S. C., and S. R., "Non-linear dynamics of a drill-string with uncertain model of the bit-rock interaction," *International Journal of Non-Linear Mechanics*, vol. 44, no. 8, pp. 865–876, 2009.

[12] F. Arvani, M. M. Sarker, D. G. Rideout, and S. D. Butt, "Design and development of an engineering drilling simulator and application for offshore drilling for MODUs and deepwater environments," *Society of Petroleum Engineers - SPE Deepwater Drilling and Completions Conference 2014*, pp. 417–433, 2014.

[13] M. Sarker, G. Rideout, and S. Butt, "Dynamic model for longitudinal and torsional motions of a horizontal oilwell drillstring with wellbore stick-slip friction," *Journal of Petroleum Science and Engineering*, vol. 150, pp. 272–287, 2017.

[14] D. Xie, Z. Huang, Y. Ma, V. Vaziri, M. Kapitaniak, and M. Wiercigroch, "Nonlinear dynamics of lump mass model of drill-string in horizontal well," *International Journal of Mechanical Sciences*, vol. 174, p. 105450, 2020.

[15] F. V. P., "Vibrations and stability of a pipe when liquid flows through it," *Inzhenernyi Sbornik*, vol. 10, no. 1, pp. 69–70, 1951.

[16] G. Housner, "Bending vibrations of a pipe line containing flowing fluid," *The ASME Journal of Applied Mechanics*, 1952.

[17] F. I. Niordson, *Vibrations of a cylindrical tube containing flowing fluid.* Lindst hl, 1953.

[18] C. S, W. M.W, and J. JA, "Added mass and damping of a vibrating rod in confined viscous fluids," *American Society of Mechanical Engineers*, 1976.

[19] M. R, *The Effects of Frequency and Amplitude of Oscillation on the Hydrodynamic Masses of Irregular Shaped Bodies.* University of Rhode Island, 1965.

[20] C. R., "Added Mass and Damping for Cylinder Vibrations Within a Confined Fluid Using Deforming Finite Elements," *Journal of Fluids Engineering*, vol. 109, pp. 283–288, 09 1987.

[21] E. Kjolsing and M. Todd, "Damping of a fluid-conveying pipe surrounded by a viscous annulus fluid," *Journal of Sound and Vibration*, vol. 394, pp. 575–592, 2017.

[22] F. Liang, Y. Qian, Y. Chen, and A. Gao, "Nonlinear forced vibration of spinning pipes conveying fluid under lateral harmonic excitation," *International Journal of Applied Mechanics*, p. 2150098, 2021.

[23] I. R. A., "Overview of mechanics of pipes conveying fluids-part I: Fundamental studies," *Journal of Pressure Vessel Technology, Transactions of the ASME*, vol. 132, no. 3, pp. 0340011–03400132, 2010.

[24] G. Rideout, A. F, S. Butt, and F. E, "Three-dimensional multi-body bond graph model for vibration control of long shafts-application to oilwell drilling," *Proc.*

Integrated Modeling and Analysis in Applied Control and Automation, pp. 25–27, 2013.

[25] H. Qiu, J. Yang, S. Butt, and J. Zhong, "Investigation on random vibration of a drillstring," *Journal of Sound and Vibration*, vol. 406, pp. 74–88, 2017.

[26] Y. Khulief and H. Al-Naser, "Finite element dynamic analysis of drillstrings," *Finite elements in analysis and design*, vol. 41, no. 13, pp. 1270–1288, 2005.

[27] Y. Khulief, F. Al-Sulaiman, and S. Bashmal, "Vibration analysis of drillstrings with string—borehole interaction," *Proceedings of the Institution of Mechanical Engineers, Part C: Journal of Mechanical Engineering Science*, vol. 222, no. 11, pp. 2099–2110, 2008.

[28] Y. Khulief and F. Al-Sulaiman, "Laboratory investigation of drillstring vibrations," *Proceedings of the Institution of Mechanical Engineers, Part C: Journal of Mechanical Engineering Science*, vol. 223, no. 10, pp. 2249–2262, 2009.

[29] S. Scampoli, "High-Fidelity Fluid-Structure Interactions," 2012.

[30] W. C. Young, R. G. Budynas, and A. M. Sadegh, *Roark's formulas for stress and strain*, vol. 7. McGrawHill, 8 ed., 2002.

[31] M. Douglas, *Design and analysis of experiments*. John Wiley & Sons, 2017.

[32] M. F. Islam and L. Lye, "Combined use of dimensional analysis and modern experimental design methodologies in hydrodynamics experiments," *Ocean Engineering*, vol. 36, no. 3-4, pp. 237–247, 2009.

[33] M. J. Anderson and P. J. Whitcomb, *RSM simplified: optimizing processes using response surface methods for design of experiments*. Productivity press, 2016.

[34] A. Y. Aydar, "Utilization of response surface methodology in optimization of extraction of plant materials," in *Statistical Approaches With Emphasis on Design of Experiments Applied to Chemical Processes* (V. Silva, ed.), ch. 10, Rijeka: IntechOpen, 2018.

[35] R. M. R., *Exploration and Production of Petroleum and Natural Gas*. ASTM International, 2016.

[36] ANSYS, "Ansys fluent 12.0 user's guide - 12.13.19 modeling turbulence with non-newtonian fluids," 2009.

[37] M. G. Don, "Github - mihiranpathmika/bond-graph-simulations: Bond graph simulation files with constant damping and the damping model developed.."

[38] Ansys, "FSI is not working for soft materials — ANSYS learning forum," 2020. Accessed: 2022-04-10.

[39] Ansys, "2-way fsi fails during first time step — Ansys learning forum," 2022. Accessed: 2022-04-10.

[40] D. H, K. B, and T. H, "Determining the critical condition for turbulent transition in a full-developed annulus flow," *Journal of Petroleum Science and Engineering*, vol. 73, no. 1-2, pp. 41–47, 2010.

Chapter 4

Fatigue Failure Prognosis of an Oil Well Drill String Using a Lumped Segment Bond Graph Model and Finite Element Method

Abstract

A novel methodology for fatigue failure prognosis of oil well drill strings is introduced which uses less computation power. A multibody dynamic BG model of a drill string and a finite element model are employed to estimate the remaining cumulative fatigue life of the drill string. The drill string with 2D lateral vibration and axial vibration is modelled in the 20 sim™ bond graph simulation environment with a body-fixed coordinate system. Drill string collision with the wellbore caused by a rotating imbalance is included in the BG model. Concurrently, a Computer-Aided Design model of the drill string is developed using Ansys® Structural, and it is then used in finite element Analysis to determine the bending, axial, and shear compliances of each BG segment. The refined BG provides the bending moment history of the drill string back to the finite element model to evaluate the remaining fatigue life.

keywords: *Bond graph, cumulative fatigue, oil well drill strings, Finite Element Method*

Co-authorship Statement

This chapter is a manuscript of a full paper that is published in 14th International Conference on Bond Graph Simulations (ICBGM) 2021, California, USA. The co-authorship statement for this chapter follows:

The declaration applies to the following article
M. Galagedarage Don and Geoff Rideout, "*Fatigue Failure Prognosis of an Oil Well Drill String Using a Lumped Segment Bond Graph Model and Finite Element Method*". 14th International Conference on Bond Graph Simulations (ICBGM)2021 Nov 8-10, 2021- San Diego, California, USA. **Article status: Published** The PhD student analyzed the literature, performed the experiments, collected the data, developed the codes and prepared the manuscript. The supervisor edited, helped organize the manuscript, and contributed to the choice of case studies.

4.1 Introduction

4.1.1 The need for a fatigue failure prognosis technique

The urgent need for a fatigue failure prognosis technique has been present in the oil and gas drilling industry for several decades. As mentioned in [1], 76 drill-string failures from 1987 to 1990 on three continents have been investigated. As illustrated in Figure 4.1, fatigue was estimated as the primary cause of 65 % of these failures and had a significant impact on 12% of them. The other factors, such as excessive tension and torque, and low toughness of the material, were secondary causes of failures in comparison with fatigue. Supporting the above statistics, [2] has mentioned that more than 50% of the drill string failures have occurred due to fatigue failure of the drill pipes. According to [3], during the same period, drill-string failures have occurred in 14% of all drill-rig systems and cost approximately US$ 100k each time the system

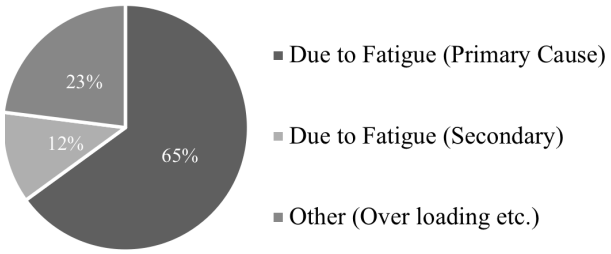

Figure 4.1: Drill string failures reported from 1987 to 1990 [1]

experienced a failure. Although the mechanisms of failures are well known and can be explained, the failure of drill strings still occurs. The prediction of drill pipe failure has become difficult because of the complex loading, severe vibrations, and the erosive and corrosive behaviour of the drilling mud [4]. Therefore, the risk associated with drill string failure remains high in terms of probability of occurrence and the cost involved. This has motivated fatigue failure prognosis techniques of drill-strings.

4.1.2 The reasons for fatigue failure of drill strings

Drill-strings used in oil drilling are subjected to complicated stresses due to excess vibration caused by bit bounce, stick-slip, and lateral forward or backward whirl with wellbore contact [5]. These complex stresses make the drillstring vulnerable to failure due to cumulative fatigue. As described by [4], there are seven identified reasons for the initiation and propagation of fatigue cracks: surface irregularities; removal or flaking of drill pipe internal coating; drill string vibrations; frictional heating; stress corrosion cracking; sulfide stress cracking; and material defects during machining and heat treatment. Threaded connections in drill pipes are highly prone to stress concentration, which leads to fatigue crack initiation. This fact is highlighted in several studies including [6], [7], and [8]. Therefore, it is a must to consider the

behaviour of threaded connections in fatigue failure prognosis.

4.1.3 The requirement of a hybrid model for fatigue prognosis

Fatigue failure prognosis can be performed following a numerical approach, such as FEA. Nevertheless, there can be constraints because of excessive simulation times [5]. On the other hand, a lower order BG model of a drill string may be able to predict the vibration behaviour of a drill string, but the localized stress and strain need to be calculated theoretically in post processing. The accurate theoretical calculation of localized stress becomes almost impossible when the geometries become complicated due to the presence of threaded connections and variable wall thicknesses. This can be handled using an finite element model, by employing it in virtual experiments to determine the relevant material behaviours. Therefore, a combined approach of finite element model and BG model is proposed to achieve this goal.

4.1.3.1 Fatigue estimation techniques

Fatigue life estimation of engineering components is an area with a number of open research topics. According to [9], there are three main methods in fatigue analysis namely, strain-life, stress-life, and fracture mechanics.

The stress-life approach is ideal for high cycle fatigue damage estimation, which involves more than 10^5 cycles. Therefore, it is suitable to estimate the fatigue damage of drill pipes. This is performed based on empirical S-N curves and then modified by a variety of factors. Although the crack initiation and propagation are not separately identified, the method is suitable to determine the overall fatigue life of an engineering component. Hence, the stress-life method is used in this study.

Strain is directly measurable using strain gauges and has been identified as an excellent quantity for characterizing low cycle fatigue. This employs strain-life relation equations instead of S-N curves. Crack initiation and the critical plane of facture are important factors in this approach. Although the strain-life approach has several other advantages over the stress-life approach, low cycle fatigue estimation of materials which undergo considerable amount of plastic deformation is the most suitable application area of this technique [9].

In the fracture mechanics approach, it is assumed that a flaw of a specific maximum size can be present anywhere in the component. It can be inside the material or on the surface. The propagation of the crack is determined based on the stress fluctuations acting on the body. The strength of this method is that the user can make decisions on the inspection intervals and scheduled maintenances. The maximum possible flaw size estimation is necessary which requires a non-destructive test (NDT) procedure [9].

According to the classification given in [10] the three main categories of fatigue problems are: completely reversing simple loads; fluctuating simple loads; and combinations of loading modes. Completely reversed single stress situations can be handled with the S-N diagrams, relating the alternating stress to life. Only one type of loading is allowed here while the midrange stress must be zero. In the case of fluctuating simple loads, general fluctuating loads can be incorporated using a criterion to relate midrange (σ_m) and alternating stresses (σ_a). Criteria such as modified Goodman, Gerber, ASME-elliptic, or Soderberg can be employed while only one type of loading is allowed at a time. When there is a combination of loading modes such as combined bending, torsion, and axial it is required to determine the equivalent von Mises stresses for midrange stress (i.e. σ'_m) and alternating stress (i.e. σ'_a). Equations 4.1 and 4.2 can be incorporated to determine these parameters and a suitable fatigue

criterion can be employed to complete the fatigue analysis.

$$\sigma'_m = \{[K_{fB}\ \sigma_{mB} + K_{fA}\ \sigma_{mA}]^2 + 3[K_{fsT}\ \tau_{mT}]^2\}^{1/2} \tag{4.1}$$

$$\sigma'_a = \{[K_{fB}\ \sigma_{aB} + K_{fA}\ \sigma_{aA}/0.85]^2 + 3[K_{fsT}\ \tau_{aT}]^2\}^{1/2} \tag{4.2}$$

where subscript A, B, and C stand for axial, bending and torsion while K_f and K_{fs} stand for normal and shear modification factors respectively. The Rainflow counting technique and S-N curve can be employed to estimate the number of cycles and determine the fatigue damage respectively [11].

In summary, fatigue life prognosis involves two stages: 1.) determination of stress history undergone by a given structure, and 2.) fatigue damage calculation. Stress history can be efficiently and effectively determined using a bond graph simulation of the vibrating structure. The stress history can then be analyzed to determine the fatigue damage by employing a software code developed based on the first principles or a finite element model.

4.2 Methodology

The overview of the entire study is illustrated in Figure 4.2. Initially, two simulation models, bond graph (BG) and Finite Element, are employed. Detailed explanations on the two models are presented in Sections 4.2.1 and 4.2.2. The finite element model, which simulates a drill string repeating unit, is used to determine the axial, shear, and bending compliances. This was performed based on virtual experiments. Those compliance values are then used to refine the BG as the first step. The BG model was validated using established theoretical calculations and using static deflection and dynamic response analysis. The BG model generates a bending moment history

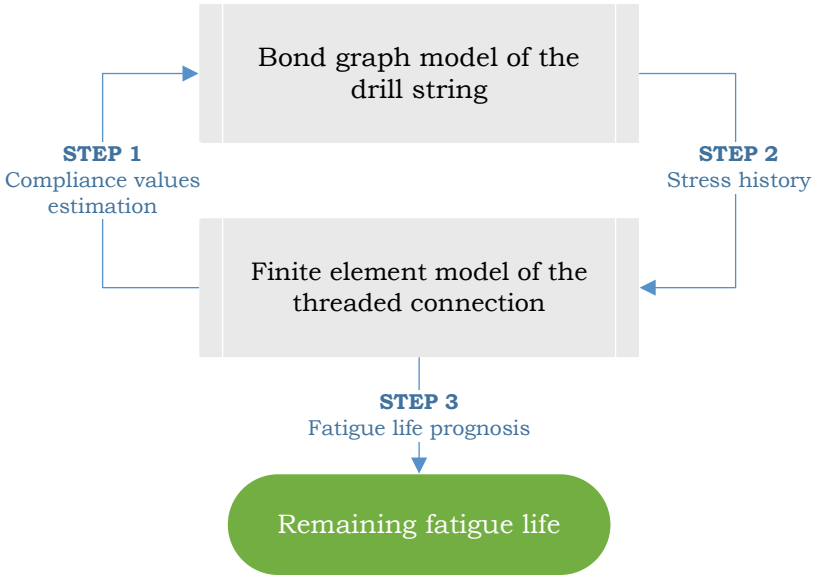

Figure 4.2: Overview of the approach

of the entire drill string of 100 m. This bending moment history is then fed back to the finite element model as history data to be used in Fatigue Tool of Ansys® Structural for fatigue life prognosis. The estimated fatigue life through simulation was verified using standard stress-life analytical calculations through the development of a Matlab®.

4.2.1 The finite element model

The FEA was done for the repeating unit of the drill string shown in Figure 4.3.a. The repeating unit is developed based on the schematic diagram of the drill string illustrated in Figure 4.4. It is an API 5D standard drill pipe with an outer diameter of 84 mm. The material is E75 Carbon Steel while the type of end finish is 'internal and external upset'. The middle part of the repeating unit consists of the threaded

box and pin with two equal pipe segments connected to it. The element size was decided after conducting a grid dependency test and the minimum size of the element was determined as 5×10^{-3} m considering the processing speed and convergence of the results.

The finite element model was used to fulfill two main requirements: firstly, to determine the compliance values and secondly to determine the remaining fatigue life based on the bending moment history as given by the BG model.

In determining the axial compliance, the element was cantilevered and subjected to a 1 mm axial displacement (e_a). The reaction force (F_a) at the fixed end was measured using the probe tool. The stiffness (K_a) is the F_a per unit e_a, and the axial compliance (C_a) is the reciprocal of K_a. Following a similar approach, the shear compliance (C_s) was determined for a pipe segment and the threaded section separately. Short segments were taken to avoid bending effects while applying the shear force. The overall shear compliance was determined considering that the assembly is equivalent to springs in series. Determination of the bending compliance (C_b) is not straightforward in comparison with the previous two. The cantilevered repeating unit was given a known bending moment, and the rotation of the cross-sections close to the free end was considered as illustrated in Figure 4.5.

The displacements of the points were drawn with high precision using AutoCAD® software and the angles of plane rotations were measured.

If the rotation of two cross-sections are $\phi(x)$ and $\phi(x + \Delta x)$, according to [13], the relationship between the applied bending moment (M) and the difference of the two rotations of the planes can be presented by Equation 4.3. This is illustrated in Figure 4.6. Therefore, the bending compliance ($\Delta x/EI$) is the required M for a unit change in $\phi(x + \Delta x) - \phi(x)$. The rotations of the cross-sections were determined by measuring the displacements of specific nodes, and the bending moment was probed

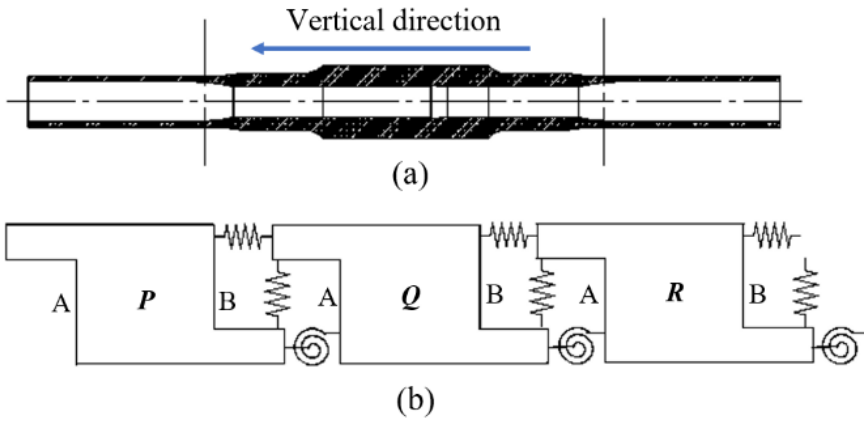

Figure 4.3: Discretization of the repeating unit (not to scale)

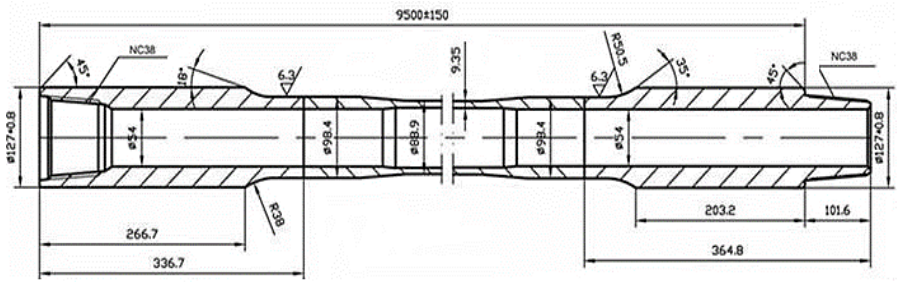

Figure 4.4: Schematic diagram of the drill pipe [12]

at the fixed end. The results of each compliance are presented in Table 4.1.

$$M = \frac{EI}{\Delta x}[\phi(x + \Delta x) - \phi(x)] \tag{4.3}$$

The compliance values and the remaining fatigue life determined through the finite element model were compared with the theoretical calculations.

4.2.2 The bond graph model

The bond graph model is provided with pinned-pinned boundary condition by providing stiff springs ($i.e.10^8\ Nm^{-1}$) at both the ends along with high damping coefficients

($i.e.10^4\ Nm^{-1}$). A zero-flow source is provided to keep the velocity at both ends zero. This is illustrated in Figure 4.7. Only the y velocity component is shown for clarity.

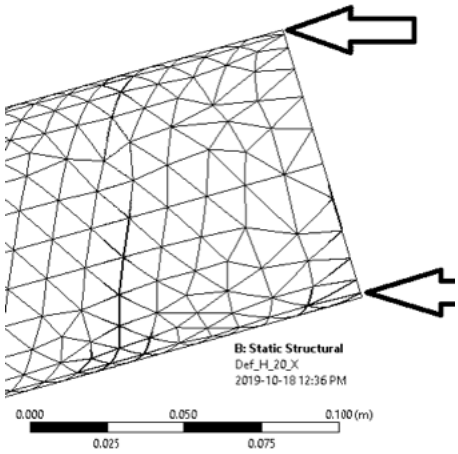

Figure 4.5: Bending stiffness determination experiment

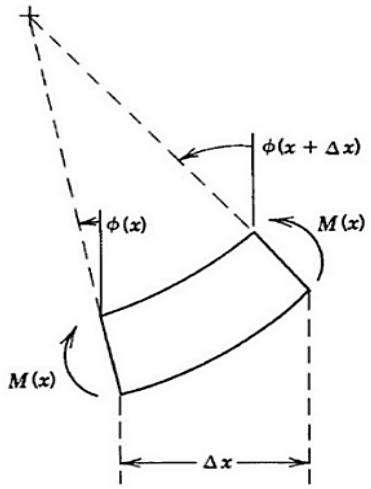

Figure 4.6: Plane rotation [13]

As shown in Figure 4.3.b, the repeating unit of the drill string is discretized into three elements to be used in the BG. The element at the middle (Q) represents the threaded connection region with the varying wall thickness while the rest of the two

(P and C) represent two similar pipe segments welded to the threaded connection. Other parameters used to implement the BG are tabulated in Table 4.1. Figure 4.8 illustrates the repeating unit of the 'Drill Pipe' indicated in Figure 4.7. There are thirty similar units inside the submodel 'Drill Pipe'. Nevertheless, the compliance values are not equal in all the elements as some represent the threaded connection while the others represent the pipe segments. As shown in Figure 4.8, the repeating unit consists of the interface submodel and 2D element submodel. The function of the interface block is matching the lower endpoint (B) velocity values of the n^{th} element to the top end (A) velocity values of the $(n+1)^{th}$ element. In other words, the body-fixed velocity of the n^{th} element is converted to the velocity in the body-fixed coordinate system of the $(n+1)^{th}$ element. The BG model of the Interface (n) block in Figure 4.8 is presented in Figure 4.9. A detailed illustration of the 'Element (n)' submodel is given in 4.10. As shown, there are five terminals to that 2D model where two of them are for the top end translational velocities, another two for the bottom end translational velocities, and finally one is for angular velocity about the z body fixed axis. A detailed explanation of this 2D element model can be found in [14]. As shown in Figure 4.8, the angular velocities of each element are integrated and the difference of two integrals is taken at the summing junction. This provides the required input to the interface model. Further, in Figure 4.8, there are shear and axial compliances introduced at all the one junctions connected to the elements. Those two types are connected to the one junctions which represent x and y components of velocities, respectively. The model does not include frictional effects generated from the wellbore drill string interaction. Nevertheless, the impact with the wellbore is simulated with the use of nonlinear contact springs on each lumped segment.

In, Figure 4.8, the 'well bore compliance' is employed for this purpose. It is coded such that the drill string experiences a force of, $k_{contact}.\delta$, transverse to the drill string,

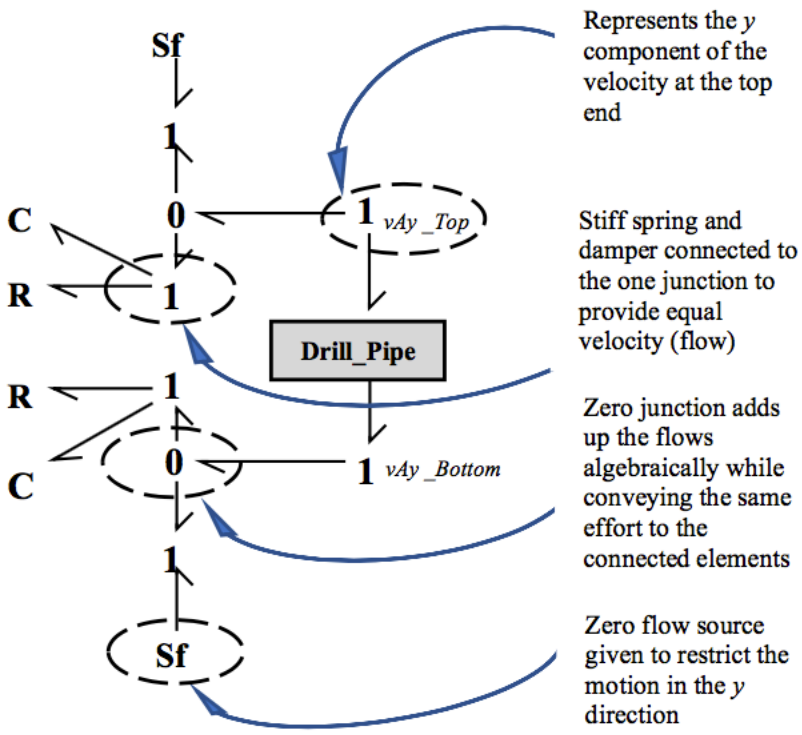

Figure 4.7: Boundary conditions of the BG

when the displacement in the y direction is greater than or equal to the radius of the well bore. This condition creates a positive interference δ. The force is set to be zero in other instances.

The vibration excitation was given to the bond graph using a modulated source of effort (MSe) with a sinusoidal signal input with an amplitude of 25 N and angular velocity (ω) of 10.4 rad/s. The effort was given laterally, in the y direction, by connecting it with a power bond to a one junction which connects a drill pipe element and an interface of the bond graph. This effort is equivalent to a 25 N centrifugal force acting in the drill string, which may be caused due to a mass imbalance or buckling of drill pipes.

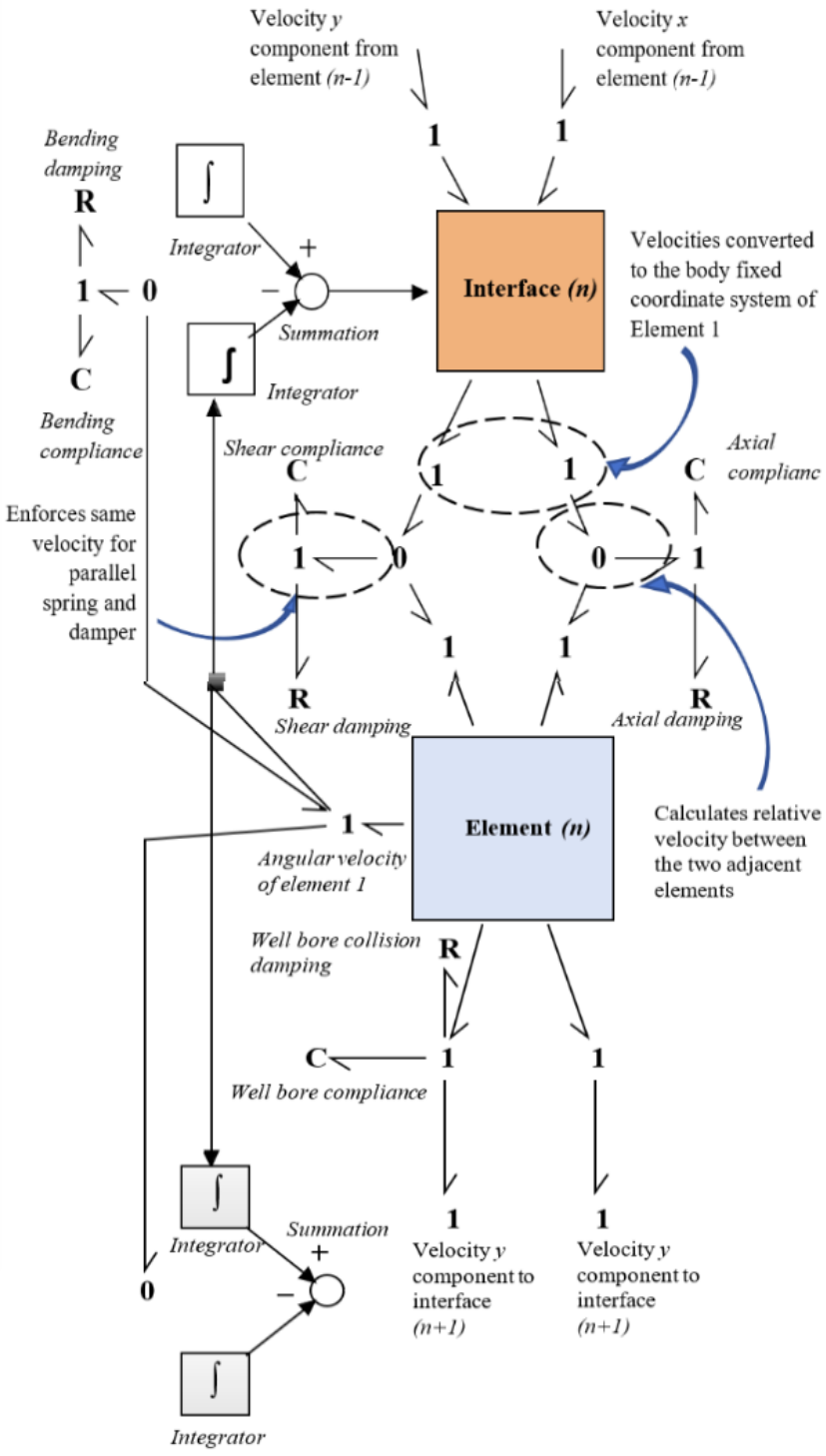

Figure 4.8: Repeating unit of the BG

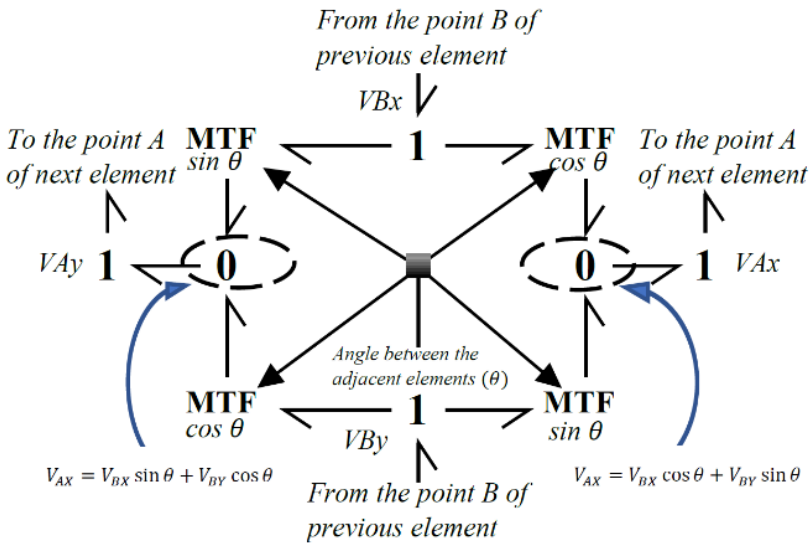

Figure 4.9: BG model of the interface

4.2.3 Fatigue life estimation

Initially, fatigue life prognosis was performed using Ansys® Fatigue Tool, after simplifying the problem into a 'variable amplitude proportional loading' case. The simplification was possible as the point of interest in the drill string was close to the midpoint. This is because the 'mass imbalance' was located at the centre of the drill string. This region of the drill string has near zero tensile stress as no external axial thrust was included in the simulation.

In the Ansys® fatigue simulation, the scale factor was set to 1 as the finite element model was simulated for unit bending moment so the historical data need not be normalized. The BG was simulated for a known time period (10 *sec*) and the bending moment fluctuation was saved in a '.dat' file. Then the finite element model was simulated with a unit bending moment (i.e. 1 Nm) using Ansys® Static Structural. The simulated bending moment fluctuation from BG model shown in Figure 4.13 was then imported into the Ansys® Fatigue Tool to estimate the fatigue life. Figure 4.11

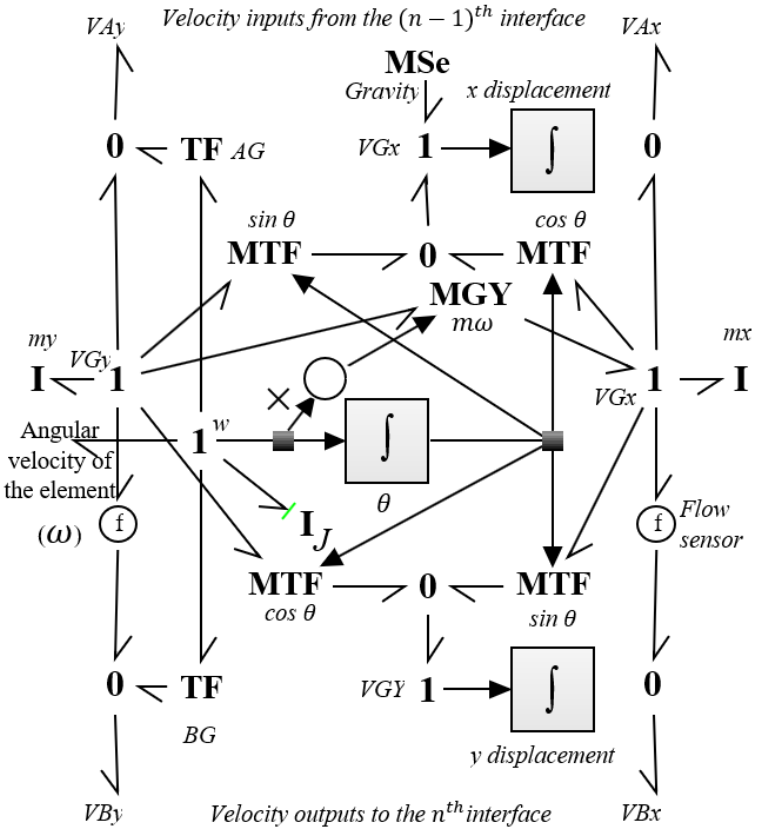

Figure 4.10: BG model of the 2D element

shows the sample bending moment fluctuation history exported from the BG model.

The fatigue life was also estimated using the stress-life approach presented in [10] for a pure bending moment situation for verification. This was coded using Matlab® and can be expanded to analyze a case where torsional and axial loadings are also considerable. The code takes the bending moment variation history from the BG model and performs rain flow counting to determine the mean and the range of the stress fluctuation as shown in Figure 4.12. Then it follows the standard calculation while considering the endurance limit modifying factors such as surface condition, size, load, and temperature. The same set of parameters and material data were used in Ansys® Fatigue Tool to estimate the fatigue damage.

Table 4.1: Specifications of the drill string segment used for simulation

Drill string parameters	**Value**	**Unit**
Pipe outer radius (r_p)	4.4×10^{-2}	m
Pipe segment length (L)	4.3×10^{0}	m
Threaded segment length (L_t)	7.6×10^{-1}	m
Pipe axial compliance (C_A)	9.2×10^{-9}	mN^{-1}
Threaded segment axial compliance (C_{At})	6.8×10^{-10}	mN^{-1}
Pipe element bending comp (C_B)	3.8×10^{-8}	rad/Nm
Threaded segment bending compliance (C_{Bt})	8.3×10^{-9}	rad/Nm
Pipe shear compliance (C_S)	5.1×10^{-8}	mN^{-1}
Threaded segment shear compliance (C_{St})	6.7×10^{-9}	mN^{-1}
Well-bore contact stiffness $K_{contact}$	1.0×10^{-6}	Nm^{-1}

The Matlab® code, BG, and finite element models are available in the author's online repository which can be accessed through the this link:(https://github.com/mihir anpathmika) and in Appendix A. The fatigue strength factor (K_F) was taken as 0.9 and stress-life approach was employed with Gerber mean stress theory in both approaches. The analytical and Ansys® simulation results are closely in agreement and are presented under results and discussion.

4.3 Results and discussion

A drill string fatigue failure prognosis technique makes an important contribution in risk reduction in oil drilling because there is a considerable probability of fatigue failure and high scale consequences are involved. Although there are numerical approaches such as FEM which can be implemented to perform this task, it requires a high computational power which makes the process slower. The proposed hybrid technique provides a solution for this issue by sharing the tasks among the two techniques, namely BG and finite element models. The task sharing was done based on their respective strengths hence the overall process becomes efficient. The remaining

fatigue life of the critical point (maximum stress concentrated point) shown in Figure 4.13 was evaluated using both finite element model and theoretical calculations. The finite element model result was 26.3 hours while the theoretical result was 21.6 hours. Here, Figure 4.13a illustrates the stress distribution in the threaded connection when the repeating unit finite element model is cantilevered and loaded with a 1 N force at the free end. Figure 4.13b represents the remaining fatigue life distribution over the threaded connection. The highest stress concentrated area has the lowest remaining fatigue life as expected.

4.3.1 Main challenges

One of the main challenges in developing the bond graph was the unavailability of published data and the experimental setups to validate the BG model. As mentioned under methodology, as a way around, the model was subjected to two virtual tests to improve confidence. Firstly, the natural frequency was determined through the frequency domain toolbox in 20 sim™. There, under model linearization, the effort on one axial compliance element was set as the input and the state of another element close to the midpoint of the beam was tested. The first, second, and third natural frequencies were compared with the theoretical values using Equation 4.4 [15]. As shown in Table 4.2, theoretical and simulation results were in good agreement for the first natural frequency. This improves the confidence in the dynamic behaviour of the drill string model.

$$\omega_n = \frac{n\pi c}{l}; \qquad n = 1, 2, 3, ... \tag{4.4}$$

Secondly, the beam bond graph model was subjected to a three-point bending test

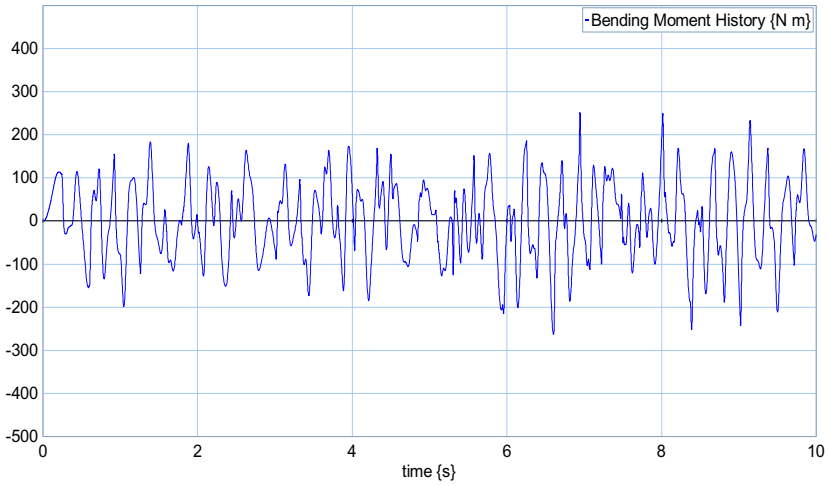

Figure 4.11: Bending moment fluctuation history determined through BG model

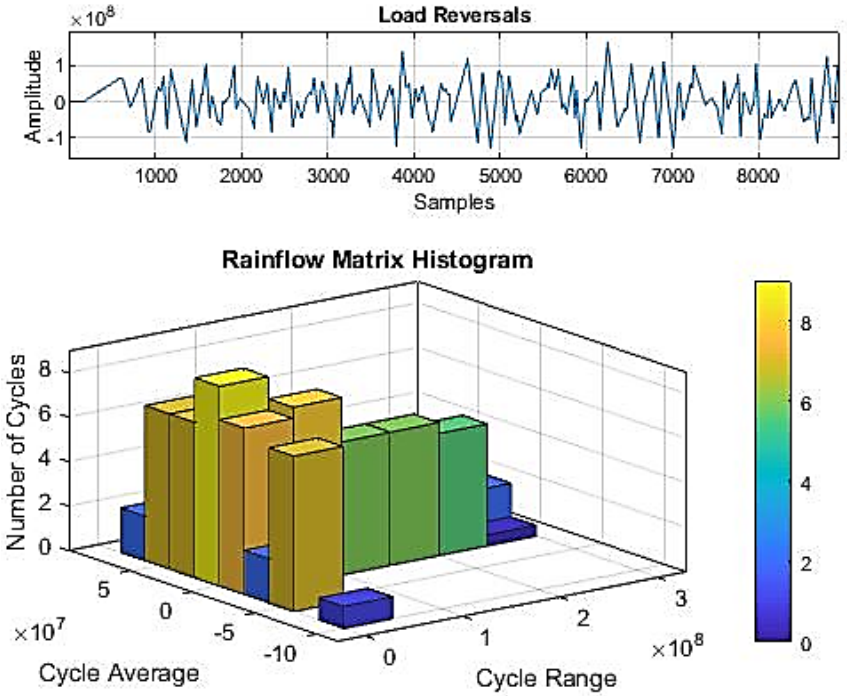

Figure 4.12: Rain flow counting result for a sample time of 10s

Table 4.2: First three natural frequencies of the drill string

n	ω_n **Theoretical** (Hz)	ω_n **Simulation** (Hz)	**Percentage deviation**
1	170	169	0.6 %
2	340	289	15.0 %
3	510	404	20.8 %

and the lateral deflection at the mid-span was compared with the theoretical value. Equation 4.5 was used for the analytical calculations. In Equation 4.5, P is the applied load at the midspan; L is the length of the beam; E is the elastic modulus of the material; and I is the second moment of area of the cross-section. The simulation results showed less than 1% deviation from the theoretical value helping to improve the confidence on the static behaviour of the BG model.

$$\delta_{max} = \frac{PL^3}{48EI} \tag{4.5}$$

The experimental validation of the finite element model is quite challenging as the area of interest is the threaded connection. Therefore, the use of strain gauges is not practical. As mentioned in [10], in a threaded connection, the first three threads take 75% of the total axial load. This was clearly evident by observing the fatigue damage in the first three threads in a separate finite element model which is axially loaded. This is a good indication of the accuracy of the model. Further, the mesh was refined to give a steady set of solutions, improving confidence in the accuracy.

4.3.2 Limitations and potential applications of the BG model

The bond graph model is designed to capture the bending, axial and shear deformations only. It needs to be further developed to simulate the torsional deformations of the drill string. According to [5], this is an essential feature for a drill string simulation and will be addressed in future studies. Further, the frictional effects should be

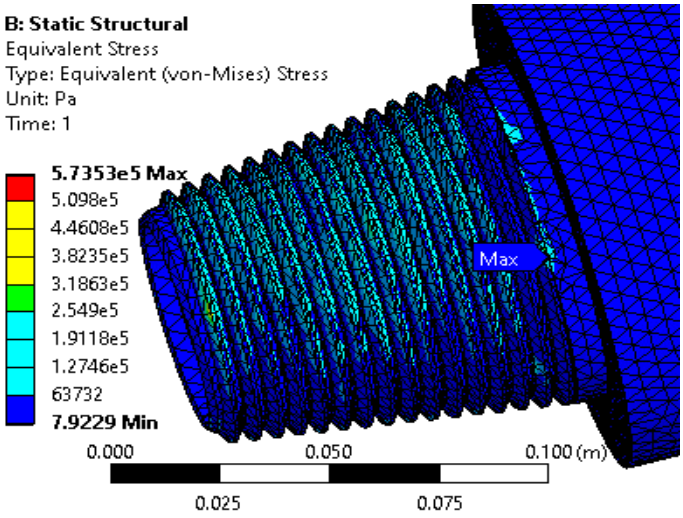

(a)

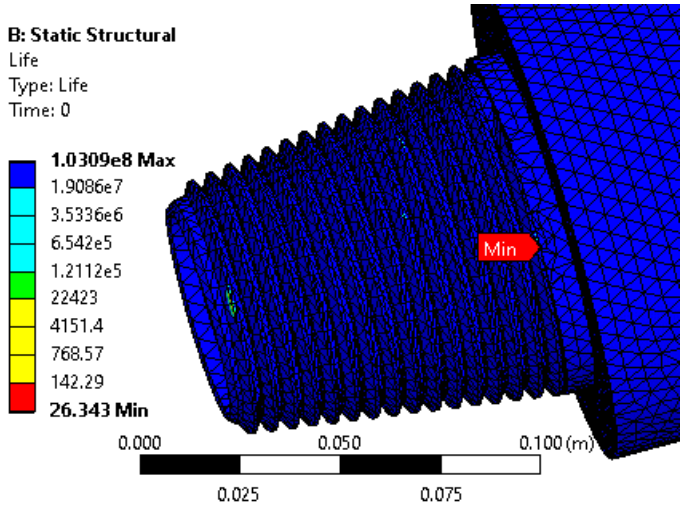

(b)

Figure 4.13: Critical point of the threaded connection

incorporated to get a deep insight of the behaviour of the drill string while in operation. A proper friction model can be incorporated to achieve this. In addition to that, a suitable bit-rock interaction model is to be introduced to simulate the interaction between the drill bit with the rock being drilled. This BG model can be adopted to predict the dynamic behaviour due to lateral and axial vibrations. Nevertheless, it is not recommended to use it when the torsional vibration induced vibrations, such as stick-slip, are dominant. Further, the BG model can be adopted in different applications which can be approximated to 2D plane deformation of beams such as leaf springs of vehicles.

4.3.3 Potential improvements in fatigue calculation technique

Fatigue calculation was initially done with Ansys® Fatigue Tool and then compared with the theoretical calculation for a simplified variable amplitude proportional loading case. There are a number of limitations involved with the methods used which can be further improved. The drill string is subjected to a combination of bending, axial, and torsion stresses. As the BG used in the current study is two dimensional, the torsion is not considered because the main focus in this study is to develop the overall methodology. Here, the point of interest is a threaded connection closer to the center (i.e. the 15^{th} BG element) of the drill string. It can be seen in the BG that the drill string is in tension towards the top while the lower part is in compression as expected. The element 15 is in tension of 100 N, which creates normal stress of 22 Pa. Therefore, in comparison with the bending stress, this normal stress can be neglected. With this simplification, the problem can be approximated to a proportional, variable amplitude scenario, which can be handled with Ansys® Fatigue Tool. This allows comparing the two results from the theoretical calculation using Matlab® code and

the Ansys® Fatigue Tool.

As a further development, the theoretical calculation can be generalized as follows to apply in combined loading applications. The bending moment, axial force and torsional fluctuation matrices of a given element can be extracted from the 20 sim™ simulation. Then it can be normalized and multiplied by the maximum direct and shear stresses determined by the finite element model static analysis. Here it is assumed that the stress fluctuation is linearly related to the fluctuation of each load when their individual effect is considered. Knowing the direct and shear stresses in each direction, the bending induced 'signed von Mises stress' fluctuation matrix can be calculated. Then the 'rainflow' function in the Matlab® signal processing toolbox can be used to perform the rain flow counting to determine the equivalent range (σ'_a) and equivalent mean (σ'_m). Finally, the Palgram-Miner rule can be implemented to determine the damage percentage and the remaining lifetime (prognosis) of the drill string.

4.4 Conclusion

A multibody dynamic bond graph model of a drill string and a finite element model were employed to estimate the remaining cumulative fatigue life of a drill string. finite element model was incorporated to refine the BG model compliance values in order to increase the accuracy of the BG model. The updated BG model was used to extract the dynamics of the drill string. The dynamic response of the drill string was then converted to stress fluctuations and used in fatigue analysis using both analytical and finite element models. The remaining useful life was prognosticated as 26.3 hours by the FEM fatigue tool. In general, the proposed bond graph-finite element model hybrid approach can be effectively used in fatigue failure prognosis of drill strings

while FEA can be effectively used to parameterize the BG simulations to increase precision.

4.5 Further work

The BG model developed in this study is a 2D model hence only two of the six main bottom hole assembly (BHA) dynamic motions can be simulated. Simulation of the rest of the types of motions including forward and backward whirl, and torsion can be achieved by developing a 3D BG model. The procedure followed and proposed for the combined loading in the current study can be used in determining the remaining fatigue life. Further to that, the model is to be experimentally validated. As an alternative, a finite element transient model of a complete drill string can be developed and compared with the performance of the hybrid model proposed in the current study. On the other hand, the fatigue analysis can be broadened to analyze the fatigue damage due to a multiaxial, non-proportional, and variable amplitude loading condition to make it more accurate in fatigue failure prognosis.

References

[1] T. Hill, P. Seshadri, and K. Durham, "A unified approach to drillstem-failure prevention," *SPE drilling engineering*, vol. 7, no. 04, pp. 254–260, 1992.

[2] K. Macdonald and J. Bjune, "Failure analysis of drillstrings," *Engineering Failure Analysis*, vol. 14, no. 8, pp. 1641–1666, 2007.

[3] M. Joosten, R. Ferguson, and J. Shute, "New study shows how to predict accumulated drill pipe fatigue," *World Oil;(United States)*, vol. 201, no. 5, 1985.

[4] S. M. Zamani, S. A. Hassanzadeh-Tabrizi, and H. Sharifi, "Failure analysis of drill pipe: A review," *Engineering Failure Analysis*, vol. 59, pp. 605–623, 2016.

[5] D. G. Rideout, A. Ghasemloonia, F. Arvani, and S. D. Butt, "An intuitive and efficient approach to integrated modelling and control of three-dimensional vibration in long shafts," *International Journal of Simulation and Process Modelling*, vol. 10, no. 2, pp. 163–178, 2015.

[6] W.-C. Chen, "Drillstring fatigue performance," *SPE drilling engineering*, vol. 5, no. 02, pp. 129–134, 1990.

[7] G. Grondin and G. Kulak, "Fatigue testing of drillpipe," *SPE Drilling & Completion*, vol. 9, no. 02, pp. 95–102, 1994.

[8] M. Knight and F. Brennan, "Fatigue life improvement of drill collars through control of bore eccentricity," *Engineering Failure Analysis*, vol. 6, no. 5, pp. 301–319, 1999.

[9] R. Browell and A. Hancq, "Calculating and displaying fatigue results," *Ansys Inc*, vol. 2, 2006.

[10] R. G. Budynas, J. K. Nisbett, *et al.*, *Shigley's mechanical engineering design*, vol. 9. McGraw-Hill New York, 2011.

[11] B. A, D. K, K. H, K. W, M. B, and J. Petersen, "Multiaxial rainflow: A consequent continuation of professor tatsuo endo's work," in *The rainflow method in fatigue*, pp. 31–40, Elsevier, 1992.

[12] HongxinCreaton, "HongxinCreaton-OCTG,Drill rig," 2021.

[13] D. C. Karnopp, D. L. Margolis, and R. C. Rosenberg, *System dynamics: modeling, simulation, and control of mechatronic systems*. John Wiley & Sons, 2012.

[14] M. H. Jalali and G. Rideout, "Development and validation of a numerical model for vibration of power lines," 2018.

[15] S. R. Singiresu *et al.*, *Mechanical vibrations*. Addison Wesley Boston, MA, 1995.

Chapter 5

Fatigue Life Prognosis of an Oil Well Drill String Using Cascaded Dynamic Models

Abstract

Early estimation of the fatigue life of an oil well drill string reduces the risk associated with drill string fatigue failures. In this study, a low-order computationally efficient bond graph model of a vertical well drill string and a component-level higher-order finite element model of a drill pipe threaded connection are employed to predict the fatigue damage of a given drill pipe. The bond graph is a 3D lumped segment model developed using the Newton-Euler formulation and body fixed coordinates. It is parameterized using finite element modelling simulations. The stress history from the top-level model is applied to the component-level model that contains details such as threaded geometry. Then, a multi-axial, non-proportional, and variable amplitude (MNV) fatigue estimation is performed using an open-source finite element analysis code. The fatigue prognosis approach is then demonstrated in a drill string design case study that optimizes the placement of vibration stabilizers in the wellbore to avoid severe vibrations while minimizing fatigue damage. Optimal placement of stabilizers predicts a 200% increase in fatigue life of the most vulnerable component with

reference to the worst-case scenario.

Key Words: *Bond graph, Cumulative fatigue, Stabilizers, Finite Element Method*

Co-authorship Statement

This chapter is a manuscript of a full paper that is submitted to Journal of Engineering Failure Analysis. The co-authorship statement for this chapter follows:

The declaration applies to the following article
M. Galagedarage Don and Rideout, G., *Fatigue Life Prognosis of an Oil Well Drill String Using Cascaded Dynamic Models*. Engineering Failure Analysis, Elsevier **Article status: Published** The PhD student analyzed the literature, performed the experiments, collected the data, developed the codes and prepared the manuscript. The supervisor edited, helped organize the manuscript, and contributed to the choice of case studies.

5.1 Introduction

Drill string failures can occur due to several reasons, such as excessive vibrations and load fluctuations, overloading, and elevated temperatures [1]. Vibrations and cyclic loading cause fatigue failure, while overloading causes failures such as buckling, twist-offs, parting, collapse and burst [2]. Excessive heat can be generated due to the severe abrasion of the drill pipe with the well bore. This happens when trying to release a stuck pipe or at severe doglegs. The elevated temperature can go beyond the critical temperature, and an applied load can destroy the pipe. Also, sudden cooling can take place due to the circulation of the drilling fluid and hence the pipe can become brittle and less resistant to shock loads [1].

As illustrated in Figure 5.1, this study mainly focuses on the failure of drill strings due to fatigue which is the most prevalent type of drill string failure [3]. There are

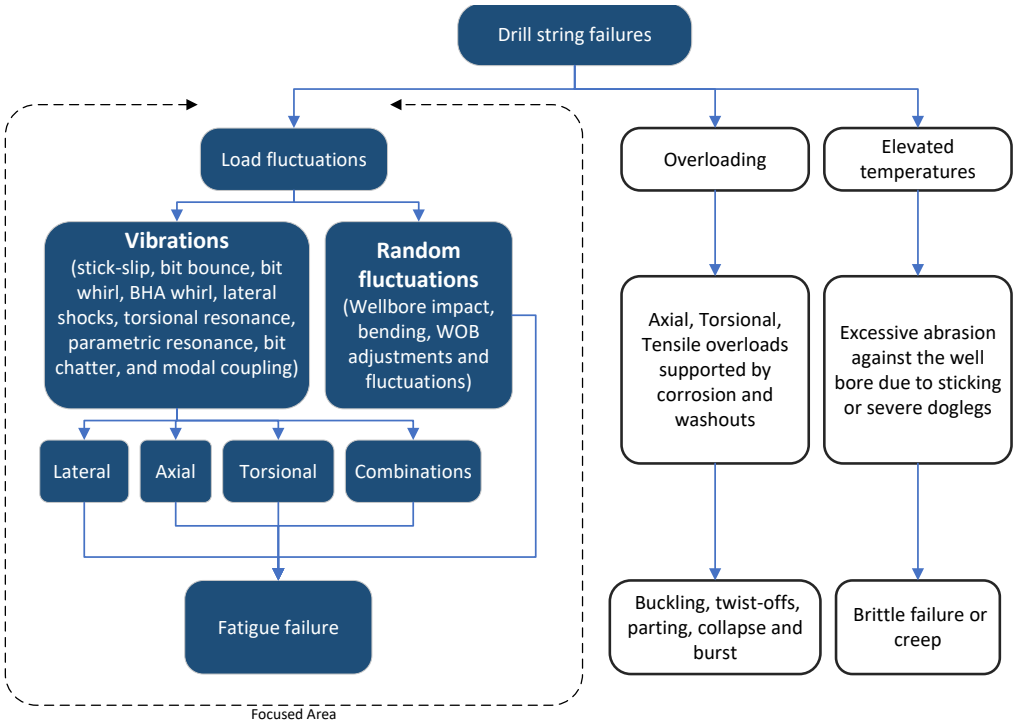

Figure 5.1: Scope of drillstring failures considered in this paper

three different forms of fatigue failure: pure fatigue failure, fatigue scars, and corrosion fatigue damage [3]. Pure fatigue failure is the area of interest in the current study. Drill string vibration can take the form of stick-slip, bit bounce, bit whirl, bottom hole assembly whirl, lateral shocks, torsional resonance, parametric resonance, bit chatter, and modal coupling. They can be broadly categorized as lateral vibrations, axial vibrations, and torsional vibrations. These vibrations can damage not only drill pipes and collars but also the drill bit and the bottom hole assembly [4]. Drill pipes fail due to fatigue, mainly at the threaded connection, due to high stress concentrations and their fluctuations [5–8]. Therefore, the main focus of the study is directed toward fatigue failures that occur at the threaded connections of the drill pipes caused due to the lateral, axial, and torsional vibrations and their combinations. However, the proposed approach can be applied to any type of fatigue threat, as long as a detailed

model in the vicinity of the at-risk component can be generated.

Even though the probability of failure can be maintained at a lower rate, the consequences of a failure are immense, leading to substantial financial and other risks. In the study presented in [9], the cost of a drill string failure due to a washout scenario is estimated as $\$300,000$ for a typical land rig. The estimated cost is based on spread rates and fishing equipment costs. In addition to that, nonproductive time, fishing services, cement plugs, sidetracks, bottom hole assembly lost in hole, and tool replacements cost the operator millions of dollars to recover [10]. Therefore, a potential drill string failure by any means carries a very high financial risk to the entire project.

The method in this paper also addresses efficiency issues in simulating top-level drill string models. Techniques such as the finite element method (FEM) come with higher computational burden in simulating long-duration drillstring vibrations with external contacts. An efficient alternative is bond graph implementation of a lumped segment representation of the drill string. The bond graph approach allows fast computation of the global drillstring dynamic responses, even with complex non-linear forcing functions over long time windows. The responses from such a "top-level" model can then be used as inputs to a high-order finite element model of individual components. The top-level model efficiency can be improved by using averaged cross-sectional properties, neglecting features such as pipe threads, etc. The finite element model can incorporate these complex features over a short sample of the drillstring, to 1) generate the averaged properties used in the top-level model, and 2) perform component fatigue life estimation that considers the complex geometric stress concentrations and component interactions in the threaded connections. The proposed methodology can also be applied to systems such as stepped shafts supported by multiple bearings or, indeed, any vibrating system where design decisions can affect

the fatigue life of individual, geometrically complex components.

Section 5.2 reviews the literature on fatigue life prognosis frameworks, drillstring vibration modelling and mitigation. Section 5.3 overviews the methodology followed by Section 5.4 with more specific details on a case study. Section 5.5 provides results, and discussion and conclusions are in Sections 5.6 and 5.7.

5.2 Background and literature review

5.2.1 Fatigue life prognosis frameworks for vibrating structures

Fatigue life prognosis provides crucial information to increase the drill string's reliability and dependability. This section highlights the available fatigue life prognosis frameworks for vibrating structures and their applicability to the current investigation.

A framework for monitoring the structural integrity of airplanes by assessing the dynamic behaviour of crucial components is presented by [11] to optimize the scheduling of an aircraft maintenance program. The mission load spectrum and structural response were evaluated concurrently using a combination of accelerometers and strain gauges, allowing the derivation of specific transference functions for each monitored key component. The components were continuously monitored, and the fatigue damage was calculated to evaluate the operation limit. For analysis, the structural health monitoring platform PRODDIATM™ Aero was utilized, which employs time and frequency-based fatigue models to estimate the structural health of aircraft. Communication limitations between sensors and the analytical platform inhibit the implementation of similar technology in drill string fatigue life prognosis.

A multi-scale, non-deterministic Digital Twin framework was developed and validated for forecasting fatigue crack propagation from initiation to failure by [12]. A complicated metallic test specimen was exposed to uniaxial fatigue, and the grain boundary level fracture propagations were modelled using finite element analysis. Fatigue life prediction showed an absolute error of 9.5% relative to the physical sample. A finite element analysis and data-driven regression combined approach is presented by [13] to predict the fatigue crack propagation due to in-phase biaxial loading. The model consisted of online and offline components where the online component predicted the crack propagation under constant loading while the offline component used experimental data to assist the online model. The study was limited to bi-axial loading conditions.

A generic approach for integrating in-situ diagnostics and prognostics in a non-deterministic Digital Twin architecture is presented in [14]. This work used high-fidelity finite element modelling, Markov chain Monte Carlo sampling, and periodic measurements from strain sensors placed at nine distinct locations on a sample surface to simulate the formation of non-planar cracks. This approach showed successful prognostic capabilities for a laboratory setup and has the potential to be further developed toward realistic in-situ applications. However, this method will only be effective if regular and accurate stress measurements are feasible, which is not true for drill string-related applications.

In addition to the frameworks mentioned above, numerous fatigue life prognosis approaches are reported in the literature. A two-stage model is proposed by [13] to determine fatigue life of steel structures using a local strain-life approach and linear elastic fracture mechanics. Additionally, [15] makes use of cutting-edge stochastic modelling in conjunction with structural health monitoring data produced from strain measurements to forecast the fatigue life online in composite materials that are

subjected to fluctuating loads. In windmill structural fatigue estimation, the study presented in [16] employed spectral approaches for determining structural responses to stochastic loading and demonstrated that accurate approximations of the rain-flow stress-range spectra are attainable based on the power spectral densities of the structural responses.

A vast majority of engineering structures are subjected to multi-axial loading, and hence it is essential to have an insight into the material's response to such loading conditions. A multi-axial, non-proportional, and variable amplitude (MNV) fatigue analysis is essential in designing safe and reliable structures and optimising their weight and cost [17, 18]. Multi-axial fatigue estimation can also be used to evaluate the performance of existing structures and components, identify potential failure modes, and develop effective maintenance and repair strategies. Although there are fatigue life estimation frameworks available in the literature, as presented in this section, there is a requirement for a more generalized framework for MNV loading conditions to address structural fatigue failure-related problems.

5.2.1.1 Available tools and techniques for fatigue life estimation

While there are numerous open research topics in the area of fatigue life assessment of engineering components, as mentioned in [19] and [20], stress-life, strain-life, and fracture mechanics are the three basic techniques used in fatigue analysis. According to [21], if an environment is corrosive, infinite fatigue life is not possible at which the material will no longer experience fatigue because corrosion will ultimately lead to failure, regardless of cyclic stress level. The harm caused by the combination of corrosion and cyclic stress is greater than the sum of the damage caused by each separately. Even in settings that seem to have little or no corrosion, the fatigue threshold or endurance limit will always be lower when exposed to a corrosive environment.

Although excessive corrosion can be avoided through techniques such as the use of corrosion inhibitors [22], reducing the water content by using emulsion-based drilling fluid [23], and monitoring pH levels; corrosion cannot be nullified. Therefore, as explained in [21], corrosion lowers the fatigue endurance limit, and fatigue failure is accelerated by washouts, surface damages, and induced thermal stresses.

As further explained in [19], high cycle fatigue, which encompasses more than 10^5 cycles, is best treated with a stress-life method based on empirical S-N curves, which are then altered by several correction factors. The method is suitable for determining the overall fatigue life of an engineering component, despite the fact that the crack start and propagation are not individually detected. On the other hand, the strain-life method uses the strain, which can be readily measured using strain gauges, as a highly effective criterion for describing low-cycle fatigue. Instead of S-N curves, strain-life relation equations are used that consider the critical plane of facture and crack initiation. In the fracture mechanics approach, it is assumed that flaws of a certain maximum size might reside inside or on the surface of the material. The maximum flaw size can be determined using a non-destructive testing (NDT) technique. At the same time, this flaw propagates based on the stress fluctuations the material is subjected to. The fact that the user can decide when inspections should be performed and when maintenance should be scheduled is one of the strengths of the fracture mechanics approach.

Both commercial and open-source software are available, which employ the above techniques to determine the fatigue life of structures [19, 20, 24]. ANSYS® Fatigue Tool facilitates stress life and strain life approaches while nCode Design Life® and SalomeMeca™can apply all three methods. SalomeMeca™ is an open-source finite element analysis code with a solver called CodeAster™, with a capability to handle MNV loading conditions [25]. The software accepts multiaxial, non-proportional load

fluctuations, which can simulate the most general scenarios of fatigue damage. On the other hand, software packages such as Matlab® are also equipped with tools to perform 'rainflow counting' of variable amplitude stress fluctuations, which is an important step in fatigue life prognosis.

Drill string fatigue failure applications fall in the category of high-cycle fatigue. Therefore, the stress-life approach is used in this paper, implemented using SalomeMeca™, an established freely available research tool with MNV fatigue estimation capability.

5.2.2 Modelling of drill-string dynamics

5.2.2.1 Fluid conveying pipe vibration modelling and simulation

Dynamics of fluid-carrying pipes were first analytically modelled with linear equations of motion in the 1950s by [26–28]. These models have been developed considering the effect of the fluid flow, assuming a uniform flow profile in the pipe. Furthermore, [29–34] have further analyzed the dynamic behaviour of fluid-conveying straight pipes and require further development to make them applicable in analyzing pipes with nonlinear trajectories. Moreover, the effects on pipe dynamics due to the momentum and rheological changes of the flowing fluids are yet to be incorporated into these analytical models.

Finite element method-based numerical models suffer from the requirement of an excessive amount of computation power in order to simulate complex multi-physics models of fluid conveying pipes [35]. Nevertheless, several models have been developed using the finite element method, such as in [36–39].

A computationally less expensive approach using three-dimensional lumped segments, with Newton-Euler equations of motion implemented in the bond graph for-

malism, was proposed by [35] to simulate long slender structures. This approach is capable of realistically simulating 3D drill string vibrations and interactions with the well bore. Also, the simulation can be easily coupled with actuators such as PID-controlled induction motors, while the boundary conditions can be easily reconfigured. Moreover, lumped segment models can also incorporate the damping effects due to the rheological and dynamic behaviour of fluids flowing through the pipe and the outer annular space. Based on the modelling approach developed by [35], a complete deviated well drill string simulation has been presented by [40]. This model can simulate the drill string vibrations due to the axial and torsional bit-rock interactions and can be used to optimize the drilling performance.

The model introduced by [35] and further developed by [40] has been chosen for the current study. It has comparatively less computational burden compared to finite element analysis, and the flexibility to incorporate contact models and fluid effects. Bond graphs facilitate the combination of submodels from different domains such as fluid, multi-body dynamics, and electromechanical actuation.

5.2.2.2 The bond graph formalism

The bond graph simulation environment provides a common platform for the simulation of systems comprised of elements from multiple engineering domains. The method does not use discipline-specific elements, but generalized elements for energy storage (capacitive C and inertial I), dissipation R, transformers TF, gyrators GY, and power conserving junctions to enforce parallel and series connection laws. Energy plays the role of 'common currency' [41] hence the mechanical, electrical, thermal, and hydraulic systems can be unified by the fact that their components exchange energy [42] through 'Energy Ports'. The system interacts with its surroundings using sources of effort Se and flow Sf ports. In other words, bond graph modelling lever-

ages analogies among different domains to solve technological problems [43]. There are two generalized power variables, $effort(e)$ and $flow(f)$ which are the time derivatives of generalized $momentum(p)$ and $displacement(q)$. The product of $effort(e)$ and $flow(f)$ is power.

Further, the power conserving $0-junction$ and $1-junction$ model Kirchoff's node and loop laws, respectively. Efforts at $0-junctions$ sum to zero while flows are identical along all the bonds connected to the $1-junction$ and vice versa. The algebraically positive power flow direction is indicated with a half arrow while causality is indicated with a short line perpendicular to the bond. The causal stroke location indicates whether the effort or flow is the input or output from the constitutive law of the connected element. Powerless signals such as control signals are denoted by a full arrow. A systematic approach to learning bond graph concepts is presented in [42].

5.2.3 Drill-string vibration mitigation

In order to have a higher rate of penetration while maintaining a suitable failure safety factor in the drilling process, the operator must predict and suppress vibrations [44]. Therefore, it is essential to identify the main causes of drill string vibration and how to mitigate them.

Lateral drill string vibration is known to lead to fatigue failures and measurement while drilling (MWD) tool failures. While the bit can cause significant vibration, the centrifugal forces produced when imbalanced drill string components are rotated are also significant [45, 46]. As described in [47], bore misalignment, initial curvature, and gradual wear throughout service are some of the factors that contribute to imbalance. Furthermore, stabilizer blades, mud motors and the friction between the borehole and

drill string are contributing factors [48].

Certain field-developed vibration mitigation procedures are available in drilling manuals have been validated through modelling and studying the drill string dynamics [49]. For example, stopping and restarting can be done upon detection of severe vibration, and stability paths can be found and followed to avoid critical vibrations when increasing the rotary speed of the drill string.

Drill string stabilizers are used to mechanically stabilize the bottom hole assembly. Conventionally, changes in the bottom hole assembly are made by tripping the drill string out of the wellbore. This is to add or remove stabilizers to or from the drill string. As a solution, [50] proposes a stabilizer which can be remotely adjusted into two distinct diameters, and each mode is controlled by switching on and off the drilling mud pump.

Varying WOB and drilling speed are also approaches to mitigate the vibration. Sometimes such actions can reduce one type of vibration while exacerbating another, suggesting a need for a multi-variable multi-objective optimization approach to vibration and component life prediction. This paper focuses on a single vibration mitigation design variable, the placement of stabilizers, using 'cascaded' models to efficiently predict stress history and fatigue life of components. The methodology is described in Sections 5.3 and 5.4. The overall approach is not restricted to a single variable optimization, and the competing objectives of multiple vibration mitigation methods could be studied by expanding the optimization problem definition. The primary contribution of this paper is to demonstrate the use of a top-level simplified model feeding stress history into, and receiving parameter updating information from, a higher-order component-level model, and then performing MNV fatigue analysis.

5.3 Methodology

This section presents the methodology followed to develop the fatigue life prognosis framework. A 3D drillstring bond graph simulation is employed and parameterized to meet the specifications of API 5D drill pipes and collars. A fatigue life estimation is presented based on the stress history extracted from the 3D drill string bond graph simulation. Finally, the methodology is applied in a case study to demonstrate the ability of the framework to be used as a fatigue life optimization tool.

5.3.1 Development of the drill-string dynamic model

The lumped segment 3D bond graph dynamic model consists of pipe, stabilizer, and drill collar elements. The model was developed based on the contributions in [35] and [51]. Pipe and collar elements are illustrated in Figure 5.2 and 5.4 respectively. Only the axial compliances are shown in the figures for clarity. A and B are the two ends of an element, while G is the centre of gravity. A detailed schematic of an API 5D drill pipe is shown in Figure 5.3. A drill pipe element of a drill string bond graph model was defined as two connected drill pipe halves, as illustrated in

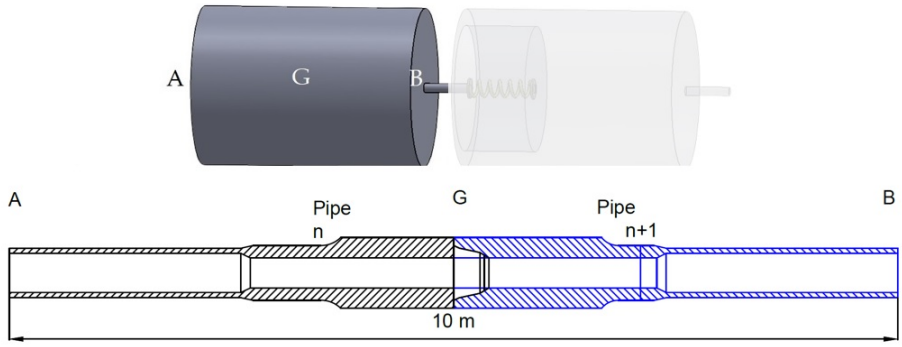

Figure 5.2: The conceptual illustration of a bond graph pipe element (not to scale)

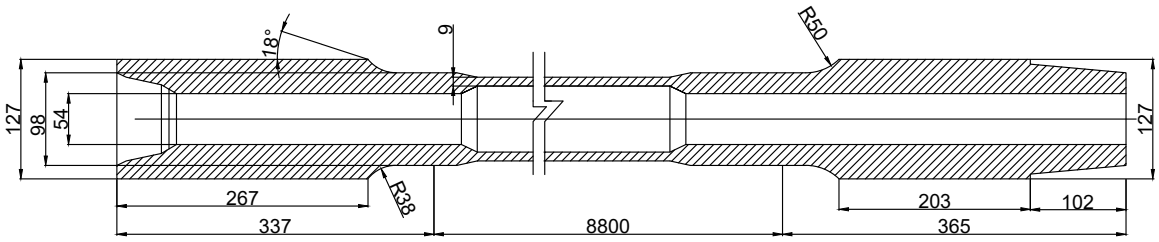

Figure 5.3: Schematic diagram of the API 5D drill pipe (not to scale)

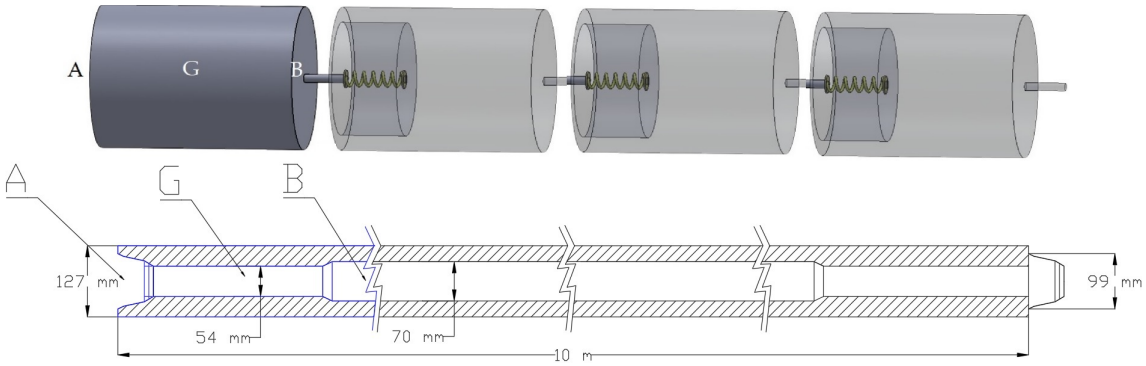

Figure 5.4: The conceptual illustration of a bond graph collar element (not to scale)

Figure 5.2. They are API 5D standard drill pipes made from E75 Carbon Steel with an 'internal and external upset' end finish. In the original parameterization of the bond graph model, the compliance values (reciprocal of stiffnesses) of each element have been calculated without considering the varying cross-section and the effect of threaded connections. Therefore, a finite element method-based approach is used to determine the unknown compliance parameters of a given element more accurately. A detailed description on the determination of compliance values; bending, axial, shear, and torsional; is presented in Section 5.3.1.1.

The drill string vibrations get damped due to the presence of the drilling fluid. This effect is often simplified and modelled as a static damping constant. In this study, the damping model introduced in [52] is implemented to simulate the varying damping constant based on various variables such as the eccentricity of the drill pipe

in the wellbore, fluid rheology, and flow speed.

5.3.1.1 Determination of the compliance values of elements

The four primary compliance values: axial, shear, bending, and torsional; are difficult to establish precisely through manual calculations due to the intricate curvatures and varied cross-sections. Further, the effect of the threaded connections on the stiffness values is difficult to estimate efficiently using manual calculations. Figure 5.5 conceptually illustrates the first three compliances, while the torsional spring can be visualized as a similar spring to the axial but with a rotational instead of translational degree of freedom.

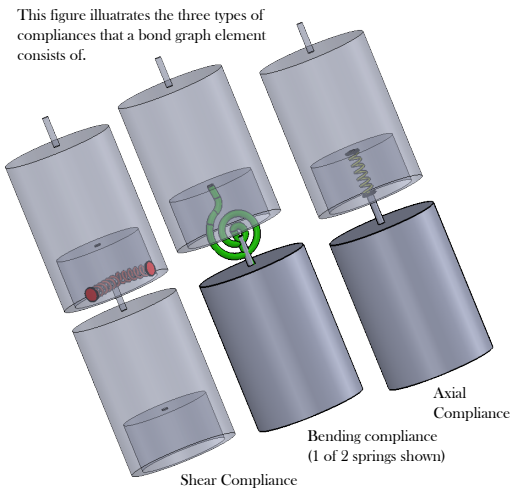

Figure 5.5: Schematic of pipe lumped-parameter elements

In this section, the procedure followed to determine the compliance values of drill pipe, stabilizer, and collar elements is presented.

The selected element was modelled in SolidWorks® and imported into ANSYS® Static Structural. After performing a mesh dependence test, the minimum size of the element was selected to be 1×10^{-2} m, taking into account the processing speed and convergence of the results. The drill collar element was cantilevered and subjected to

bending, axial, shear, and torsional deformations to examine the respective responses as illustrated in Figure 5.6.

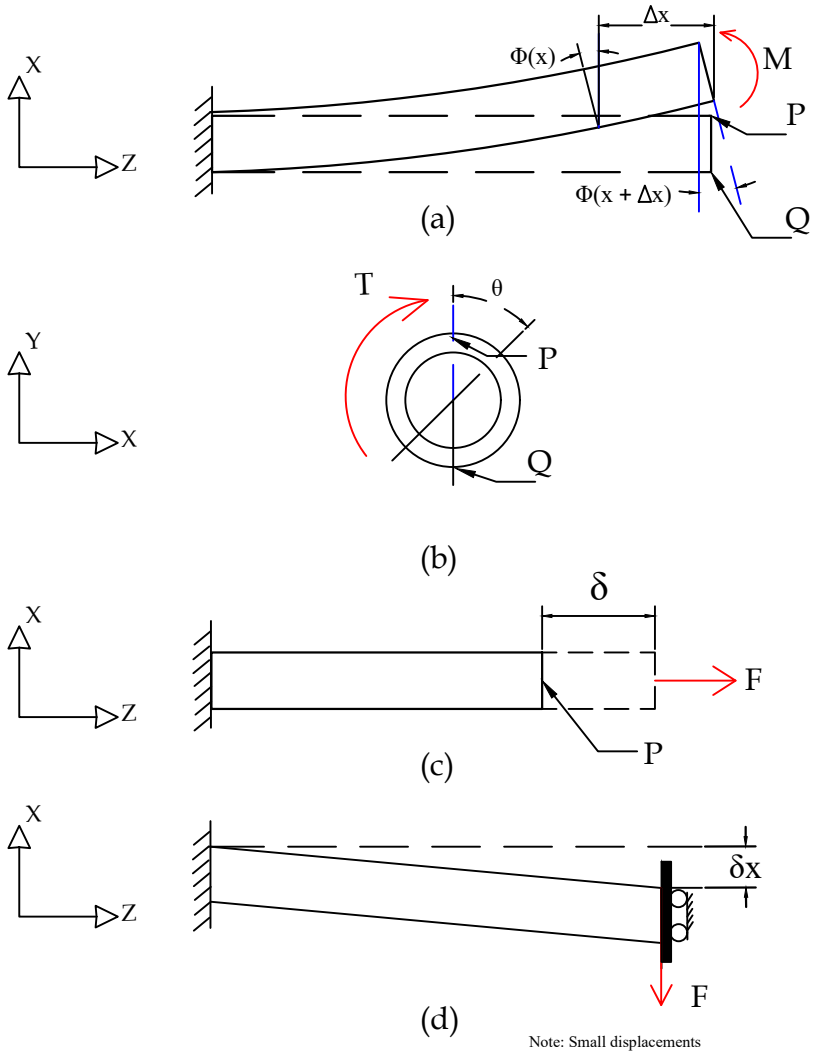

Figure 5.6: Determination of compliance values

To determine the bending compliance, the cantilevered element was given a 1000 Nm bending moment (M) at the free end as shown in Figure 5.6 a. This results in a rotation of the free end on the $x - z$ plane. The displacements of points P and Q

were precisely drafted in AutoCAD® and the angle of rotation was determined as $1.12675 \times 10^{-3}\ rad$. According to [42], if the rotations of two cross-sections are $\phi(x)$ and $\phi(x + \Delta x)$, the relationship between the applied bending moment (M) and the difference of the two plane rotations is given by Equation 5.1.

$$M = \frac{EI}{\Delta x}[\phi(x + \Delta x) - \phi(x)] \tag{5.1}$$

where L, E, and I are length of the beam segment, elastic modulus, and second moment of area of the cross-section respectively. The bending compliance (C_{bend}) was calculated as shown in Equation 5.2.

$$C_{bend} = \frac{L}{EI} = \frac{\phi(x + \Delta x) - \phi(x)}{M} = 1.12455 \times 10^{-6}\ rad/Nm \tag{5.2}$$

To determine the torsional compliance, a moment of 1000 Nm was applied on the free end in the z direction, as illustrated in Figure 5.6 b. Then the displacements of the points P and Q were determined using the finite element model and precision mapping to determine the angle of twist of the beam due to the applied moment. Equation 5.3 defines the torsional compliance ($C_{torsional}$).

$$C_{torsional} = \frac{L}{GJ} = \frac{\Theta}{T} \tag{5.3}$$

where L is the length of the beam, G is the shear modulus, J is the second polar moment of area, Θ is the angle of twist, and T is the applied torque.

Equation 5.4 describes the axial compliance C_{axial} which originated from Hooke's Law of elasticity.

$$C_{axial} = \frac{L}{EA} = \frac{\delta}{F} \tag{5.4}$$

where E is the elastic modulus, A is the cross-sectional area, δ is the extension and F is the applied force. As illustrated in Figure 5.6 c, an axial load of 1000 N was applied and the displacement response of point P was measured in the axial (z) direction and C_{axial} was calculated using Equation 5.4.

To estimate the shear compliance (C_{shear}), as shown in Figure 5.6 d, the element was cantilevered and a tangential distributed force of 1000 N was applied on the free end surface. The motion of the loaded plane was restricted to rotate in order to minimize the effect of bending due to the applied load. The calculation was done using Equation 5.6 which was derived from Equation 5.5.

$$\tau = G\gamma \tag{5.5}$$

$$C_{shear} = \frac{h}{GA} = \frac{\delta x}{F} \tag{5.6}$$

where τ is the shear stress, G is the shear modulus, γ is the shear strain, h is the distance between the shear load and the fixed end, A is the cross-sectional area, F is the applied force and δx is the displacement of the loaded face in the direction of the applied shear force. All the displacements are in the $10 - 100$ μm range. Therefore, the small angle assumption was applied.

5.3.2 Fatigue life estimation approach

The load fluctuations on a real-world structure can be highly complex. Figure 5.7 illustrates six different loading conditions that a given point of a drill string can undergo while in operation. In the figure, F_s, F_a, M_b, and M_t stand for shear forces, axial force, bending moments, and torsional load respectively. The MNV fatigue estimation was performed using SalomeMeca™, an environment that is open-source

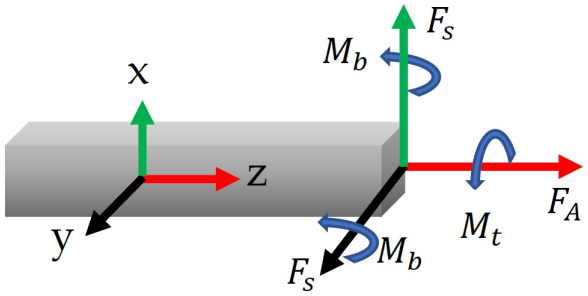

Figure 5.7: Complex loading acting on a structure

and therefore widely accessible.

The following section presents a detailed workflow for using SalomeMeca™ for the MNV fatigue analysis under consideration.

5.3.2.1 Accessing SalomeMeca™

There are several options available for accessing SalomeMeca™. A Linux-based operating system, CAE Linux™ 2020, is equipped with SalomeMeca™ along with many other Computer Aided Engineering (CAE) applications. Another option is installing the Ubuntu® operating system and manually installing the compatible SalomeMeca™ version. Moreover, the users can use the pre-processor, solver, and post-processor applications separately on these platforms. Alternatively, Windows versions are also available, which are stable and reliable. An overview of the simulation process is presented in Figure 5.8.

5.3.2.2 MNV fatigue analysis workflow

SalomeMeca™ consists of the pre-processors (Geometry Module, Shaper), solver (CodeAster™), and the post-processor (Paravis™) in a single package which provides all the required tools for an MNV fatigue analysis. Alternatively, a geometry designed in a different computer-aided design (CAD) package can be imported as a 'STEP' file

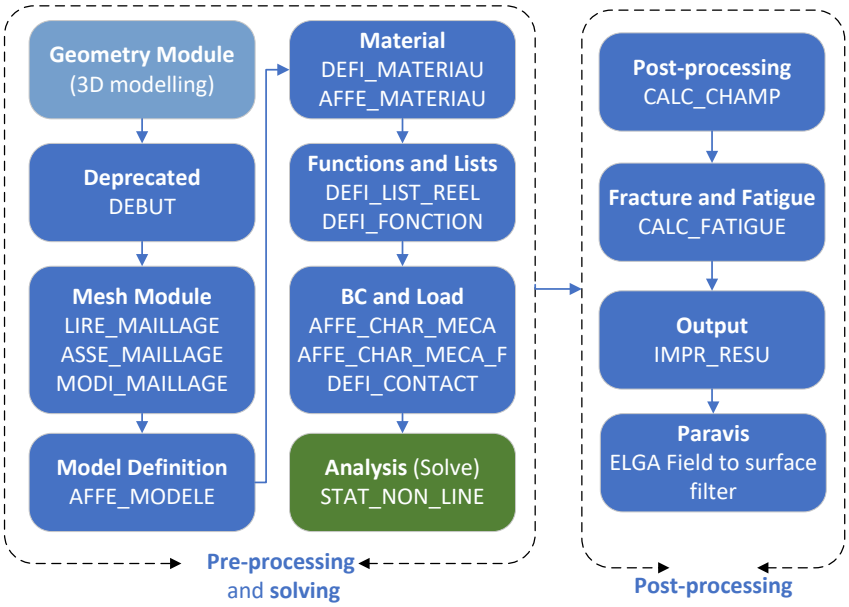

Figure 5.8: Fatigue life estimation workflow using SalomeMeca™

to start the pre-processing process (`File, Import`). Next, the groups of planes were defined, which will be later used to define the mesh planes (`New Entity, Group, Create Group`). These mesh planes were directly used in CodeAster™ to assign boundary conditions. For example, if a particular plane needs to be fixed while another plane is used in loading, it is necessary to create two separate planes and name them accordingly. Once this step is done, the Mesh Module was activated for further pre-processing in meshing.

Mesh Module provides greater flexibility to generate the optimum mesh for a given geometry. To create the mesh, start with `Create mesh` command and select the geometry. It is necessary to view the relevant geometry in order to select it. Depending on the geometry, 3D, 2D, 1D, or 0D can be selected, and the algorithm and *hypothesis* can be selected accordingly. For example, `NETGEN 1D-2D-3D` was selected as the algorithm for 3D geometries, and the *hypothesis* was selected as `NETGEN 3D Parameters`. By editing the *hypothesis*, the user can control the mesh parameters, in-

cluding the maximum and minimum sizes of elements. Then the mesh was computed using `Compute` command. Once the mesh is computed, the mesh groups were created using `Mesh, Create Groups from Geometry` command. The geometry groups created in the Geometry Module were used in this step to make it more convenient.

The current study consists of two separate 3D geometrical components, namely the Box and Pin of the threaded connection of two adjacent drill pipes. Two different approaches can be taken in developing the mesh for this kind of simulation. The first approach is generating a compound mesh at the meshing stage, and the second option is defining a nonlinear contact between the box and pin at the simulation setup stage. In the first approach, the two components can be separately meshed following the process mentioned above and generate a compound mesh using the `Mesh, Create Compound` command. The mesh planes defined in each component can also be made available in the compound mesh. The first approach will be described under AsterStudy in the next paragraph. The meshed geometries are presented in Figures 5.9a and 5.9b. Once the meshing step is completed, the `AsterStudy` module was activated to proceed with the simulation setup.

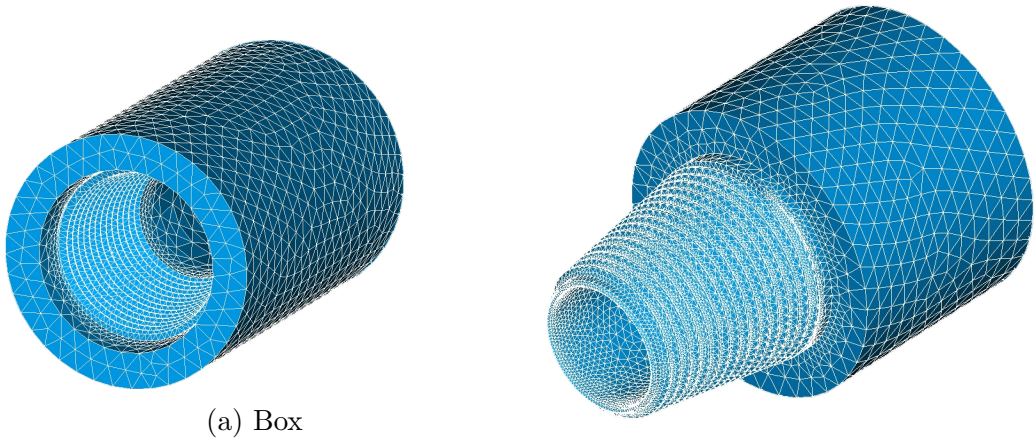

(a) Box

(b) Pin

Figure 5.9: The meshed 'box' and 'pin' components

AsterStudy provides the necessary tools to set up the simulation. The setup process consists of several sections and can be done directly by coding or using the graphical user interface (GUI). To start the process, a new stage was started under `CurrentCase` using the `Add stage` command. First, a mesh needs to be read, and it was done using `LIRE_MAILLAGE` operator in the `Mesh` category. Next, the mesh was modified using `MODI_MAILLAGE` operator. As the model is fixed at one face and loaded on the other face, `ORIE_PEAU_3D` is the suitable keyword to use, available under `MODI_MAILLAGE` operator. In this step, the mesh faces defined for the loading end and fixed end during meshing were selected to be available when setting boundary conditions and defining loads. The French words in the operator keywords reflect the country of origin of the software, the English-language documentation of which is limited.

Under `Model Definition` category, the operator `AFFE_MODELE` was used to assign 3D finite elements for a mechanical simulation. Then in the category of `material`, the material was defined using the operator `DEFI_MATERIAU`. For example, the material was defined as Steel using `ELAS` keyword, which has the required options to define a linear isotropic elastic material. Additionally, the work hardening effect and the elastic limit were defined using the `ECRO_LINE` keyword. The keyword `FATIGUE` is important because that is where Wöhler's Diagram (S-N Curve) is defined. It can be either implemented as a function or by specifying the values of `A_BASQUIN` and `BETA_BASQUIN`. Moreover, to define the tensile strength at the operating temperature, `SU` operand was used, which comes under the `RCCM` keyword. To assign the defined material, the operator `AFFE_MATERIAU` is used.

The loads acting on the sample were introduced as time series functions to perform an MNV fatigue analysis. For instance, the bending moment, torsion, lateral, and axial load histories were extracted from the bond graph simulation as 'CSV' files

and imported to the DEFI_FUNCTION operator through VALE keyword. This operator facilitates MNV fatigue analysis which is an advanced feature of SalomeMeca™. These operators and keywords are available in the Functions and Lists category.

In the category of Boundary Conditions and Loads (i.e. BC and Load), AFFE_CHAR_MECA operator was used to fix one end of the mesh while AFFE_CHAR_MECA_F was used to define the bending moments and forces. In order to fix one end, the FACE_IMPO keyword was used to limit the degrees of freedom in all directions. Also, the face to be fixed was selected from the mesh entities created in the meshing step. Bending moments were introduced as a moment created by a lateral load acting at the free end, while torsion was applied as a moment of a couple.

A nonlinear contact between the two bodies at the threaded connection was defined using the DEFI_CONTACT operator in CodeAster™, which comes under the category of BC and Load. To consider the geometrical nonlinearity, the keyword FORMULATION='CONTINUE' was used. Also, the ALGO_CONT and COEF_PENA_CONT combination was used to keep the global matrix asymmetry preserved while solving using a penalty method. Ignoring this step would have led to solution convergence issues. The solution of nonlinear contact was done using STAT_NON_LINE. This operator handles the geometric nonlinearity and the nonlinearity in frictional contact. If the compound mesh approach was taken rather than considering the nonlinear contact approach, both the DEFI_CONTACT and STAT_NON_LINE could have been replaced with the MECA_STATIQUE operator.

The operator CALC_CHAMP was used to automatically calculate intermediate fields to get the output of SIEQ_ELGA, which are the principal stresses. Using this operator, the need for awareness of the dependencies of the intermediate fields required to calculate SIEQ_ELGA was eliminated.

The field of fatigue damage was calculated using the CALC_FATIGUE operator.

This was accomplished by taking into account the past equivalent stresses that were computed using `SIEQ_ELGA` at each Gauss point. In this operation, the elementary loading cycles are extracted using rainflow counting. The total damage experienced by the structure is the sum of the damage associated with the elementary cycles. This operator uses Wöhler's Diagram defined in the `DEFI_MATERIAU` operator to perform the cumulative damage calculation. To extract the results, the `IMPR_RESU` procedure was used and the results were written into a 'MED' file which can be used for post-processing in Paravis™. Alternatively, the `POST_FATIGUE` operator can be used with the `IMPR_RESU` procedure to perform a multi-axial fatigue analysis that provides the results in a tabulated form. The author's online repository provides the complete code, which can be accessed through this link (https://github.com/mihiranpathmika). It is also presented in Appendix B.

5.3.2.3 Post processing

Post-processing was done in Paravis™, which is included in SalomeMeca™. Alternatively, Paravis™ can be used as a separate installation on the previously mentioned Linux and Windows platforms. Paravis™ works based on the concept of filters. Therefore, after importing the 'MED' file into Paravis™, the filter `ELGA Field to surface` was added in order to view the fatigue damage distribution. Alternatively, the post-processing tool available in CodeAster™ can also be used to determine the maximum fatigue damage. The default result is in terms of remaining fatigue life. As mentioned in CodeAster™ documentation, fatigue damage is defined as the reciprocal of remaining fatigue life.

5.4 Case study: Optimizing the fatigue life of drill collars

In this section, a case study is presented, which demonstrates the use of the proposed framework as a fatigue life optimization tool. The locations of two stabilizers are considered independent variables (factors), while fatigue damage is the dependent variable. The Design of Experiments (DoE) approach was used to develop the experimental matrix, and the experiments were carried out using the fatigue life prognosis framework of Section 5.3. The outcome is a statistical model of fatigue damage as a function of stabilizer location, which can be utilized to decide the optimal stabilizer locations for a given drilling scenario. Threaded connections are the areas most susceptible to fatigue failure because of the high stress concentration sites. Therefore, the threaded connections were used in fatigue simulations as the site of maximum predicted fatigue damage.

Drill collars are exceptionally robust industrial tubes that are located below the drill pipe neutral point, and must therefore take higher compressive loads that could cause buckling. Drill collars only make up a small fraction of the drillstring total length. For instance, a 10,000 ft (3048 m) drill string could only include 500 ft (152 m) of drill collars and 9,000 ft (2743 m) of drill pipe. Drill collars are usually manufactured in lengths similar to drill pipes and are connected vertically on the drilling rig. Drill collars are thick-walled, hefty, and have very little flexibility, in contrast to drill pipe. Usually, drill collars are employed above the outer core barrel assembly. They are mostly employed to provide weight to the drill bit. However, they also serve as a shock absorber to lessen the vibrations and impact pressures brought on by drilling [53].

The bottom hole assembly of this case study consists of five drill collars, two stabilizers, and one outer core barrel assembly. The schematic diagram and the corresponding bond graph are illustrated in Figures 5.10a and 5.10b respectively. The

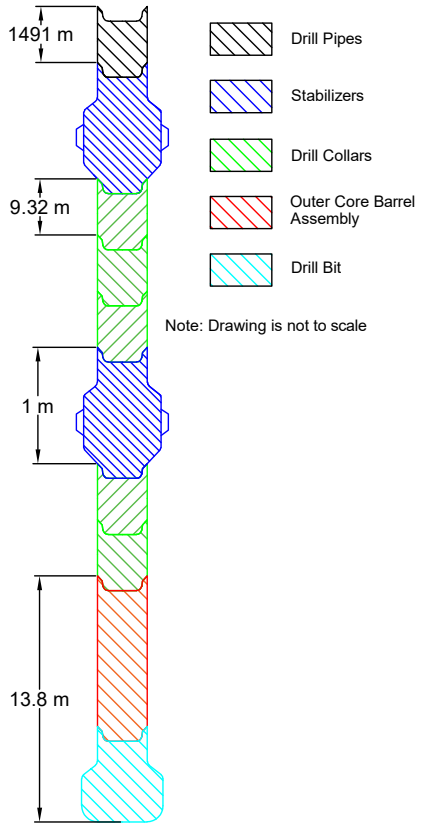

(a) Schematic diagram of the bottom hole assembly

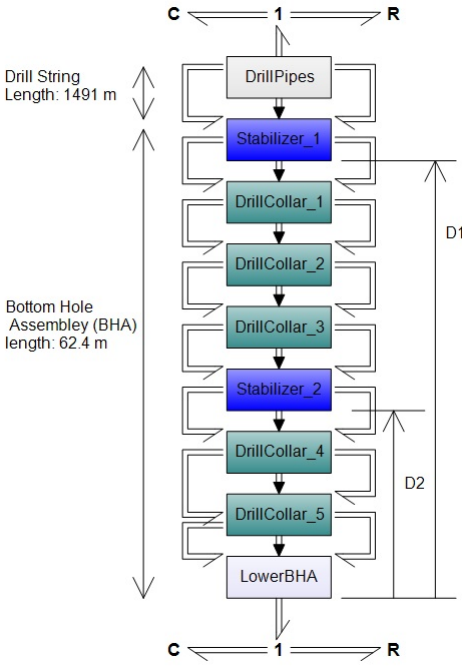

(b) Bond graph of the drill string

Figure 5.10: The location of the two stabilizers (not to scale)

outer core barrel assembly and the drill bit are represented by *LowerBHA* submodel in Figure 5.10b simulated with four bond graph elements. The submodel represents components such as the drill bit, stabilized bit sub, outer core barrel, landing saver sub, top sub, and head sub.

The locations of the stabilizers were simultaneously varied, and the maximum fatigue damage at the threaded connection was estimated for each stabilizer config-

uration. The experimental matrix consists of 13 runs. Different stabilizer location combinations are tabulated along with the corresponding maximum fatigue damages in Section 5.5.

The experimental matrix was developed following the RSM [54]. The DOE approach is used by the RSM to gather data and pinpoint important interactions and factors that affect the process response. A statistical model to represent the causal relationships between causes and responses is then presented.

5.4.1 Bond graph implementation

The 3D bond graph element model illustrated in Figure 5.11 was utilized along with the interface model presented in 5.12 to develop the bond graph simulation. As shown in Figure 5.10b, a set of drill pipes with a length of 1491 m is located above the bottom hole assembly which has a length of 64.4 m. The bond graph was parameterized using the stiffness values determined through the proposed method presented in Table 5.1.

The compliance values are coded into the capacitive (C) elements of the interface submodel shown in Figure 5.12. The topmost drill pipe and the drill bit at the bottom are given pinned boundary conditions through the use of stiff lateral springs with parallel damping. Also, the top drill pipe is provided with an effort source to drive the entire drill string.

The interaction with the wellbore is modelled using a C element representing a stiff spring oriented radially outward from the centre of the drill string as illustrated in Figure 5.13. When the eccentricity (e) sufficiently increases such that the pipe reaches the wellbore, the stiffness of the spring (K_w) becomes non-zero and generates a reaction force on the drill string. The location of the pipe axis in the cross-section considered (G) was defined using the angular displacement (ϕ) and the eccentric-

ity (e). In modelling the drill collars, four adjacent lumped segments were taken as equivalent to a drill collar, as shown in Figure 5.4 in terms of compliance and inertial parameters. Therefore, there are four elements in a given *Drill Collar* sub-model in Figure 5.10b. The stabilizer units were placed as per the experimental matrix provided in Table 5.2. As indicated in Figure 5.10b, $D1$ and $D2$ are measured from the

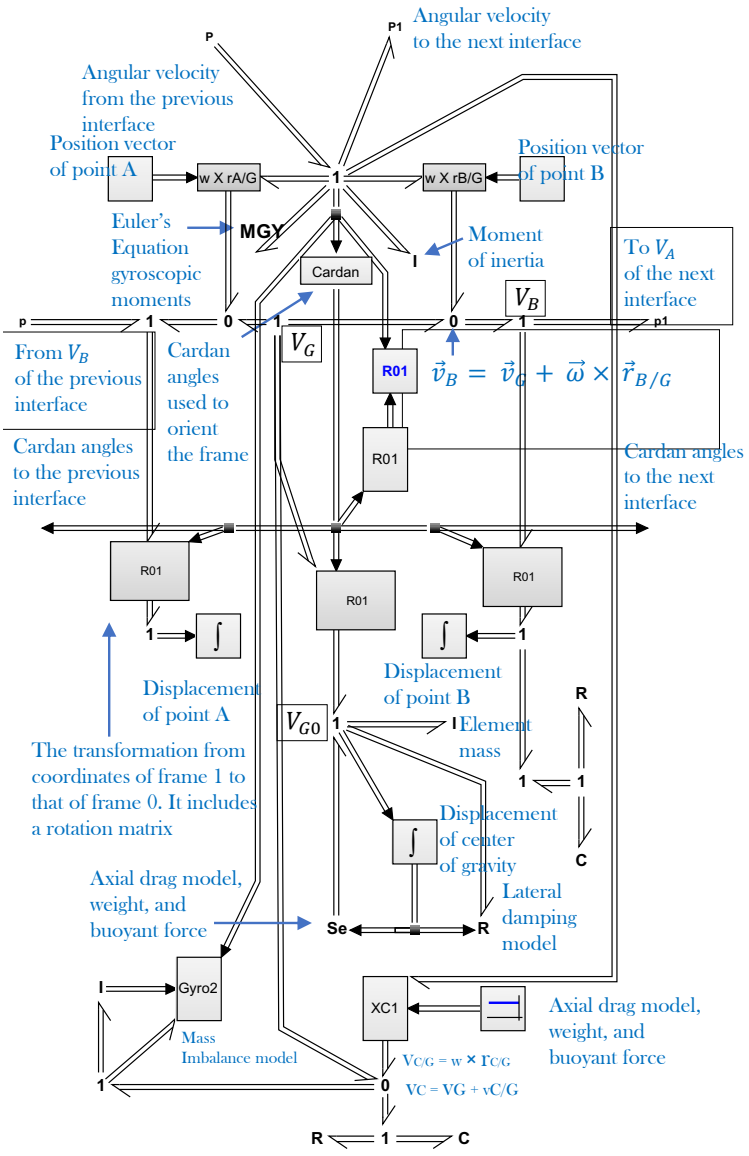

Figure 5.11: The construction of the 3D bond graph element

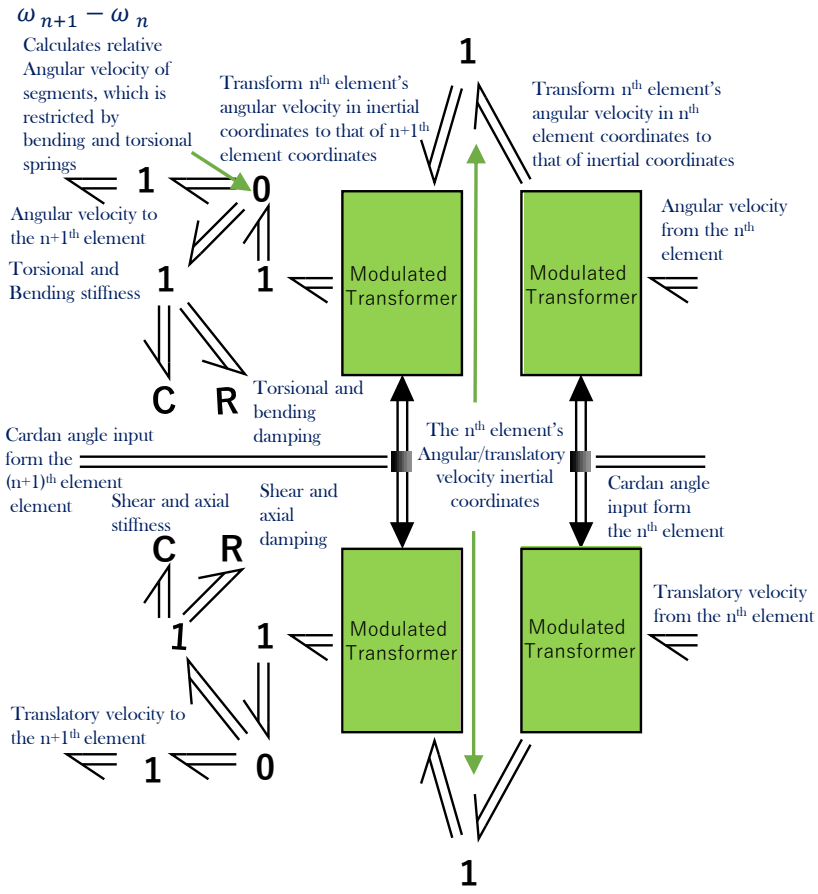

Figure 5.12: Interface submodel between two 3D bond graph elements

lowermost point of the drill bit. The simulation was run until the load fluctuations became nearly consistent. The simulated load fluctuations were extracted from the efforts of the shear, axial, bending, and torsional springs. They were exported into 'CSV' files for later use in the finite element model for MNV fatigue failure prognosis. A sample load fluctuation history for Drill Collar 1 is presented in Figure 5.14 in Section 5.5. Figures 5.14 a and b illustrate the bending moment fluctuation while Figures 5.14 e and f illustrate the shear force fluctuation on two orthogonal planes. Figure 5.14 c and d illustrate the axial and torsional load fluctuations respectively. Figure 5.15 illustrates the fatigue damage distribution of a drill collar threaded con-

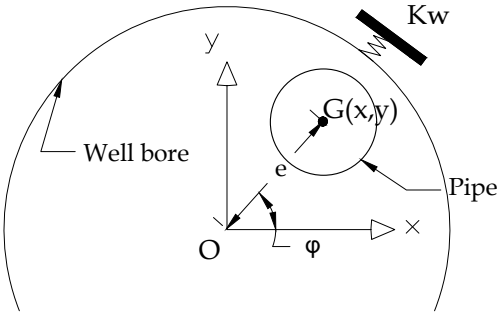

Figure 5.13: Drill pipe-well bore interaction model schematic

nection for the load fluctuation in Figure 5.14 over 60 s. The analysis was done using CodeAster™ solver in SalomeMeca™, and the post-processing was done using Paravis™.

5.5 Results

As the first step of the process, the dynamic model was developed using bond graphs. Then compliance values for drill string stabilizers, collars, and pipes were determined and the bond graph was refined accordingly. The compliance values are presented in Table 5.1. The reason for different percentage errors between theoretical method and numerical method results is explained in Section 5.6.

Table 5.1: Bond graph element compliance values

Compliance	**Stabilizer**			**Collar (corner element)**			**Pipe Element**		
	A	**B**	**% Error**	**A**	**B**	**% Error**	**A**	**B**	**% Error**
Axial	1.20×10^{-10}	2.12×10^{-10}	76.7	1.54×10^{-9}	1.59×10^{-9}	3.2	1.90×10^{-8}	1.97×10^{-8}	3.7
Shear	5.61×10^{-9}	8.31×10^{-10}	85.2	5.79×10^{-7}	7.17×10^{-9}	98.8	2.37×10^{-7}	9.44×10^{-8}	60.2
Torsional	3.68×10^{-7}	1.05×10^{-7}	71.5	1.46×10^{-6}	1.49×10^{-6}	2.1	1.20×10^{-5}	3.19×10^{-5}	165.8
Bending	1.39×10^{-9}	8.05×10^{-8}	5691.4	1.12×10^{-6}	1.14×10^{-6}	1.8	1.45×10^{-5}	2.45×10^{-5}	69.0

A - Result of the proposed method, B - Theoretical calculation result.

The case study's goal was to locate the stabilizers such that they minimize the fatigue damage of the most vulnerable drill collar for a given stabilizer configuration.

The experimental matrix and the maximum fatigue damage values of the respective stabilizer location combinations are presented in Table 5.2.

Figure 5.16 illustrates the statistical model developed through the DoE approach. According to the figure, the stabilizer location combination $D_1 = 61.4$ and $D_2 = 23.12$ provides the minimum fatigue damage while $D_1 = 61.4$ and $D_2 = 32.44$ combination gives the maximum damage. The percentage difference between the maximum and minimum fatigue damages is 200% of the minimum damage in the scenario considered.

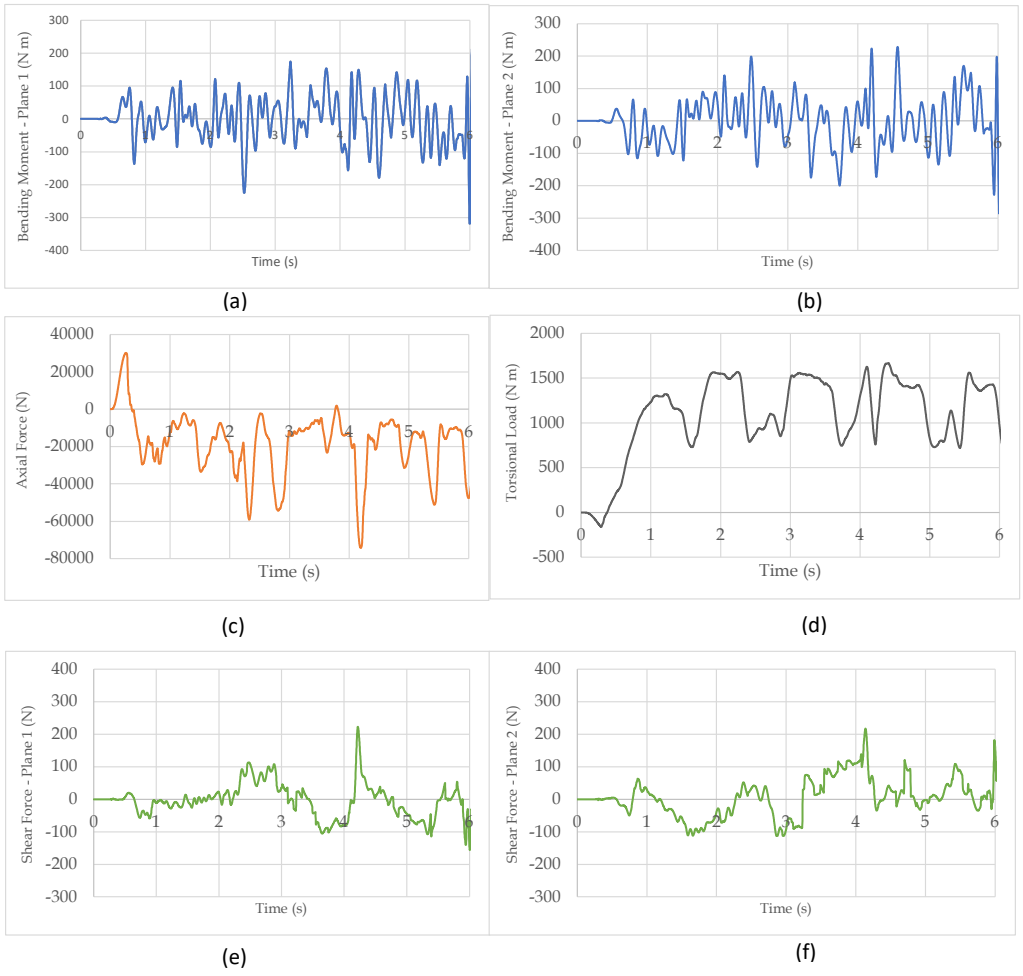

Figure 5.14: Load fluctuations on Drill Collar 1

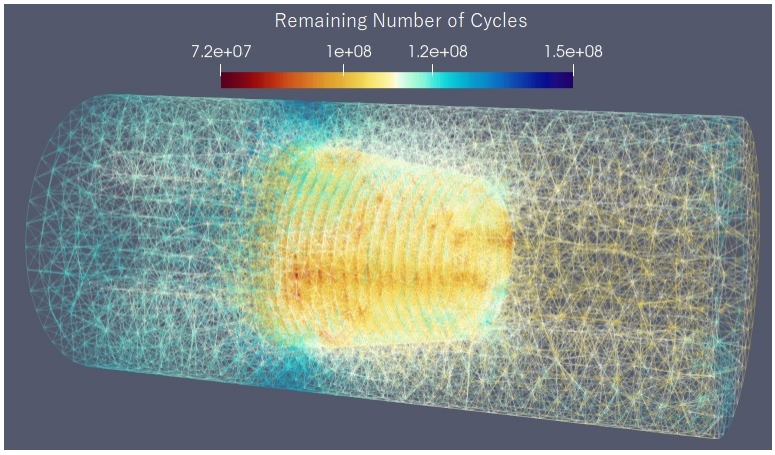

Figure 5.15: A sample simulation post-processing using Paravis™

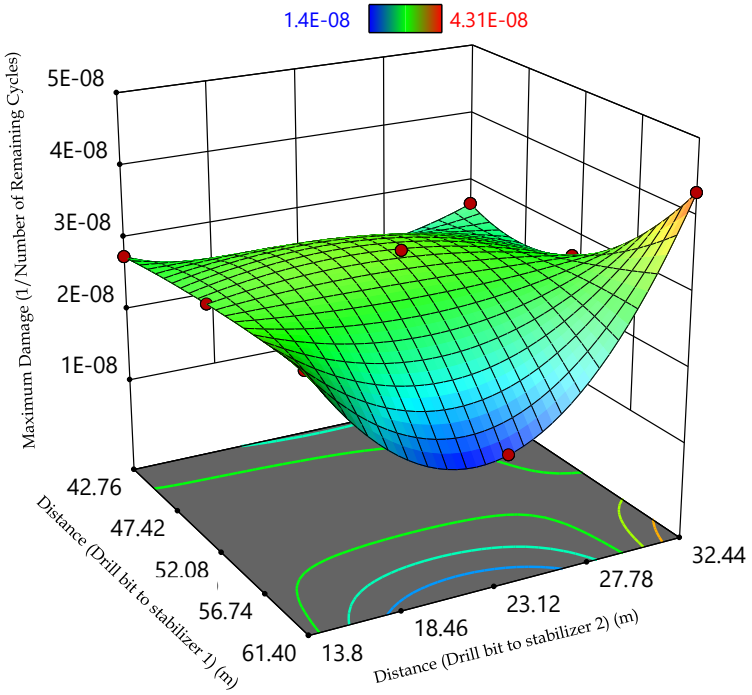

Figure 5.16: Maximum fatigue damage for different stabilizer configurations

Table 5.2: The experimental matrix

Experiment Number	Factor 1	Factor 2	Response
	Distance Drill Bit to Stabilizer 1 (D1) (m)	Distance Drill Bit to Stabilizer 2 (D2) (m)	Fatigue Damage (1/nos)
1	61.4	32.44	4.31×10^{-8}
2	52.08	23.32	3.20×10^{-8}
3	61.40	23.32	1.40×10^{-8}
4	42.76	32.44	2.67×10^{-8}
5	52.08	23.32	3.20×10^{-8}
6	42.76	23.32	2.24×10^{-8}
7	52.08	32.44	2.69×10^{-8}
8	52.08	23.32	3.20×10^{-8}
9	61.40	13.80	3.03×10^{-8}
10	52.08	23.32	3.20×10^{-8}
11	52.08	23.32	3.20×10^{-8}
12	52.08	13.80	2.96×10^{-8}
13	42.76	13.80	2.76×10^{-8}

5.6 Discussion

The current study presents a framework for estimating and optimizing the fatigue life of drill pipes and collars of a vertical oil well drill string. The MNV fatigue estimation is done using SalomeMeca™, and the required stress histories are generated using the 3D bond graph model. The developed framework was applied to optimize the fatigue life of drill collars as a proof of concept.

The 3D bond graph where the Newton-Euler approach is implemented can drastically reduce the processing time to generate stress histories compared to finite element models. Even though bond graph lumped segment models are lower-order models, they serve with sufficient accuracy in low-frequency vibration simulations. The introduction of contact simulations and friction models is comparatively convenient and computationally inexpensive. In the bond graph model, the damping constant

representing the structural damping and the drag effect due to the drilling fluid was assumed to be static. Alternatively, lateral and axial drag models developed considering the drilling fluid flow through the pipe and annular space, drilling fluid rheology, and other physical properties can be used to replace the static damping constant.

Further, a given drill collar is represented with four lumped segment bond graph elements, giving a sufficient total number of segments to accurately capture the first two vibration modes of the entire bottom hole assembly. The first two vibration modes are considered to account for the majority of vibration energy. Therefore, they should be sufficient to predict fatigue failure. Alternatively, a further increase in elements will increase the accuracy with extended simulation times as a trade-off. Figure 5.17 illustrates the accuracy of the first four natural frequencies with the increasing number of elements for a 7 m long slender structure. As it indicates, eighteen to twenty elements are sufficient to achieve accurate results for the first four natural frequencies. There can be several types of external excitations acting on a drill string. Firstly, the drill collars cannot be guaranteed to be straight after manufacturing, transportation, and stacking at the well site. Therefore, their centres of mass can get offset from the axis of rotation, which causes a mass imbalance. Due to the continuous interaction with the wellbore, defects such as washouts[1] also can contribute to it. Mass imbalances cause lateral vibrations generating bending moments in the drill string. Bit bounce can occur due to the nature of the formation being traversed, and the WOB creating axial loads and stick-slip vibrations can generate torsional vibrations. These excitations create stress fluctuations at the threaded connections, leading to fatigue failure.

Some compliance values determined using the proposed method, presented in Ta-

[1]Washout is when a hole is worn in the pipe, and becomes increasingly larger due to circulating drilling fluid. This can eventually sever or twist off the pipe entirely.

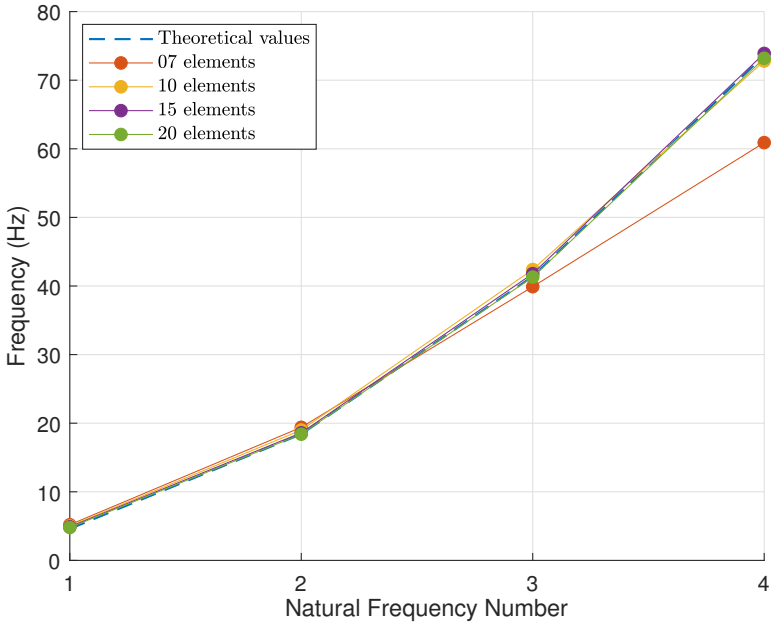

Figure 5.17: Natural frequency

ble 5.1, are distinctly different compared to their respective theoretical values. For example, the compliance values of the stabilizer element, shown in Figure 5.18a, are highly overestimated due to assuming a hollow cylindrical body with only the outer and inner diameters matched with the actual stabilizer. Figures 5.18a and 5.18b illustrate a stabilizer and its approximation, respectively. The complexity of strain distribution on the actual geometry versus the cylindrical body indicates how challenging it is to determine the deformations and hence their compliance values through theoretical calculations. This also demonstrates the disadvantage of using approximations to calculate compliance values of the lumped segment model elements. Moreover, the inaccurate estimation of compliance and other properties causes erroneous predictions of natural frequencies and other dynamic behaviours of a structure which makes the entire simulation less useful. Therefore, the proposed procedure of compliance value determination plays a major role in the accurate modelling and simulation

of vibrating structures.

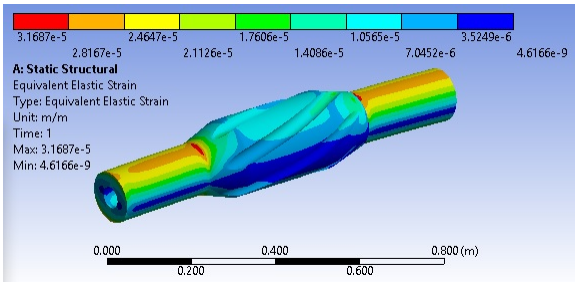

(a) Strain distribution of a stabilizer in bending

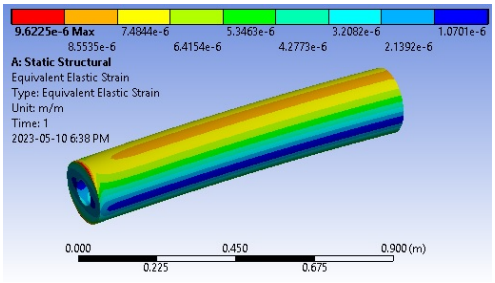

(b) Strain distribution of a simplified stabilizer in bending

Figure 5.18: Deformation comparison of a stabilizer vs its simplified element

5.7 Conclusions

This study provides a fatigue life prognosis framework for slender structures such as drill strings. The proposed framework can capture the dynamics of the vibrating structure, extract the loading history, and perform an MNV-type of fatigue analysis. Using the proposed framework, the bottom hole assembly of a vertical-well drill string was evaluated for maximum fatigue damage concerning the location of two stabilizers. Considering all five drill pipes, it can be concluded that the optimum placement of stabilizers will be $D1 = 61.40\ m$ and $D2 = 23.32\ m$. Through this arrangement of stabilizers, the maximum fatigue damage of the drill collars can be minimized. The fatigue damage of the optimal configuration was three times lesser than that of the worst-case scenario.

5.8 Further work

The current study solely focuses on optimizing the fatigue life by strategically placing the stabilizers among the drill collars. Nevertheless, some more factors may govern

the fatigue life, such as WOB and rotary speed of the drill string. A broader study can be employed with those factors included, followed by a DOE procedure and required fatigue life estimations. Further, it will be interesting to understand the effect of the drill string's varying total length and the rheological properties of the drilling fluid on fatigue damage.

The fatigue estimation framework introduced can be further developed as a Digital Twin of the drill string by integrating with a machine learning algorithm to identify the bottom hole vibration conditions through surface measurements. The machine learning (ML) algorithm can be trained to identify the vibration in terms of magnitude and type (i.e. whirling, bit bounce, stick-slip etc.). The training data can be synthetically developed using the bond graph introduced in this study. Finally, the digital twin can be developed by integrating bond graph, finite element method, and ML components which can predict the remaining fatigue life dynamically. Also, there is a potential to develop standalone software by integrating those three components, which can be developed into a marketable product.

5.9 Acknowledgement

This work was financially supported by the Natural Sciences and Engineering Research Council (NSERC) of Canada and Memorial University of Newfoundland (MUN), Canada. The authors thankfully acknowledge the continuous support provided by the Drilling Technology Laboratory (DTL) research group, the Intelligent Systems Laboratory, and the Mechanical Division of Technical Services at MUN, Canada.

References

[1] C. Stelzer, *Drillpipe Failure and its Prediction.* PhD thesis, Mining University Leoben, 2007.

[2] M. Albdiry and M. Almensory, "Failure analysis of drillstring in petroleum industry: a review," *Engineering Failure Analysis*, vol. 65, pp. 74–85, 2016.

[3] H. Xie, J. Zhou, and P. Zhang, "Simulation research on vibration parameters model of drill string," *Fuel*, vol. 315, may 2022.

[4] J. Abdo, E. M. Hassan, K. Boulbrachene, and J. C. Kwak, "Drillstring failure—identification, modeling, and experimental characterization," *ASCE-ASME Journal of Risk and Uncertainty in Engineering Systems, Part B: Mechanical Engineering*, vol. 5, no. 2, p. 021004, 2019.

[5] W. C. Chen, "Drillstring fatigue performance," *SPE Drilling Engineering*, vol. 5, no. 2, pp. 129–134 16076, 1990.

[6] G. Y. Grondin and G. L. Kulak, "Fatigue testing of drillpipe," *SPE Drilling and Completion*, vol. 9, no. 2, pp. 95–102, 1994.

[7] M. J. Knight and F. P. Brennan, "Fatigue life improvement of drill collars through control of bore eccentricity," *Engineering Failure Analysis*, vol. 6, no. 5, pp. 301–319, 1999.

[8] M. Galagedarage Don and G. Rideout, "Fatigue failure prognosis of an oil well drill string using a lumped segment bond graph model and finite element method," in *ICBGM'2021*, (San Diego, California USA), pp. 1–14, Society for Modeling & Simulation International (SCS), 2021.

[9] A. Ambrus, P. Ashok, D. Ramos, A. Chintapalli, A. Susich, T. Thetford, B. Nelson, M. Shahri, J. McNab, and M. Behounek, "Self-learning probabilistic detection and alerting of drillstring washout and pump failure incidents during drilling operations," *Society of Petroleum Engineers - IADC/SPE Drilling Conference and Exhibition, DC 2018*, vol. 2018-March, pp. 6–8, 3 2018.

[10] O. Ozguc, "Analysis of fatigue behaviour of drill pipe on pin-box connection," in *Proceedings of the Institution of Mechanical Engineers Part M: Journal of Engineering for the Maritime Environment*, vol. 235, pp. 68–80, 2021.

[11] T. Martins, V. Infante, L. Sousa, A. Fonseca, P. J. Antunes, A. M. Moura, and B. Serrano, "Numerical and experimental study of aircraft structural health," *International Journal of Fatigue*, vol. 132, 3 2020.

[12] S. R. Yeratapally, P. E. Leser, J. D. Hochhalter, W. P. Leser, and T. J. Ruggles, "A digital twin feasibility study (part i): Non-deterministic predictions of fatigue life in aluminum alloy 7075-t651 using a microstructure-based multi-scale model," *Engineering Fracture Mechanics*, vol. 228, p. 106888, 2020.

[13] G. Li, S. Datta, A. Chattopadhyay, N. Iyyer, and N. Phan, "An online-offline prognosis model for fatigue life prediction under biaxial cyclic loading with overloads," *Fatigue and Fracture of Engineering Materials and Structures*, vol. 42, pp. 1175–1190, 5 2019.

[14] P. E. Leser, J. E. Warner, W. P. Leser, G. F. Bomarito, J. A. Newman, and J. D. Hochhalter, "A digital twin feasibility study (part ii): Non-deterministic predictions of fatigue life using in-situ diagnostics and prognostics," *Engineering Fracture Mechanics*, vol. 229, p. 106903, 2020.

[15] N. Eleftheroglou, D. Zarouchas, T. Loutas, R. C. Alderliesten, and R. Benedictus, "Online remaining fatigue life prognosis for composite materials based on strain data and stochastic modeling," in *Key Engineering Materials*, vol. 713, pp. 34–37, Trans Tech Publ, 2016.

[16] G. De Roeck, G. Degrande, G. Lombaert, and G. Muller, "Fatigue life prognosis for structural elements under stochastic wind loading based on spectral methods," in *Proceedings of the 8th International Conference on Structural Dynamics - EURODYN*, 1629-1635, (Leuven, Belgium), July 2011.

[17] B.-R. You and S.-B. Lee, "A critical review on multiaxial fatigue assessments of metals," *International Journal of Fatigue*, vol. 18, no. 4, pp. 235–244, 1996.

[18] J. A. Bannantine and D. F. Socie, "A variable amplitude multiaxial fatigue life prediction method," *Third International Conference on Biaxial/Multiaxial Fatigue*, pp. 12.1 – 12.20, 1989.

[19] R. Browell and A. Hancq, "Calculating and displaying fatigue results," *ANSYS Inc*, vol. 2, pp. 1–42, 2006.

[20] nCode, "Comparison of fatigue analysis methods ncode," 2022. https://www.ncode.com/videos/216-comparison-of-fatiue-analysis-methods.

[21] Maritime, "Corrosion fatigue of the drill pipes," 03 2021. https://www.libramar.net/news/corrosion_fatigue_of_the_drill_pipes.

[22] M. Palimi, Y. Tang, V. Alvarez, E. Kuru, and D. Li, "Green corrosion inhibitors for drilling operation: New derivatives of fatty acid-based inhibitors in drilling fluids for 1018 carbon steel in co2-saturated kcl environments," *Materials Chemistry and Physics*, vol. 288, p. 126406, 2022.

[23] B. K. Paswan and V. Mahto, "Development of environment-friendly oil-in-water emulsion based drilling fluid for shale gas formation using sunflower oil," *Journal of Petroleum Science and Engineering*, vol. 191, p. 107129, 2020.

[24] CodeAster, "Salome meca code aster," 2021. https://www.code-aster.org/V2/spip.php?article303.

[25] S. Plessis, "Operator post fatigue," 10 2013. http://www.gnu.org/copyleft/fdl.html.

[26] V. Feodos'Ev, "Vibrations and stability of a pipe when liquid flows through it," *Inzhenernyi Sbornik*, vol. 10, no. 1, pp. 69–70, 1951.

[27] H. Ashley and G. Haviland, "Bending vibrations of a pipe line containing flowing fluid," *Journal of Applied Mechanics*, vol. 17, pp. 229–232, 04 2021.

[28] F. I. Niordson, *Vibrations of a cylindrical tube containing flowing fluid*. Lindståhl, 1953.

[29] S. Chen, M. t. Wambsganss, and J. Jendrzejczyk, "Added mass and damping of a vibrating rod in confined viscous fluids," *American Society of Mechanical Engineers*, 1976.

[30] S. Chen, "Fluid damping for circular cylindrical structures," *Nuclear Engineering and Design*, vol. 63, no. 1, pp. 81–100, 1981.

[31] M. P. Paidoussis and N. Issid, "Dynamic stability of pipes conveying fluid," *Journal of sound and vibration*, vol. 33, no. 3, pp. 267–294, 1974.

[32] E. J. Kjolsing and M. D. Todd, "Damping of a fluid-conveying pipe surrounded by a viscous annulus fluid," *Journal of Sound and Vibration*, vol. 394, pp. 575–592, 2017.

[33] R. A. Ibrahim, "Overview of mechanics of pipes conveying fluids-part I: Fundamental studies," *Journal of Pressure Vessel Technology, Transactions of the ASME*, vol. 132, no. 3, pp. 0340011–03400132, 2010.

[34] F. Liang, Y. Qian, Y. Chen, and A. Gao, "Nonlinear forced vibration of spinning pipes conveying fluid under lateral harmonic excitation," *International Journal of Applied Mechanics*, p. 2150098, 2021.

[35] D. G. Rideout, A. Ghasemloonia, F. Arvani, and S. D. Butt, "An intuitive and efficient approach to integrated modelling and control of three-dimensional vibration in long shafts," *International Journal of Simulation and Process Modelling*, vol. 10, no. 2, pp. 163–178, 2015.

[36] Y. Khulief and H. Al-Naser, "Finite element dynamic analysis of drillstrings," *Finite elements in analysis and design*, vol. 41, no. 13, pp. 1270–1288, 2005.

[37] Y. Khulief, F. Al-Sulaiman, and S. Bashmal, "Vibration analysis of drillstrings with string—borehole interaction," *Proceedings of the Institution of Mechanical Engineers, Part C: Journal of Mechanical Engineering Science*, vol. 222, no. 11, pp. 2099–2110, 2008.

[38] Y. Khulief and F. Al-Sulaiman, "Laboratory investigation of drillstring vibrations," *Proceedings of the Institution of Mechanical Engineers, Part C: Journal of Mechanical Engineering Science*, vol. 223, no. 10, pp. 2249–2262, 2009.

[39] H. Qiu, J. Yang, S. Butt, and J. Zhong, "Investigation on random vibration of a drillstring," *Journal of Sound and Vibration*, vol. 406, pp. 74–88, 2017.

[40] M. Sarker *et al.*, *Modeling and simulation of vibration in deviated wells.* PhD thesis, Memorial University of Newfoundland, 2017.

[41] A. Mukherjee, R. Karmakar, and A. K. Samantaray, *Bond graph in modeling, simulation and fault identification*. IK International New Delhi, 2006.

[42] D. C. Karnopp, D. L. Margolis, and R. C. Rosenberg, *System dynamics: modeling, simulation, and control of mechatronic systems*. John Wiley & Sons, 2012.

[43] E. Szücs, *Fundamental Studies in Engineering 2- Similitude and modelling*. Elsevier, 1980.

[44] G. P. Sotomayor, J. C. Plácido, and J. C. Cunha, "Drill string vibration: How to identify and suppress," *SPE Latin American and Caribbean Petroleum Engineering Conference Proceedings*, vol. 1997-August, 8 1997. http://onepetro.org.

[45] M. Dykstra, D.-K. Chen, and T. Warren, "Experimental evaluations of drill bit and drill string dynamics," in *SPE Annual Technical Conference and Exhibition*, OnePetro, 1994.

[46] C. Langeveld, "Pdc bit dynamics," in *IADC/SPE Drilling Conference*, OnePetro, 1992.

[47] S. Rewcastle and T. Burgess, "Real-time downhole shock measurements increase drilling efficiency and improve mwd reliability," in *IADC/SPE Drilling Conference*, OnePetro, 1992.

[48] S. Irawan, A. K. Shanmugam, M. I. P. Hidayat, and T. R. Biyanto, "Study of lateral vibration of drilling string with mass imbalance using finite element," *International Journal on Advanced Science, Engineering and Information Technology*, vol. 9, no. 3, pp. 816–821, 2019.

[49] L. P. de Moraes and M. A. Savi, "Drill-string vibration analysis considering

an axial-torsional-lateral nonsmooth model," *Journal of Sound and Vibration*, vol. 438, pp. 220–237, 1 2019.

[50] L. Tang, H. Yao, and C. Wang, "Development of remotely operated adjustable stabilizer to improve drilling efficiency," *Journal of Natural Gas Science and Engineering*, vol. 95, p. 104174, 11 2021.

[51] M. Sarker, D. G. Rideout, and S. D. Butt, "Dynamic model for longitudinal and torsional motions of a horizontal oilwell drillstring with wellbore stick-slip friction," *Journal of Petroleum Science and Engineering*, vol. 150, pp. 272–287, 2017.

[52] M. Galagedarage Don and G. Rideout, "An experimentally-verified approach for enhancing fluid drag force simulation in vertical oilwell drill strings," *Mathematical and Computer Modelling of Dynamical Systems*, vol. 28, no. 1, pp. 197–228, 2022.

[53] E. S. Group, "Drill collars," 2022. https://drillpipesupply.com/drill-collars/.

[54] M. A. Hadiyat, B. M. Sopha, and B. S. Wibowo, "Response surface methodology using observational data: A systematic literature review," *Applied Sciences*, vol. 12, no. 20, p. 10663, 2022.

Chapter 6

A Digital Twinning Methodology for Vibration Prediction and Fatigue Life Prognosis of Vertical Oil Well Drillstrings

Abstract

A detailed methodology to develop a digital twin has many useful applications in the era of technology 4.0. This study provides a framework to develop a digital twin for vibration prediction and fatigue life prognosis of a vertical oil well drillstring. The nature and the severity of the down-hole vibrations are identified and estimated based on the vibrational and operational parameter measurements made at the surface level. Because of the difficulty in accessing full-scale industrial drilling data, a reduced-scale drillstring was constructed that could exhibit bit bounce, stick-slip and whirl. A bond graph simulation model was tuned to match the apparatus, and then used to generate synthetic training data. The trained machine learning algorithm can classify the incoming surface monitoring data from the physical twin into different types and severities of vibration states which are not otherwise observable. Moreover, the classified vibration condition is used to re-configure the bond graph model with

appropriate complexity to generate a loading history for fatigue life prognosis. The fatigue life estimation uses a novel combination of a low-complexity model of the entire drillstring and a high fidelity finite element model of components where stress concentrations are most severe. The digital twin detected the vibration type and its severity and estimated the remaining fatigue life of the physical system using only measurements of the motor current, rig floor axial vibration, and rotary speed.

Keywords: *Digital Twin, Bond graph, Hidden Markov model, Surface monitoring, Drillstring*

Co-authorship Statement

This chapter is a manuscript of a full paper that is submitted to Journal of IEEE Access. The co-authorship statement for this chapter follows:

The declaration applies to the following article
M. Galagedarage Don and Rideout, G., *A digital twinning methodology for vibration prediction and fatigue life prognosis of vertical oil well drillstrings.* IEEE Access **Article status: Published** The PhD student analyzed the literature, performed the experiments, collected the data, developed the codes and prepared the manuscript. The supervisor edited, helped organize the manuscript, and contributed to the choice of case studies.

6.1 Introduction

Downhole drillstring vibrations, especially high-frequency vibrations, are not observable from the ground level due to wave attenuation and bandwidth limitation of the currently-used measuring techniques [1]. As mentioned in [2], a number of telemetry methods have been developed over the years to transfer measured data to the surface, including mud-pulse (MP), electromagnetic (EM), wired-drill-pipe, and acoustic

telemetry. While the wired-drill-pipe telemetry can transport data up to 57 kbps, the MP and EM telemetry systems can only communicate data at rates of about up to 10 bps. In offshore applications, EM telemetry is ineffective, and wired drill pipe telemetry is expensive and prone to malfunction when the wiring link between the transmitter and receiver is lost. Acoustic telemetry has the capacity to communicate at rates up to hundreds of bits per second. These transmission rates are insufficient for near real-time surface monitoring of high-frequency downhole vibrations. Therefore, both the detection and control of such vibrations are done at the bottom of the well [1, 3].

Nevertheless, the availability of rich vibrational data is essential for applications such as fatigue life prognosis of drill pipes. Timely detection of such conditions helps to make effective rectifications of the operations and hence to reduce the risk and to assure reliability. This allows the driller to take action to mitigate the vibration, for example, by reducing WOB and/or increasing rotational speed to address stick-slip. The high cost for the downhole measurement of the drillstring vibrations consequently encourages machine learning approaches to downhole vibration prediction during drilling [4]. The limited availability of reliable training data for machine learning algorithms is also a challenge. A digital twin of a drillstring has the potential to generate synthetic data for different 'what-if' scenarios [5], which may be a solution for this problem. Therefore, the current study is focused on developing a digital twin which has the ability to generate its own data, by performing a series of simulations, to train its machine learning algorithms in order to make useful predictions such as downhole vibration state and fatigue life prognosis.

The overall outcome of the current study is a digital twin for a vibrating structure, in this case an oil well drillstring. The process starts with a physical system that is susceptible to vibration problems that a) can be classified (stick-slip, bit bounce,

and whirl for drilling) and b) are not easily detected because direct measurement is not practical. A dynamic simulation model of the physical system is then created and parameterized, including virtual sensors to generate time series of practically available measurements. The virtual measurements corresponding to the selected types of vibration from the simulation model are used to train a machine learning algorithm. Measurements of actual physical system vibration can be input to the trained algorithm to identify vibration type and severity. Once vibration is detected and classified, the simulation model is configured to replicate it, and generate stress histories. The stress histories are exported to a finite element model for fatigue life prognosis.

Section 6.2 reviews literature on digital twinning, vibration measurement in drilling, drillstring modelling, and machine learning algorithms. Section 6.3 gives an overview of the process and introduces the techniques used at each stage. Sections 6.4 to 6.7 give detailed development of the case study system, simulation model, machine learning algorithm and training, and fatigue life prediction. Section 6.8 provides results, and discussion and conclusions are in Sections 6.9 and 6.10.

6.2 Background study

6.2.1 Digital twins

This section introduces the digital twin concept and presents some recent developments along with their strengths and weaknesses.

"Digital twin" is a term that has been used in the recent past to describe a digital replica of a physical system. However, there is no consolidated view on what digital twins are [6]. The concept of 'digital twin' was first introduced by Michael Grieves

at the University of Michigan in 2003 through Grieves' Executive Course on Product Lifecycle Management [7]. According to [5], the term 'digital twin' carries various definitions, and the term is often misinterpreted. As mentioned in their review, on some occasions, just a 3D visualization of a physical system is referred to as a digital twin. According to the broadest definition identified by [5], a digital twin is an "integrated multi-physics, multi-scale, probabilistic simulation of an as-built system, enabled by digital thread, that uses the best available models, sensor information, and input data to mirror and predict activities or performance over the life of its corresponding physical twin"[8].

Meanwhile, [9] defines three types of digital twins: Product, Process, and Performance. Product digital twins are used for the efficient design of new products, while Process digital twins are used in manufacturing and production planning. Performance digital twins are used to capture, analyze, and act on operational data. According to this classification [9], the outcome of the current study can be classified as a Performance digital twin.

A digital twin conceptual framework for a dynamic structural damage problem is presented by [6], in which a physics-based model coupled with a Quadratic Discriminant-based classifier algorithm was introduced. The proposed conceptual framework could be adapted to implement a Product digital twin, which can prognose the fatigue failure of a vibrating structure.

A digital twin concept was proposed in [10] to estimate the structural life of aircraft components. It was envisioned that during the industry 4.0 technology level, the manufacturer could automatically populate the high-fidelity Product digital twin during manufacturing. While in operation, based on the sensor readings and other inputs, the digital twin would be capable of estimating structural life. However, as further mentioned in [10], the measured aircraft weight while in operation, which is

a crucial input to the digital twin, still involves cumbersome ground equipment and input with assumptions given by the flight crew, and is hence not accurate at the moment.

In addition to damage or life predictions of systems, the digital twin approach can be used in process optimization. A novel hybrid framework introduced by [11] combines machine learning methods with API laboratory procedures, onsite measurement data, and fluid rheology to adequately describe the drilling fluids. This approach can leverage the drilling performance by optimizing cutting transport and hence get an efficient rate of penetration (ROP). Further, as proposed by [12], digital twins can support planning, real-time analysis, real-time automated monitoring, forecasting simulation, and forward-looking simulations of problematic situations.

The use of digital twins in the fatigue life prognosis of drillstrings is not reported in the literature. Mathematical modelling, vibration simulations, fatigue analysis, and classification of surface monitoring measurements using machine learning algorithms are found as isolated studies in most cases and a holistic approach is not available in the literature. The current study addresses this by presenting a digital twin development procedure integrating dynamic modelling, vibration simulation, machine learning, and fatigue analysis.

6.2.2 Surface monitoring techniques and their importance

Prior work has studied the feasibility of surface monitoring in estimating downhole vibration conditions. In order to learn more about bit-rock interaction, vibrations at the top of the drillstring were initially recorded and processed in the 1960's [13]. The contact between the bit and the rock during rotary or motor drilling generates forces and displacements in the drillstring. As further mentioned in [13], in the case

of rotary drilling, additional stresses are produced between the drillstring and the wellbore wall. Another type of excitation comes from the fluid pulses produced by reciprocating mud pumps. Along the accessible mechanical and fluid routes, the forces from all these connected phenomena interact and transmit toward the surface. Measurements of stresses and accelerations made at the surface level can help to understand the downhole vibration conditions.

A study to understand the correlation between tri-cone bit wear conditions based on the different drilling signal measurements made at the surface level and drilling vibration analysis is presented in [14]. Several rigs were instrumented with data acquisition units including sensors to measure hoist motor current, rotary motor current, head encoder position, bailing air pressure, hoist voltage, rotary voltage, lower-mast vibration, and upper-mast vibration signals. The vibration was sensed using two accelerometers installed at approximately 2/3 of the drill mast height and the mast base. It was found that the rotary motor current signal statistical features are sensitive to bit wear which is related to the rotational speed [14]. Also, in their study on rock drilling operations, [15] concluded that vibration signals have significant potential for determining the degree of tool wear. Both the methods presented in [14] and [15] require downhole measurements to train the algorithms for the classification of vibration states.

A model using an artificial neural network (ANN) to anticipate the vibration of the drillstring when drilling a horizontal segment was presented by [16]. The three different forms of drillstring vibrations: axial, torsional, and lateral, were predicted by the ANN model using the surface drilling parameters as model inputs. Flow rate, mud pumping pressure, surface rotating speed, top drive torque, weight on bit, and ROP were the surface monitoring drilling parameters used. An equation for real-time estimation of the down-hole vibrations was proposed using the model developed. The

approach of [16] required actual data to train the machine learning algorithm, which is not always a readily available factor in most situations.

Severe downhole stick-slip vibrations can be identified solely based on surface monitoring drilling data in the method proposed by [4]. It categorizes multi-channel drilling data acquired at the surface by employing a deep neural network model to identify downhole vibration events. This method requires both surface monitoring measurements and downhole measurements to train the deep neural network in order to perform this task.

Severe downhole stick-slip vibrations can be identified solely based on surface monitoring drilling data in the method proposed by [4], which categorized multi-channel drilling data acquired at the surface by employing a deep neural network model to identify downhole vibration events. This method required both surface monitoring measurements and downhole measurements to train the deep neural network in order to perform this task.

The patent presented in [17] also uses a surface monitoring technique to estimate the downhole lateral vibrations. The algorithm used is fine-tuned using the data taken from the downhole sensor. Once the algorithm is trained, it has the ability to detect lateral vibration. As per the observations, it was deduced that an increase in the moving average of drillstring torque or a decrease in the variation of drillstring torque is a sign of lateral vibration, which ultimately leads to a reduction of ROP. This method was limited to lateral vibration and whirling detection. Physical data was used in training the algorithm.

The above contributions emphasize the viability of surface-level monitoring of drill string vibrations. The training of a machine learning algorithm by employing a sophisticated drill string multi-physics simulation to identify various vibration categories and their intensities has not yet been investigated.

6.2.3 Algorithm training using synthetic data

Any artificially-generated information not originating from events or objects in the real world can be given the designation 'synthetic data'. Simulations have the potential to generate synthetic data which can mimic the actual scenario, and the generated data can be used to train a machine learning algorithm for a variety of uses. Synthetic data has a number of key advantages, including the ability to generate large training data sets without the need for manual labelling of data and the reduction of restrictions associated with the use of regulated or sensitive data. They can also be customized to match circumstances that real-world data does not permit at a low cost. Higher data quality, scalability, and ease of use are some advantages, to name a few [18, 19].

Synthetic data is used in software data-driven testing due to its flexibility, scalability, and realism [18]. In some cases, synthetic training data outperforms real-world data and is essential for creating superior Artificial Intelligence (AI) models. This is because rare incidents also can be simulated, and data can be generated, which facilitates better algorithm training covering the entire spectrum of events. Moreover, it helps to eliminate some practical issues in using real-world data, such as biases in data which lead to skewness and inaccuracy of the model. A variation on synthetic data is *partially* synthetic data that keeps some of the original data set and performs a gap-filling using the simulated data. Hybrid synthetic data combines the real-world and generated data, which creates an opportunity to acquire the benefits of both fully synthetic and partially synthetic data.

Further details on synthetic data usage in machine learning algorithm training and its practical limitations relevant to the current study are presented in Section 6.9.

6.2.3.1 An open-source hidden Markov model toolbox

An open-source HMM toolbox is presented in [20], which provides improved flexibility in developing fault detection tools [21]. The operating concept is explained in Section 6.3.2, which explains the suitability of using HMM for surface monitoring applications. When using this toolbox, the user does not need to evaluate the prior probabilities or transition probabilities of states which is a requirement of most of the commercial software tools. Instead, the algorithm can be trained using the training data set to generate them. A detailed description of the HMM open-source toolbox is available in [20, 21] for further information.

6.2.4 Drillstring simulation

According to [22], the modelling of lateral vibrations of drillstrings has been explored since the mid-1960s. Analytical and finite element modelling approaches have been the most widely used. Although initial attempts relied on closed-form analytical solutions, the extreme complexity of vibrations and interactions with the well bore set limits to this approach. Therefore, the latter approach has become more common with the advancement of computer processing speeds but may be of limited use in design exercises because of excessive simulation times [23].

Physical system modelling can be more effective when using an approach that allows easy integration of components from different energy domains such as fluid, electrical, thermal, and mechanical. A typical drillstring simulation involves, but is not limited to, induction motors, fluid flows, structural vibrations, and heat transfer submodels. Sometimes it can be cumbersome to simulate each mechanism or phenomenon in their own domains and combine to get the overall output [24]. Although it is feasible for certain scales and complexity levels, the computational cost may be

massive when the system becomes larger and more complicated.

It is beneficial to bring all the domains into one common platform to simplify the problem. Energy can be used to play the role of the 'common currency' in this kind of situation. The bond graph method [23–25] uses a small set of generalized elements to represent power storage, dissipation, boundary conditions, continuity, and compatibility constraints. The element symbols and connection rules are the same regardless of the energy domain, making multi-domain modelling straightforward. Further details on bond graphs can be found in [23–25].

References [23, 26, 27] present drillstring bond graph simulations using the Newton-Euler formulation and a body-fixed coordinate system. Rigid lumped segments were connected to each other with axial, shear, bending, and torsional springs such that the behaviour of the model approached that of a continuous system as the number of elements increases. Figures 6.1a, 6.1b and 6.1c illustrate the first three types, while the torsional spring can be considered as a similar spring to the one in Figure 6.1c but with a rotational degree of freedom. These springs are analogues to the struc-

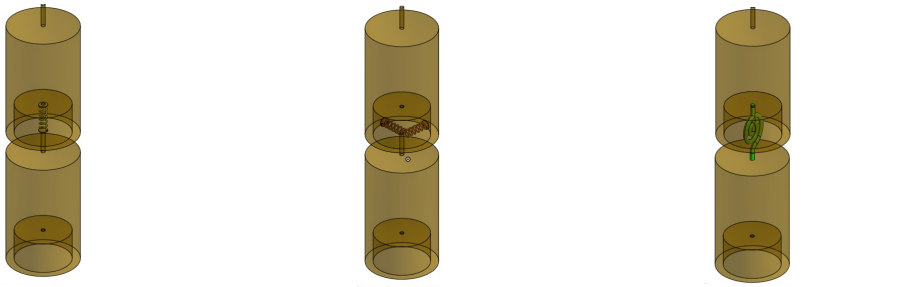

(a) Axial compliance (b) Shear compliance (c) Bending compliance

Figure 6.1: Bond graph element compliances

ture's elasticity which are represented by capacitive (compliant) elements in the bond graph.

A flexible nonlinear drillstring model developed based on Lagrangian dynamics is also possible, as presented in [28]. The simulation included lateral bending, longitu-

dinal motion, and torsional deformation dynamics. Because of the comparative ease of extracting constraint and internal forces, a Newton-Euler formulation with lumped segments is used in this paper.

The stress history at a specific location can be determined using the effort fluctuations of the compliances in the bond graph that represent the springs in Figure 6.1a, as was done in [28] and in the lumped segment bond graph models previously published by the authors. That stress history can then be used in software such as SalomeMeca™ to perform fatigue estimation for multiaxial, non-proportional, and variable amplitude MNV loading scenarios. SalomeMeca™ is an open-source software that provides considerable flexibility in performing FEA simulations. A detailed description of the fatigue life estimation workflow is provided in [29].

In summary, this paper will leverage the bond graph approach, with lumped segments, to (1) represent a vertical drillstring physical apparatus, (2) generate training data for a machine learning algorithm to predict vibration, (3) predict stress history based on the physical system vibration that has been detected by the algorithm, and (4) use the stress history in SalomeMeca™ to give a fatigue prognosis.

6.3 Methodology

This section presents the methodology for developing the digital twin framework. Figure 6.2 is a flow chart showing the integration of the dynamic model, machine learning algorithm, physical system, and finite element post-processing into a digital twin capable of vibration prediction and fatigue failure prognosis. The bond graph simulations generated three types of vibrations: stick-slip, bit bounce, and whirling at three different levels of severity: high (H), medium (M), and low (L). Nine different parameter sets were used to generate the data sets. The synthetically generated data

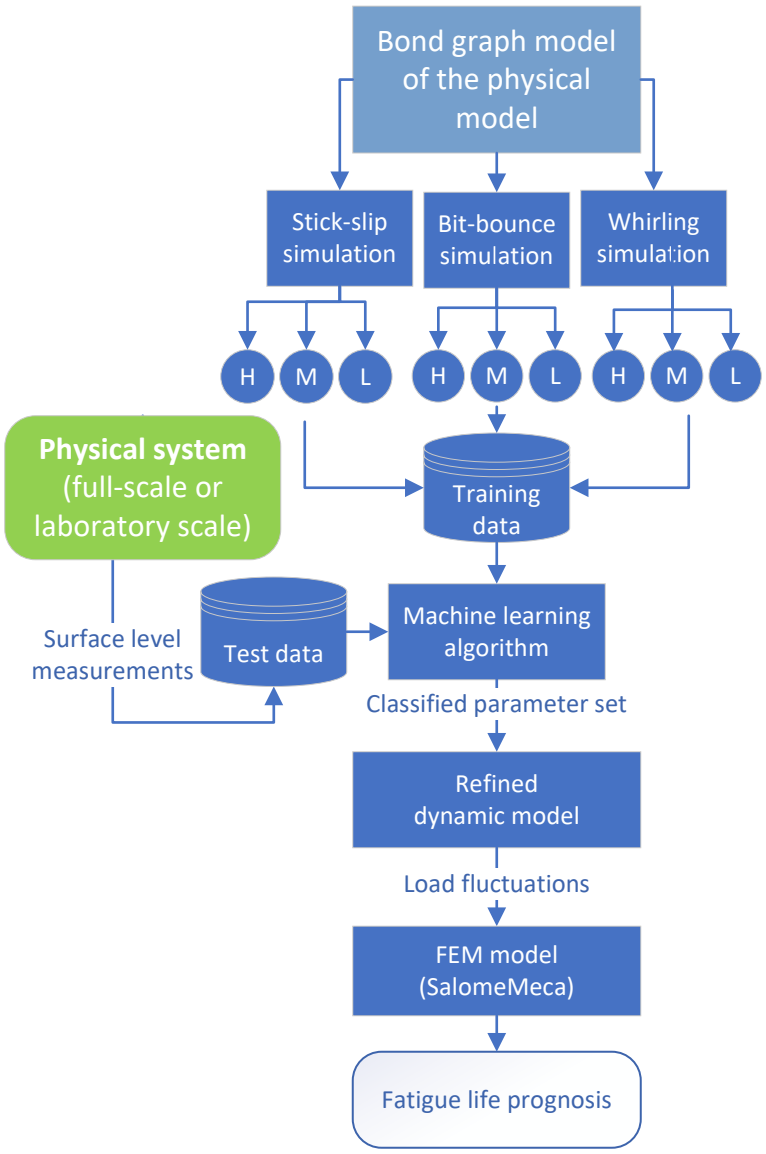

Figure 6.2: Proposed digital twin framework

was used as the training data for the machine learning algorithm. Therefore, the trained algorithm is capable of classifying the incoming surface monitoring measurements originating from the physical model into one of the nine categories. Depending on the classification, the bond graph is reconfigured with the relevant parameter set and inputs to create that vibration scenario. The generated load fluctuation history

from the bond graph is then used in the finite element model, which can prognose the fatigue life of the drillstring. The following sub-sections provide a detailed step-by-step description of the procedure.

6.3.1 The bond graph model and its function

The primary requirement of the bond graph is to simulate the potential drillstring dynamics for a given set of boundary conditions and operating parameters. Also, it should provide stress histories for fatigue life prognosis. Later damping, contact spring and friction force, and axial drag forces must be computed within the model. The number of elements can be decided based on the desired simulation speed and the modes of vibration considered. Once the simulation is set up, the bit bounce, stick-slip, and whirling scenarios can be created, and the corresponding surface-level responses can be recorded. These data are used to train the machine learning algorithms to classify unknown vibrations. These steps are described in detail in Section 6.5. All the bond graph simulations and codes can be accessed through the author's online repository (https://github.com/mihiranpathmika).

6.3.2 The use of Hidden Markov Model (HMM) in surface monitoring applications

HMM is a statistical Markov model in which the system being modelled is assumed to be a Markov process [30] with 'hidden' states. Figure 6.3a illustrates the basic concept of the function of the HMM. According to that, the unobservable states can be indirectly studied by observing partially related incidents. $P1$ through $P8$ are the respective probabilities of changing one state to another indicated by the arrows. Knowing these prior probabilities, the user can deduce the likelihood of 'hidden'

states by looking at the observable incident. In the current study, the same concept

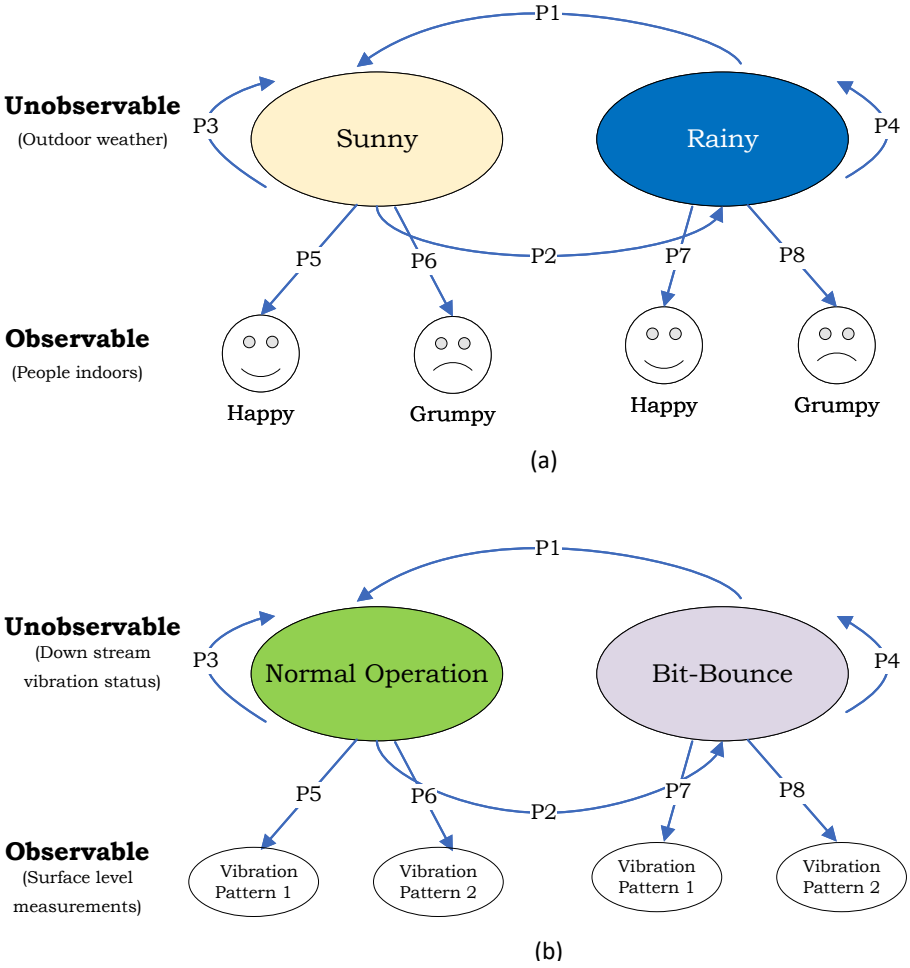

Figure 6.3: Hidden Markov Model (HMM)

is proposed to be used to detect the hidden states of the drillstring. For example, as illustrated in Figure 6.3b, the hidden states may be 'Normal Operation' and 'Bit Bounce' while the observable incidents are two different vibration patterns that do not carry a direct meaning. If the user can determine the probabilities $P1$ through $P8$, the HMM can identify the most probable transition in states according to the changes in vibration patterns observable from the ground level. This is done using the Viterbi Algorithm. It is a dynamic programming algorithm for finding the most likely sequence of hidden states (Viterbi Path) that results in a sequence of observed

events, especially in the context of Markov information sources and HMMs [31]. The concept illustrated in Figure 6.3 is used in the current study in classifying all three vibration conditions (bit bounce, stick-slip, and whirling) and their respective severity levels.

The user can train the HMM with different known vibration patterns for known actual states downhole. This training part will be facilitated by the validated bond graph model [21, 32, 33] as shown in Section 6.6.

6.3.3 Fatigue life estimation approach

SalomeMeca™ [34] is used to estimate MNV loading fatigue damage. Geometry, Mesh, CodeAster, and ParaVis are the software that serve 3D modelling, meshing, solving, and post processing of finite element models. Geometry module facilitates the development of 3D models and defining geometrical entities that support the meshing process in the Mesh module. Mesh module provides enhanced flexibility in meshing by providing better control of the meshing parameters. The solver used is CodeAster™ which facilitates the definition of materials, load assignments, specifying boundary conditions, fatigue life estimation, and numerical solving. Finally, ParaVis™ [35] was used to post-process the results generated by CodeAster™.

6.4 Physical system

This section applies the proposed methodology on a laboratory-scale apparatus as proof of concept. The main intention here is to showcase that training data for a machine learning algorithm, in this case for a slender vibrating structure, can be generated using a dynamic simulation model. This approach is useful when it is not feasible to generate reliable data from the physical structure in cases such as the

down-hole vibration of a drillstring.

6.4.1 Apparatus design

As the initial step, the apparatus was designed as illustrated in Figures 6.4 and 6.5. Further details of the design and CAD models can be accessed through the author's online repository. The drill bit consists of a flat bottom with a discontinuous cam profile that meshes with a similar profile on the base (hole bottom) as shown in Figure 6.6. Clockwise rotation of the bit will cause axial impacts resembling bit bounce vibration. When rotated in the opposite direction, this 'chatter mechanism' locks and the flexible coupling undergoes high torsional deformation and axial shortening, lifts the drill bit and suddenly releases it from the hole bottom. This motion resembles the stick-slip type of vibration. Further, the flexible coupling provides damping in the drillstring.

The platform, where the motor is mounted, can be moved vertically up or down using threaded rods and lock nuts. This facilitates axial thrust control, mimicking the WOB of a drillstring. Therefore, the apparatus can also be operated without the chatter mechanism and the flexible coupling to get stick-slip. The flexible coupling approach was used to get a more distinct stick-slip motion. With the addition of the WOB, the flexible coupling tends to move away from the central axis, causing a mass imbalance. This promotes the forward whirling action of the rotating string. Further, rubber skins attached to the flexible coupling holder create an increased friction force between the wall and the drillstring, which leads to backward whirling. Figure 6.7a depicts the fabricated apparatus ready for data acquisition, and Figure 6.7b illustrates the bond graph simulation's 3D visualization.

6.4.2 Instrumentation and data acquisition

The physical apparatus was instrumented to gather measurements that are typically available on the rig floor during drilling. The vibration of the platform, motor current

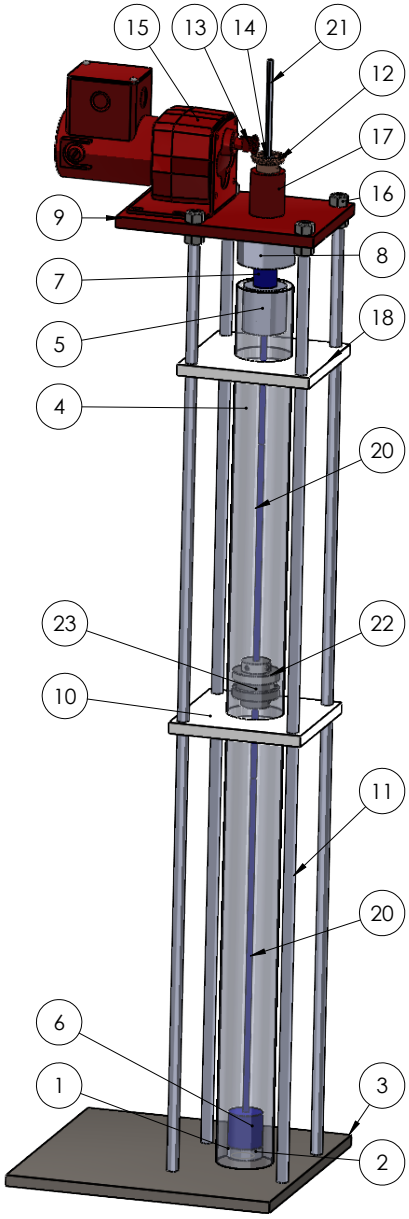

ITEM NO.	PART NUMBER
1	Base_pit
2	Drillbit_Chatter_1
3	Base
4	Cover
5	Bush_Bearing_1
6	Drillbit_Chatter_2
7	Rotary_Table
8	Bush_Bearing_2
9	Platform
10	Stiffner_1
11	Threaded_rod
12	Bevel_Gear
13	Bevel_Pinion
14	Bushing
15	Gear Motor_DC
16	Lock Nut
17	Collar
18	Stiffner_2
19	Spring (Hidden)
20	Drillstring_bottom
21	Drillstring_Middle
22	Flexible_Coupling
23	Flexible_Material

Figure 6.4: Components

fluctuation, and rotational speed fluctuation with lateral vibration of the rotating table are assumed to have a correlation with the downhole vibration conditions. These measurements must be acquired as a time series to feed the machine learning algorithm as testing data.

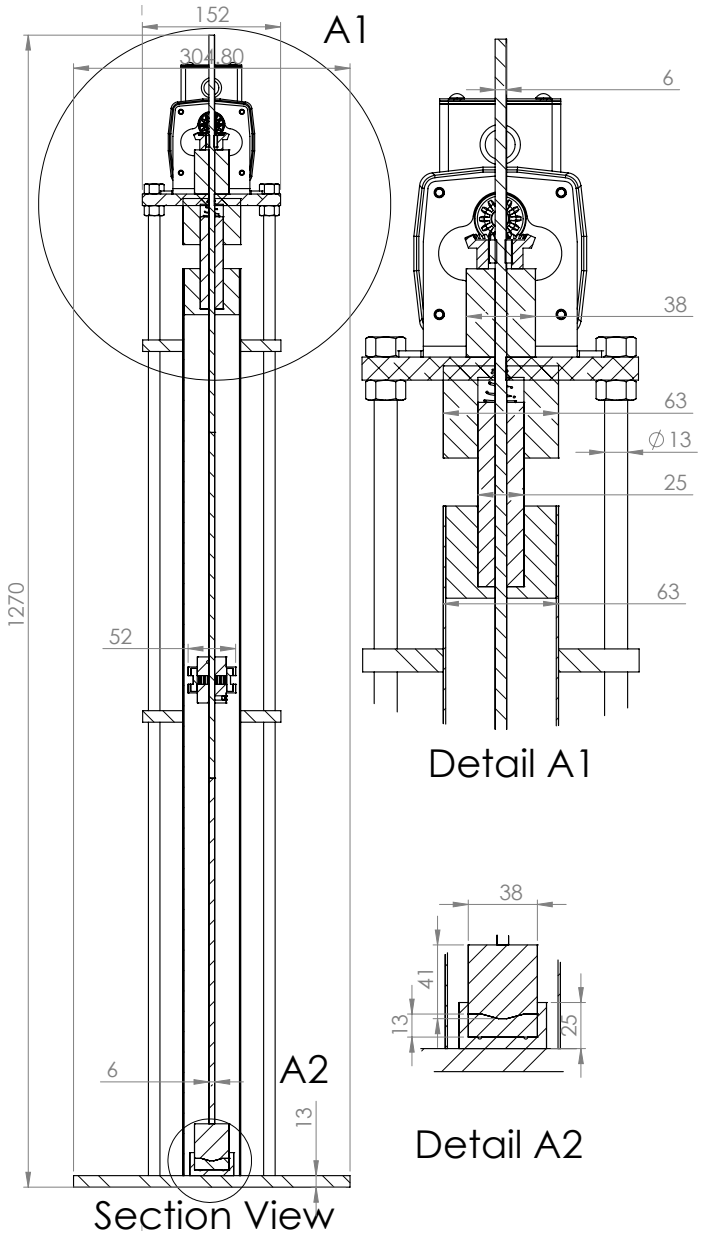

Figure 6.5: Vibration simulator dimensions (Unit: mm)

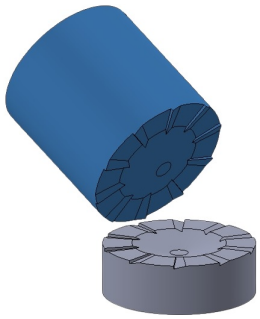

(a) "Chatter" mechanism

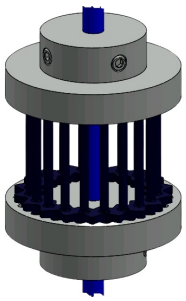

(b) Flexible coupling

Figure 6.6: The construction of key components

The vibration of the platform was acquired using a Kistler™ K-Shear general-purpose accelerometer. The angular speed fluctuation of the Rotating Table was captured using an AccuRange 200™ Laser Measurement Sensor and an optical encoder. The accuracies and ranges of the sensors used are presented in Table 6.1. The voltage across a resistor in series with the gear motor is directly proportional to

Table 6.1: Specifications of the sensors used

Sensor Type	**Make**	**Specifications**
Accelerometer	Kistler™ K-Shear	100 g (Max range)
Accelerometer	Kistler™ K-Shear	500 g (Max range)
Displacement Sensor	AccuRange™ 200	50. 8 mm (Range) 50.8 µm (Linearity)

the current demand fluctuation of the motor. Based on this assumption, the motor current fluctuation was measured as the third variable. National Instruments™ (NI) USB-6008 data logger, and LabVIEW™ software were used for data acquisition using these three channels. The LabVIEW™ program used is shown in Figure 6.8. The data acquired is presented in Section 6.8.

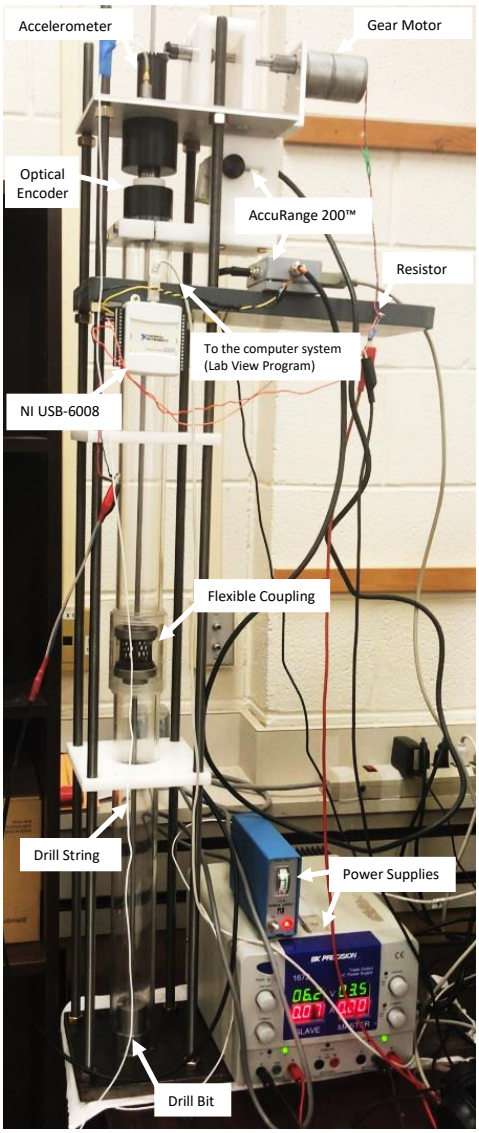

(a) Drillstring vibration simulator apparatus

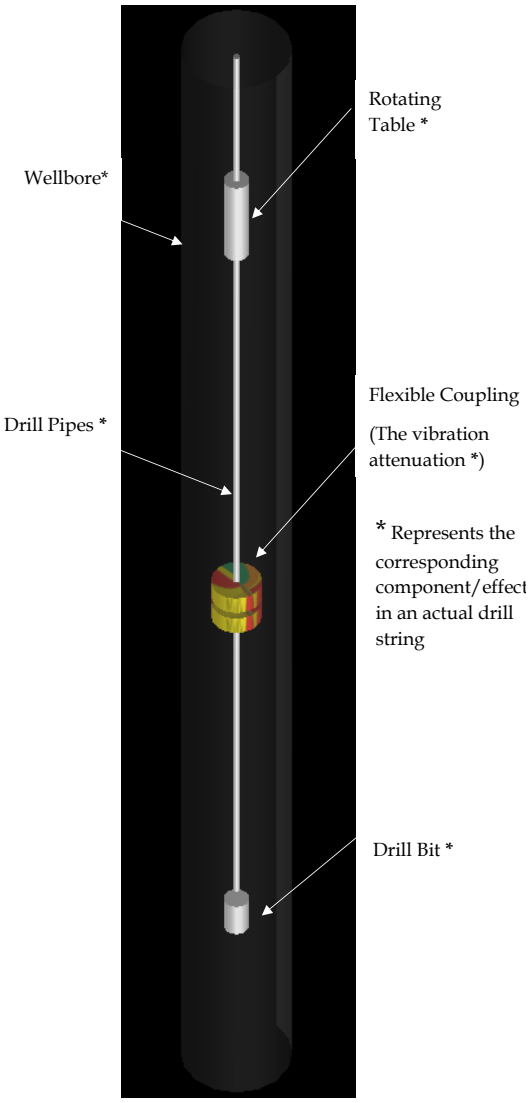

(b) The 3D visualization of the bond graph simulation

Figure 6.7: Apparatus and its bond graph simulation

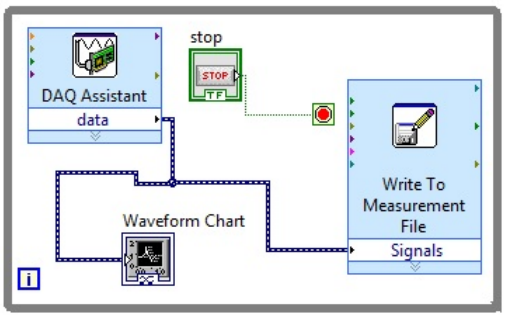

Figure 6.8: The LabVIEW™ program for data acquisition

6.5 Development of the simulation model

6.5.1 Lumped segment submodels and connections

The bond graph rigid body submodel used to simulate the actual drillstring is shown in Figure 6.9a. The corresponding points of A, B, and G indicated in Figure 6.9a are depicted in Figure 6.9a with a total of nine elements used, successfully capturing the first two natural frequencies of the various vibration types. In Figure 6.9a, One Junctions (1) represent velocity nodes where efforts (i.e. forces and torques) sum to zero and Zero Junctions (0) represent effort nodes that enforce velocity constraint equations. For example, the circled 0 junction, with the directed power bonds, enforces the relative velocity equation $v_a = v_G + v_{A|G}$, in vector form, where the relative velocity term is generated by a cross product of the relative position vector and angular velocity. The "R01" submodels are coordinate transforms. The developed bond graph can be reconfigured and customized to simulate a given structure by conveniently modifying the number of segments and (or) by including or suppressing certain degrees of freedom. The stiffness values can be determined following the procedure presented in [36].

The friction effects can be modelled by coding the friction model shown in Figure

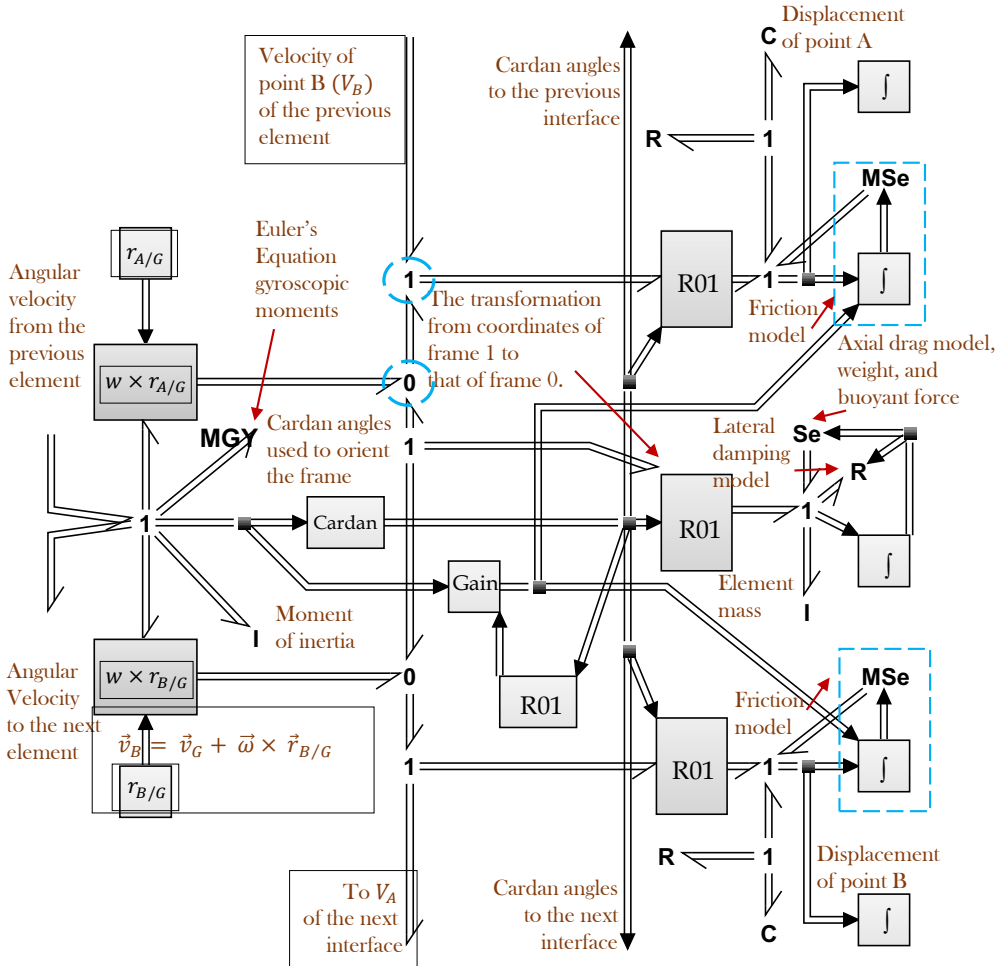

(a) Bond graph element with fluid damping and frictional models

(b) Successive multibody segments

Figure 6.9: The construction of a bond graph element

6.9 with the constitutive law of the modeler's choice. In this paper, a model presented in [37] is used, which is illustrated in Figure 6.10. Sample models are available for potential users and can be accessed through the online repository. The Stribeck friction, denoted as F_S, displays a negative slope when velocities are low. Meanwhile,

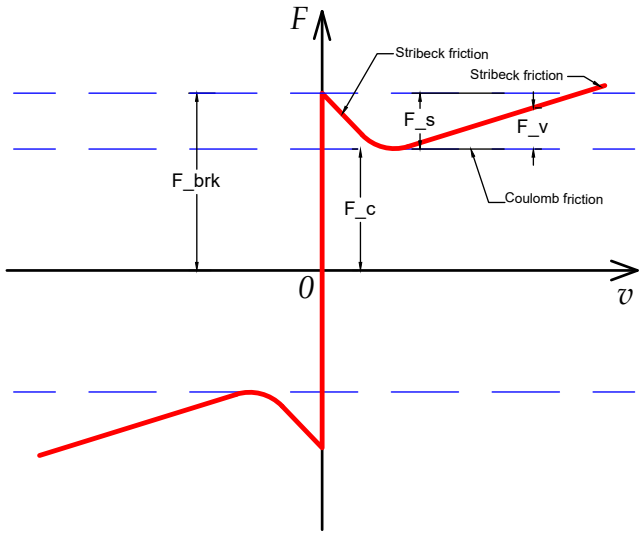

Figure 6.10: The friction model used in the bond graph

the Coulomb friction, F_C, produces a constant force at all velocities, and the viscous friction, F_V, resists motion with a force that is directly proportional to the relative velocity. The sum of the Coulomb and Stribeck frictions in the vicinity of zero velocity is commonly known as breakaway friction, F_{brk}. The friction can be estimated using the following equations:

$$F = \sqrt{2e}(F_{brk} - F_C) \cdot \exp(-\left(\frac{v}{v_{St}}\right)^2) \cdot \frac{v}{v_{St}} + F_C \cdot \tanh\left(\frac{v}{v_{Coul}}\right) + f_v \tag{6.1}$$

$$v_{St} = v_{brk}\sqrt{2} \tag{6.2}$$

$$v_{Coul} = \frac{v_{brk}}{10} \tag{6.3}$$

$$v = v_R - v_C \tag{6.4}$$

where F is friction force, F_C is Coulomb friction, F_{brk} is breakaway friction, v_{brk} is breakaway friction velocity, v_{St} is Stribeck velocity threshold, v_{Coul} is Coulomb velocity threshold, v_R and v_C are absolute velocities of the two bodies in contact, v is relative velocity, and f is viscous friction coefficient.

6.5.2 Flexible coupling modelling

The flexible coupling plays a major role in transferring the torque to the drill bit while allowing significant torsional deflection, creating a shortening effect that couples torsional and axial motion, and working as a vibration attenuator. Its nonlinear behaviour was characterized through a simple experiment. The shortening effect and the torsion with the increasing angle of twist θ are presented in Figure 6.11 and their models are presented in Equations 6.5 and 6.6 respectively. The axial shortening c (m/rad) and reaction torque τ (Nm/rad) are given by

$$c = 0.0013\ \theta^3 + 0.0038\ \theta^2 + 0.0005\ \theta + 0.00005 \tag{6.5}$$

$$\tau = -0.1342\ \theta^3 + 0.3088\ \theta^2 + 0.0699\ \theta - 0.0049 \tag{6.6}$$

where θ (rad) is the angle of twist. Equation 6.5 was time-differentiated and coded into a Modulated Source of Flow (MSf), and Equation 6.6 was coded into a modulated torsional bending stiffness C element as shown in Figure 6.12. Figure 6.12 depicts an interface model that connects adjacent rigid body segments by computing relative velocities of shear, axial, bending, and torsional springs. Interface elements other than the one at the flexible coupling are the same, except they do not have a modulated torsional stiffness or MSf with axial shortening effect. The interface models consist of four modulated transformers (MTF). Transformer, or TF, elements model a power

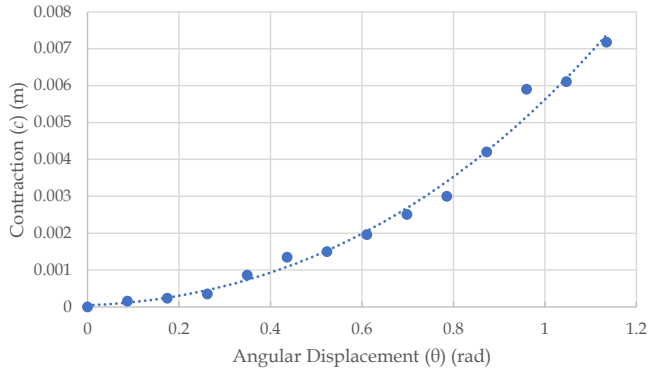

(a) Shortening effect vs angular twist

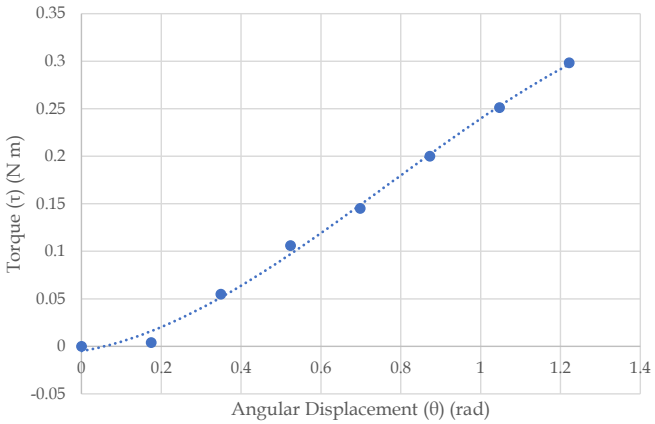

(b) Torque vs angular twist

Figure 6.11: Characterization of the flexible coupling

conserving transformation wherein effort variables are related to each other by a parameter, and flow variables are related to each other by the same parameter. For example, meshing gears would be modelled as a TF, with input and output torque and angular velocities related by the same gear ratio. An MTF has a varying parameter that is provided by a modulating signal. The MTFs in the interface element multiply velocity vectors in the frame of one body by a rotation matrix, to transform the velocity to the inertial frame. The next MTF transforms the velocity from inertial to the frame of the adjacent body. This allows a calculation of velocity of point B on one body relative to point A on the adjacent body, by subtracting two vectors in the same frame. The C elements (with parallel damping elements R) integrate the

relative velocity to get relative displacement components (translational or angular, as appropriate), which are multiplied by the spring stiffnesses to get internal efforts. These efforts maintain the shape of the rod, while creating stresses used in later fatigue analysis. The bond graph model can simulate bit bounce, stick-slip, and whirling vibrations. The simulated data was stored as comma-separated values (CSV) files for later use as training data for the machine learning algorithm.

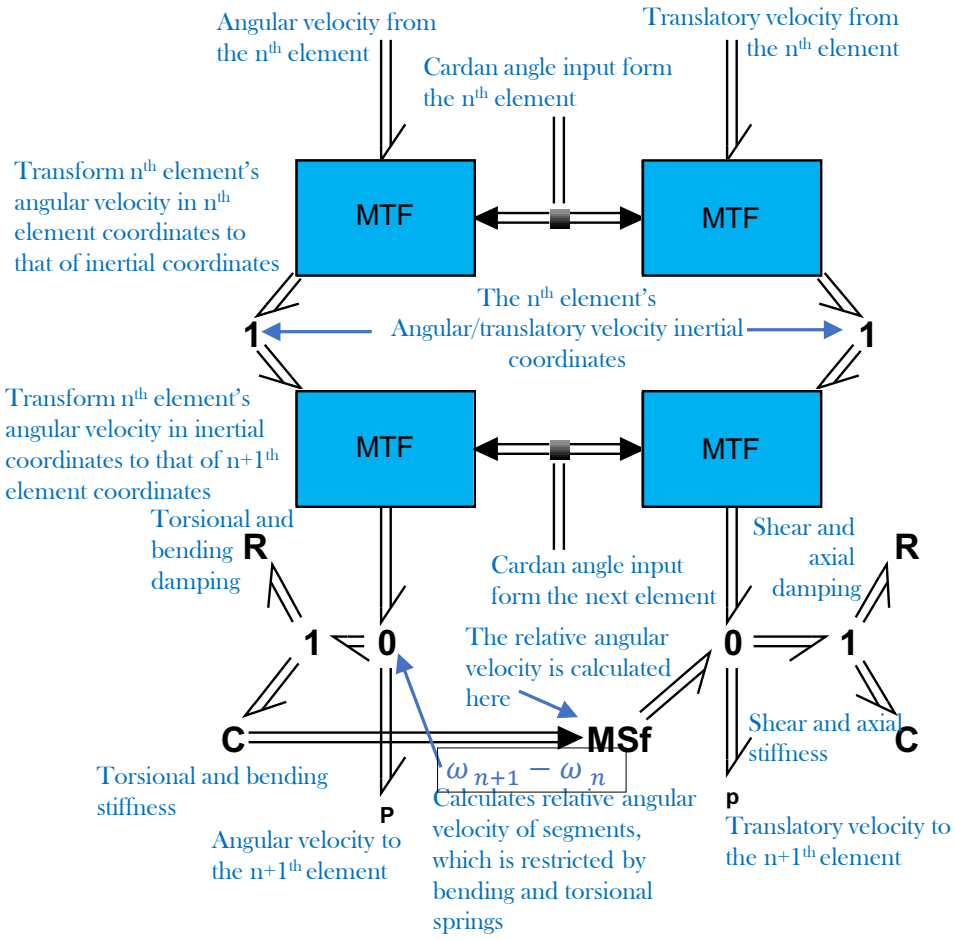

Figure 6.12: Bond graph model of the flexible coupling

6.6 Vibration classification

6.6.1 The machine learning algorithm

The HMM introduced in Section 6.3.2 is applied in the vibration status classification of the apparatus. As illustrated in Figure 6.2, the classification code developed based on the HMM algorithm can identify the type of vibration and its severity level. A brief description of the workflow of the code is presented in this section. The explanation is in line with the code presented in the author's online repository and in Appendix C.

The HMM introduced in Section 6.3.2 is applied to the vibration status classification of the apparatus. As illustrated in Figure 6.2, the classification code developed based on the HMM algorithm will identify the type of vibration and its severity level. A brief description of the workflow of the code is presented in this section. The associated code is presented in the author's online repository.

This code is solely based on the open-source HMM toolbox presented in [20]. The entire code consists of ten sections. The first nine sections are to train the algorithm for the nine different vibration conditions illustrated in Figure 6.2. The tenth section of the code is responsible for classifying the incoming data strings to the relevant 'basket'.

The simulations were configured to generate training data for the nine vibration conditions. The experimental apparatus was then used to create the corresponding physical conditions for actual measurement and application of the machine learning algorithm. The testing data for bit bounce and stick-slip vibrations were taken for one amplitude level (medium) and then scaled to get the upper and lower extremes of vibration amplitudes. For whirling, the readings were taken for three different am-

plitude levels because the number of well-bore interactions is the characteristic behaviour of this type of vibration, and is different at different amplitude levels. The motor current or the angular speed does not show a considerable fluctuation for this type of vibration. It should be highlighted that the angular speed at the surface level was not giving a considerable fluctuation for different downhole vibrations of the apparatus used. This is because of the softness of the flexible coupling. Therefore only the axial vibration and the motor current fluctuation contributed significantly to the classification process, which was sufficient to distinguish the nine vibration conditions.

Both training and testing data were scaled prior to use in the algorithm. In this way, all the training and testing data can be brought in to a common scale, so pattern recognition is convenient to perform. The training process follows an iterative approach which is not computationally extensive. In the algorithm, the user can control the number of different layers in the 3D matrix. For example, it may represent different data sets from similar drillstrings. Also, the user can specify the number of Gaussian mixtures and the number of hidden states. The algorithm assumes prior and transition probabilities and optimizes them using the Expectation Maximization (EM) algorithm. When the calculated log-likelihood becomes consistent, the iteration stops, and it is considered a trained algorithm for the given data set. Figure 6.13 is the training curve for the algorithm, for the case of bit bounce vibration with a medium amplitude level. Once the algorithm is trained using training data, it generates some parameters unique to the data set that is used to train.

The classification is done based on the log-likelihood value estimated for an incoming test data string from the physical apparatus. This data string consists of the three readings taken simultaneously from the accelerometer, displacement sensor, and the motor current reading. The displacement sensor captures the response of angular

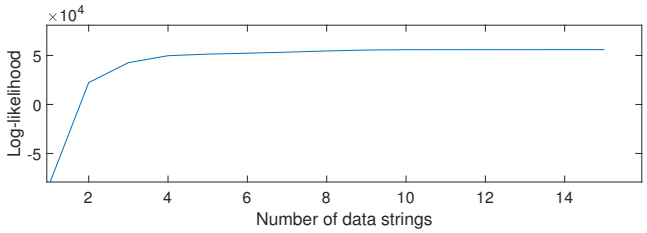

Figure 6.13: HMM training curve

velocity change using the optical encoder. The classifier takes all the data strings and computes the log-likelihood using the nine trained algorithms. In other words, it evaluates the similarity of the incoming test data strings to the respective states. The state which is corresponding to the maximum mean log-likelihood is presented as the vibration state of the drillstring during that time period. Once this is identified, the corresponding configuration of the bond graph can be selected to simulate and generate the relevant stress history for the fatigue life prognosis. These bond graph simulation stress histories can be made readily available as a database for a rapid fatigue prognosis.

6.7 Fatigue life prognosis

This section presents the extraction of the loading history from the bond graph, reconfigured after classification of physical system vibration, and the subsequent fatigue life prognosis procedure. The maximum stress concentration occurs at the joint between the drill bit and the drillstring due to the sharp transition of cross-section. This focused area was selected for further analysis.

The load fluctuation can be captured using the bond graph. Bending and shearing loads, each on two orthogonal planes, with axial and torsional loads, are the six load fluctuations that can be fed into SalomeMeca™ as time-series data. The

load fluctuations were extracted from the bond graph capacitive elements that represent the bending, torsional, shear, and axial compliances at the joint considered. The extracted load fluctuations for high amplitude whirling simulation are presented in Figure 6.18. Meshing was done using the Mesh Tool in SalomeMeca™ `Netgen 1D-2D-3d`, and the meshed geometry is shown in Figure 6.19a. For convenience in defining the aforementioned loadings, the 'loading horns' shown in Figure 6.19 were used. Figure 6.19 illustrates the fatigue prognosis result for high amplitude whirling vibration performed throughout 20 seconds while the angular speed of the drillstring is 100 rpm (10.4 rad/s). A complete MNV fatigue analysis workflow is available in [29] for further information.

As expected, the stresses acting on the steel moving parts of the apparatus in the laboratory are not severe, hence a substantial fatigue life remains. The fatigue life estimation methodology using SalomeMeca™ was verified by comparing it with the results of a simulation performed using a commercial code.

6.8 Results

6.8.1 Training and testing data sets

Figure 6.14 illustrates the comparison of the measurements: motor current and axial acceleration for stick-slip and bit bounce vibration conditions. Simulated data is presented in the left column, while experimental data is presented in the right column. Figures 6.14a, b, e, and f represent the responses for stick-slip (SS) vibration with medium amplitude (M), while Figures 6.14c, d, g, and h represent the responses for bit bounce (BB) vibration in the same amplitude level. Figure 6.15 depicts the responses for the whirling motion at low (L), medium (M), and high (H) amplitudes.

Different patterns of axial accelerations at different amplitude levels are evident. The abbreviations TR and TST stand for 'training' and 'testing', respectively. In both Figures 6.14 and 6.15, all the simulation results are scaled for comparison purposes while preserving the characteristic features.

6.8.2 Classification

The code does the classification based on the average log-likelihood value computed for a given sample testing data set. This scoring method selects the best candidate

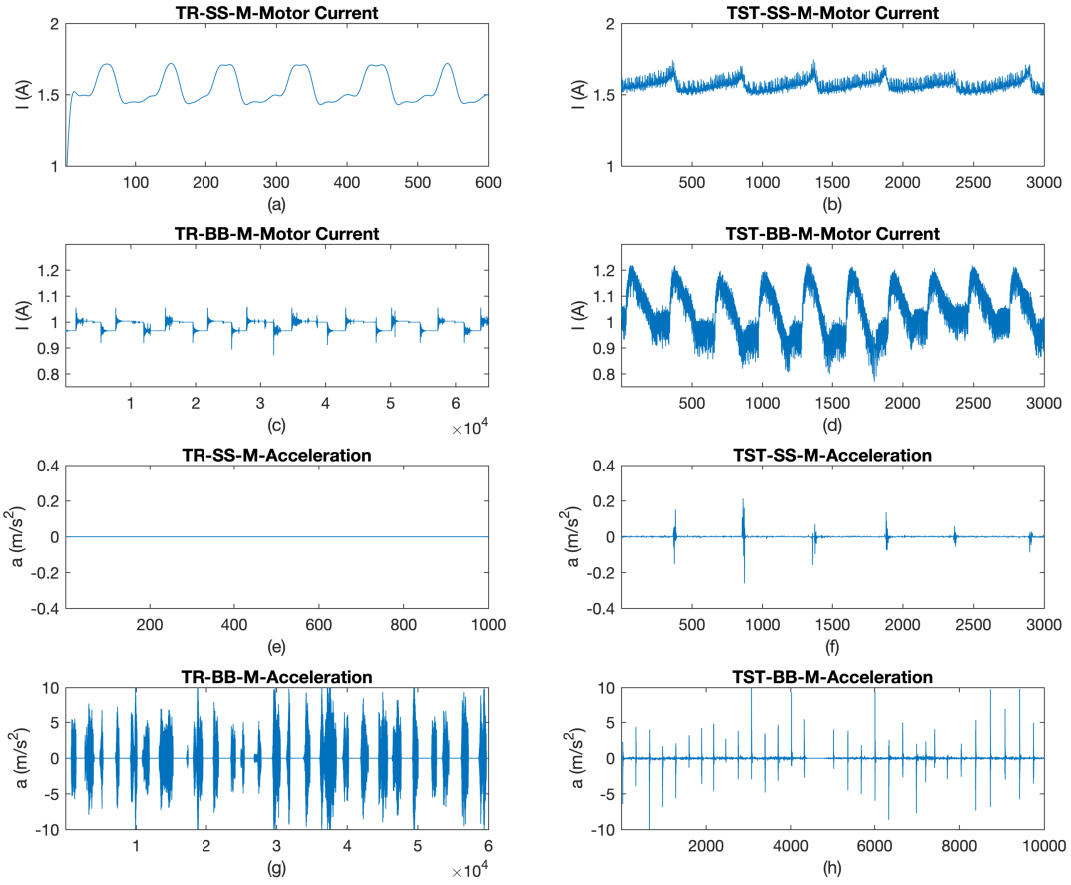

Figure 6.14: Training and testing data for stick-slip and bit bounce vibrations Note: The x axes represent the number of samples

among the trained algorithms. Figure 6.16 represents a sample classification of low amplitude whirling vibration. The algorithm has shortlisted SS-M, WH-H, WH-M and WH-L. The average log-likelihood for the given test data set has been calculated with the trained algorithm as shown in Table 6.2. The numerical values indicate that the average log-likelihood values are close for the three types of whirling and medium stick-slip vibration conditions, while the maximum among them is assigned to low

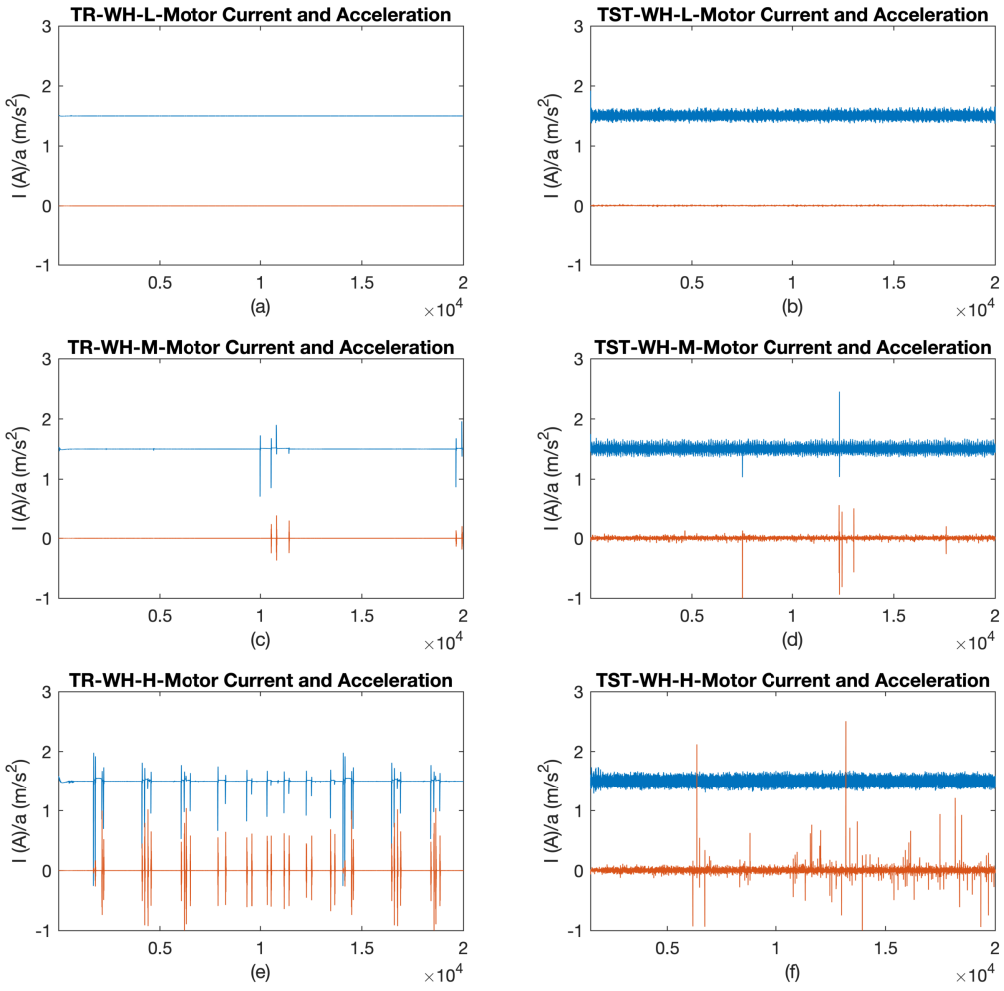

Figure 6.15: Training and testing data for whirling vibrations
Note: The x axes represent the number of samples. Motor current (I) and Acceleration (a) are shown in blue and orange respectively.

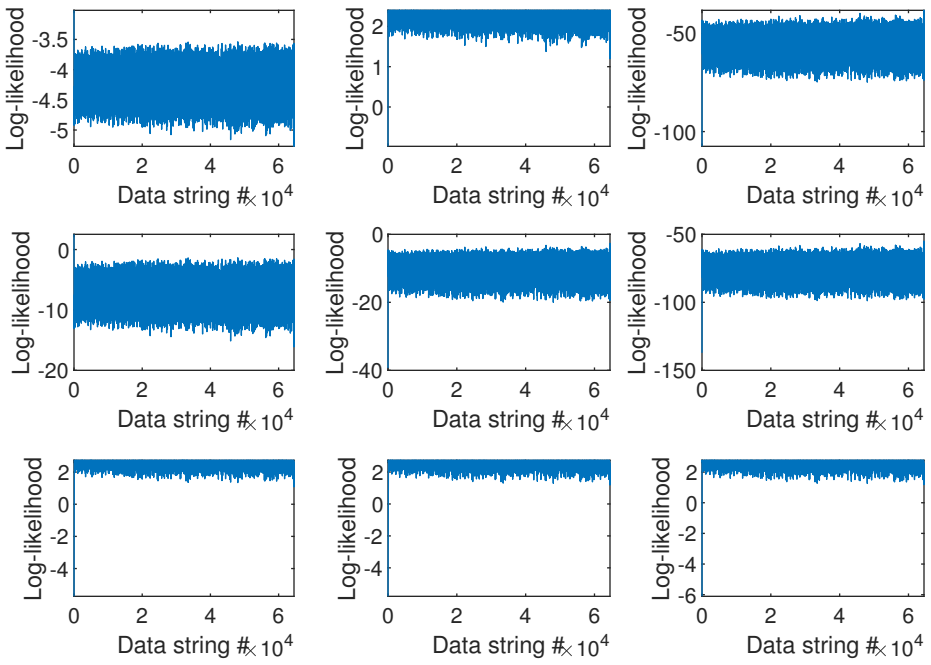

Figure 6.16: Log-likelihood estimation for each data string

whirling vibration.

As shown in the confusion matrices illustrated in Figures 6.17a and 6.17b, the classification algorithm successfully detects almost all the vibration conditions and the corresponding severity levels. Ten trials were performed for each of the nine vibration conditions, and the detected vibration by the classifier and the corresponding actual vibration conditions are compared. The numbers in the diagonal of the confusion matrix represent the number of successful outcomes out of ten trials. As indicated, the medium amplitude whirling sometimes gets misclassified as high or low whirling when no noise is added. When noise was added as a random number matrix with a maximum amplitude of 10% of the mean value of each reading, stick-slip and bit bounce were still accurately classified, while medium whirling at some trials was

Table 6.2: Average log-likelihood value calculation result

Vibration condition	**Average log-likelihood value**
High stick-slip	-4.2595
Medium stick-slip	2.2963
Low stick-slip	-55.4190
High bit bounce	-7.3777
Medium bit bounce	-10.0500
Low bit bounce	-75.746
High whirling	2.6238
Medium whirling	2.6293
Low whirling	2.6593

classified as medium stick-slip. These performance evaluations were done for the testing data illustrated in Figure 6.14.

6.8.3 Stress history extraction and fatigue life prognosis

Once the classification algorithm selects the most probable vibration condition, the bond graph simulation with the respective parameter set was run to extract the load fluctuations following the procedure mentioned in Section 6.7. The load history extracted from the element interface adjacent to the drill bit element is presented in Figure 6.18. The shear impulses give the highest fluctuation in response to the frictional impulses due to the collision with the wellbore. SalomeMeca™ can handle this complex combined loading situation to determine the remaining fatigue life. The uneven distribution of remaining fatigue life on the drillstring is evident in Figure 6.19, which is an indication of random loading and the superposition of the six different loading fluctuations. The remaining lifetime is near infinite due to the low stress fluctuations on the drill string. Nonetheless, it is clear that the digital twin framework is able to calculate the fatigue life incorporating complex geometric features and stress

concentrations, using the simulation-based estimation of loads.

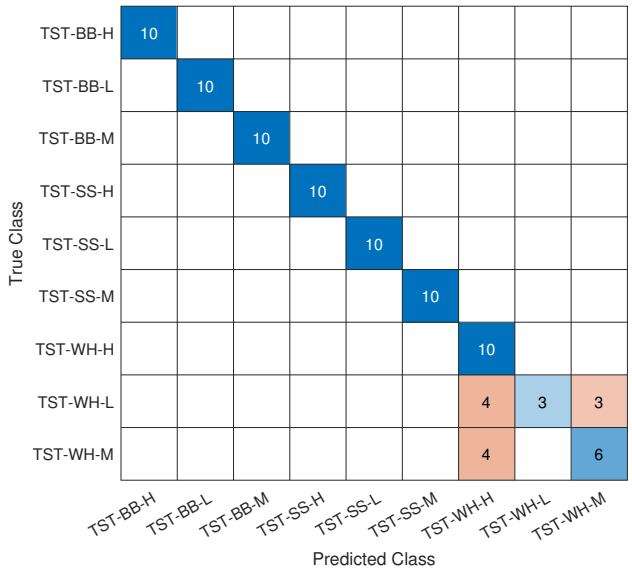

(a) The confusion matrix (noise 0%)

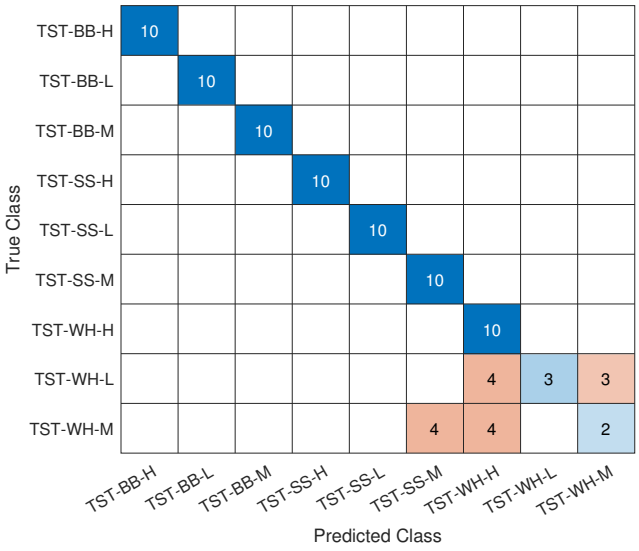

(b) The confusion matrix (noise 10%)

Figure 6.17: Performance evaluation

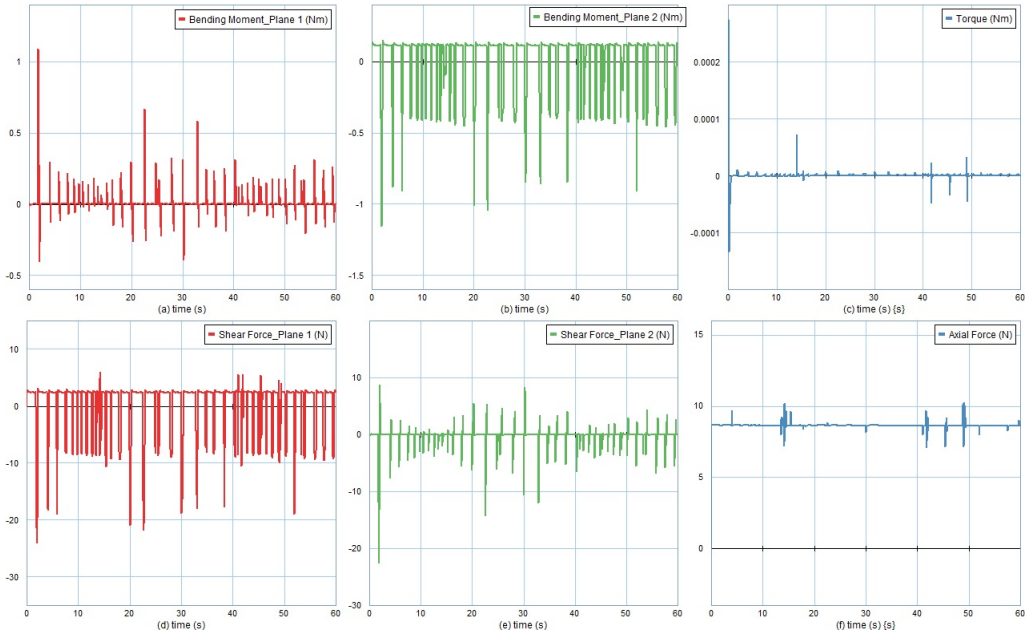

Figure 6.18: Load fluctuations at the drill bit-string connection

6.9 Discussion

The novel approach introduced in this study is capable of developing and customizing a digital twin. Successful implementation of the proposed framework has the potential to reduce reliance on measurement while drilling MWD for vibration problem detection. When the process is implemented for a full-scale drillstring, the data downloaded after tripping operations can be utilized to validate the overall digital twin. Improved real-time fatigue prognosis can increase the reliability of the drillstring, which will reduce the risk involved in the entire project. Drillstring failures have a major impact on the overall project cost, and more careful monitoring and proactive, corrective, and preventive actions will increase the drillstring's useful lifetime. Moreover, as mentioned in [38], rig downtime due to MWD tool failure carries enormous risks, especially in challenging environments. A digital twin can be imple-

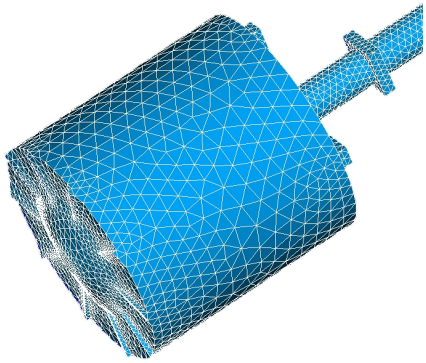

(a) Generated mesh

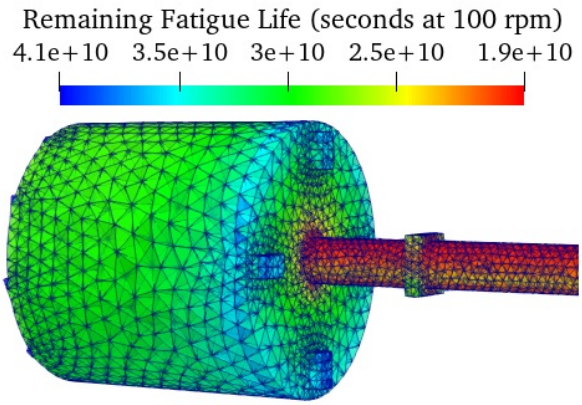

(b) Fatigue life estimation

Figure 6.19: Fatigue life prognosis at the drill bit using SalomeMeca™

mented as a secondary safety layer.

If a particular vibration is taking place in the lower part of the drillstring, the observations made at the surface level will depend on numerous factors such as the well depth, fluid flow speed, fluid rheology, speed of rotation, WOB, pipe geometry, drillstring orientation, type of drill bit, and the nature of the formation being drilled, to name a few. If these observations are only classified based on expert judgment and intuition, an inherent risk will be introduced due to potential human error. This motivates the implementation of a digital twin, using the framework of this paper, which has the capability to learn both through experience as well as running 'what-if' scenarios.

As with any measurement-based diagnostic approach, robustness of the machine learning algorithm training and predictions can be improved with a greater number of more accurate sensor inputs. A balance must be struck between accuracy of the prediction, and cost associated with increased sensing capability. In the current study, lateral acceleration of the rotary table could be added as an additional channel, incorporated into the real-time measurement data string. The use of a lower-powered motor may increase the torque fluctuations during stick-slip, thereby reducing classification uncertainty.

As described in [26] and [39], the bond graph of the digital twin could be expanded to include the effects of the drilling fluid. More experimentation could give a more nonlinear contact model for 'bit-rock' interaction and wellbore collisions.

When the digital twin is implemented for a particular drillstring, the data logged during tripping operations can be utilized to validate the overall digital twin as real-world data can be acquired with less complexity compared with deep wells. Finer adjustments to the digital twin can be made during this period which will be beneficial in the long run. In this way, confidence in the bond graph simulation can be improved as the machine learning algorithm solely depends on the data generated by the bond graph at higher depths.

There may be some practical limitations to using purely synthetic data as the data is generated in a near-perfect environment. Real-world data acquired through instrumentation will carry numerous noise effects. This is somewhat indicated in the results presented in Figure 6.14. As mentioned previously, some sensor noise can be artificially introduced into the virtual measurements, without seriously compromising the prediction ability. Therefore, more work is required to quantify the confidence of the classification algorithm in the face of varying amounts of noise or sensor error.

Open questions remain about the potential for model updating when operating

conditions or the state of the system change. If for example sensor data showed a sudden change in amplitude or frequency content, this could be due to a previously-learned vibration condition, or to non-problematic changes such as a new rock formation. It could also be an artefact of sensor failure. In future, training will be expanded to include not only anticipated vibration patterns but also things like sensor faults and changes in the environment with which the system interacts.

6.10 Conclusions

The current study proposes a bond graph, finite element modelling, and machine learning-based digital twin development framework for oilwell drillstring fatigue life prognosis where direct stress measurements are almost impractical. To detect vibration problems in a physical system, a dynamic simulation model with virtual sensors was created and used to train a machine learning algorithm. The algorithm analyzed vibration measurements from the physical system and identified the type and intensity of vibration. The simulation model was then adjusted to reproduce the vibration and generate stress histories for fatigue life analysis in a finite element model. The concept was verified to be feasible in classifying the physical system's downstream vibrations based on the type and severity level through surface-level response monitoring. Finally, the study identifies and recommends potential improvements to make the framework applicable in real-world applications.

6.11 Acknowledgement

This work was financially supported by the Natural Sciences and Engineering Research Council (NSERC) of Canada and Memorial University of Newfoundland (MUN),

Canada. The authors thankfully acknowledge the continuous support provided by the Drilling Technology Laboratory (DTL) research group, the Intelligent Systems Laboratory, and the Mechanical Division of Technical Services at MUN, Canada.

References

[1] M. E. Cobern, "Downhole vibration monitoring & control system," tech. rep., APS Technology, Inc.(US), 2005.

[2] H. Mostaghimi, J. R. Pagtalunan, B. Moon, S. Kim, and S. S. Park, "Dynamic drill-string modeling for acoustic telemetry," *International Journal of Mechanical Sciences*, vol. 218, p. 107043, 2022.

[3] Z. Zhang, Y. Shen, W. Chen, J. Shi, W. Bonstaff, K. Tang, D. Smith, Y. Arevalo, B. Jeffryes, *et al.*, "Continuous high frequency measurement improves understanding of high frequency torsional oscillation in north america land drilling," in *SPE Annual Technical Conference and Exhibition*, pp. 01–15, Society of Petroleum Engineers, 2017.

[4] Y. Zha and S. Pham, "Monitoring downhole drilling vibrations using surface data through deep learning," in *SEG Technical Program Expanded Abstracts 2018*, pp. 2101–2105, Society of Exploration Geophysicists, 2018.

[5] T. R. Wanasinghe, L. Wroblewski, B. K. Petersen, R. G. Gosine, L. A. James, O. De Silva, G. K. I. Mann, and P. J. Warrian, "Digital twin for the oil and gas industry: Overview, research trends, opportunities, and challenges," *IEEE Access*, vol. 8, pp. 104175–104197, 2020.

[6] T. Ritto and F. Rochinha, "Digital twin, physics-based model, and machine

learning applied to damage detection in structures," *Mechanical Systems and Signal Processing*, vol. 155, p. 107614, 2021.

[7] M. G. Mayani, M. Svendsen, S. Oedegaard, *et al.*, "Drilling digital twin success stories the last 10 years," in *SPE Norway One Day Seminar*, pp. 01–13, Society of Petroleum Engineers, 2018.

[8] DAU, "Defense acquisition glossary," 04 2021. https://www.dau.edu/glossary(Accessed on 02/15/2023).

[9] Siemens, "Digital twin," 2022. https://www.plm.automation.siemens.com (Accessed on 02/15/2023).

[10] J. Domone, "Digital twin for life predictions in civil aerospace," *Atkins White Paper. Digital twin can potentially integrate all the data between previous generation vehicles and current vehicle concept in its digital model*, 2018.

[11] M. Samnejad, M. Gharib Shirangi, R. Ettehadi, *et al.*, "A digital twin of drilling fluids rheology for real-time rig operations," in *Offshore Technology Conference*, pp. 01–15, Offshore Technology Conference, 2020.

[12] M. Gholami Mayani, R. Rommetveit, S. I. Oedegaard, and M. Svendsen, "Drilling automated realtime monitoring using digital twin," vol. Day 2 Tue, November 13, 2018 of *Abu Dhabi International Petroleum Exhibition and Conference*, 11 2018. D021S030R004.

[13] V. Dubinsky, H. Henneuse, and M. Kirkman, "Surface monitoring of downhole vibrations: Russian, european, and american approaches," in *European Petroleum Conference*, Society of Petroleum Engineers, 1992.

[14] H. Rafezi and F. Hassani, "Drilling signals analysis for tricone bit condition monitoring," *International Journal of Mining Science and Technology*, vol. 31, no. 2, pp. 187–195, 2021.

[15] M. Klaic, Z. Murat, T. Staroveski, and D. Brezak, "Tool wear monitoring in rock drilling applications using vibration signals," *Wear*, vol. 408, pp. 222–227, 2018.

[16] R. Saadeldin, H. Gamal, S. Elkatatny, and A. Abdulraheem, "Intelligent model for predicting downhole vibrations using surface drilling data during horizontal drilling," *Journal of Energy Resources Technology*, vol. 144, no. 8, 2022.

[17] R. W. Spencer, "Detection of downhole vibrations using surface data from drilling rigs," Apr. 1 2014. US Patent 8,688,382.

[18] Datagen, "Synthetic data: The complete guide," 2022. https://datagen.tech (Accessed on 02/15/2023).

[19] S. Nikolenko, *Synthetic data for deep learning*, vol. 174. Springer, 2021.

[20] K. Murphy, "Hidden markov model (hmm) toolbox for matlab," 2005. https://www.cs.ubc.ca/ murphyk/Software/HMM/hmm.html (Accessed on 02/15/2023).

[21] M. Galagedarage Don and F. Khan, "Process fault prognosis using hidden markov model–bayesian networks hybrid model," *Industrial & Engineering Chemistry Research*, vol. 58, no. 27, pp. 12041–12053, 2019.

[22] P. Spanos, A. Chevallier, and N. Politis, "Nonlinear stochastic drill-string vibrations," *J. Vib. Acoust.*, vol. 124, no. 4, pp. 512–518, 2002.

[23] D. G. Rideout, A. Ghasemloonia, F. Arvani, and S. D. Butt, "An intuitive and efficient approach to integrated modelling and control of three-dimensional vibration in long shafts," *International Journal of Simulation and Process Modelling*, vol. 10, no. 2, pp. 163–178, 2015.

[24] A. Mukherjee, R. Karmakar, and A. K. Samantaray, *Bond graph in modeling, simulation and fault identification*. IK International New Delhi, 2006.

[25] D. C. Karnopp, D. L. Margolis, and R. C. Rosenberg, *System dynamics: modeling, simulation, and control of mechatronic systems*. John Wiley & Sons, 2012.

[26] M. Sarker *et al.*, *Modeling and simulation of vibration in deviated wells*. PhD thesis, Memorial University of Newfoundland, 2017.

[27] A. Ghasemloonia, G. Rideout, and S. Butt, "The effect of weight on bit on the contact behavior of drillstring and wellbore," in *Proceedings of the 2010 Spring Simulation Multiconference*, pp. 1–7, 2010.

[28] E. P. Njål Kjærnes Tengesdal, Christian Holden, "Component-based modeling and simulation of nonlinear drill-string dynamics," *Journal of Offshore Mechanics and Arctic Engineering*, vol. 144, 4 2022.

[29] M. Galagedarage Don and G. Rideout, "Fatigue life prognosis of an oil well drill string using 3d lumped segment bond graph and finite element models," 2023.

[30] D. W. Stroock, *An introduction to Markov processes*, vol. 230. Springer Science & Business Media, 2013.

[31] L. Rabiner and B. Juang, "An introduction to hidden markov models," *ieee assp magazine*, vol. 3, no. 1, pp. 4–16, 1986.

[32] M. G. Don and F. Khan, "Dynamic process fault detection and diagnosis based on a combined approach of hidden markov and bayesian network model," *Chemical Engineering Science*, vol. 201, pp. 82–96, 2019.

[33] M. Galagedarage Don and F. Khan, "Auxiliary codes for fault prognosis of tennessee eastman process using a hybrid model (cpl1. 0)," *SoftwareX*, vol. 10, p. 100309, 2019.

[34] CodeAster, "Salome-meca - codeaster (accessed on 02/15/2023)," 2023. https://code-aster.org.

[35] M. Siavelis, "Paraview med for windows to open codeaster results – codeaster for windows," 2023. https://code-aster-windows.com (Accessed on 02/15/2021).

[36] M. Galagedarage Don and G. Rideout, "Fatigue failure prognosis of an oil well drill string using a lumped segment bond graph model and finite element method," in *ICBGM'2021*, (San Diego, California USA), pp. 1–14, Society for Modeling & Simulation International (SCS), 2021.

[37] B. Armstrong and C. de Wit, "Canudas," friction modeling and compensation", the control handbook," 1995.

[38] *MWD Failure Rates Due to Drilling Dynamics*, vol. All Days of *SPE/IADC Drilling Conference and Exhibition*, 02 2010. https://doi.org/10.2118/127413-MS.

[39] M. Galagedarage Don and G. Rideout, "An experimentally-verified approach for enhancing fluid drag force simulation in vertical oilwell drill strings," *Mathematical and Computer Modelling of Dynamical Systems*, vol. 28, no. 1, pp. 197–228, 2022.

Chapter 7

Summary and Future Research

This section summarizes the outcomes of the overall project, which align with the main objectives and contributions presented in Chapter 1. The generalized digital twin development framework proposed through this study is illustrated in Figure 7.1. The framework can be employed to develop a digital twin of a vertical well drill string and any vibrating structure in general. The reader can follow the process in Figure 7.1 starting from the block *'physical system'*. Sections from 7.1 to 7.3 explain the important steps followed and the procedure to follow in developing a digital twin. Potential research initiatives are highlighted towards the end of the chapter.

7.1 Digital twin parameterization

As mentioned in Subsection 1.2.1, Objective 1 is primarily on parameterizing the backbone simulation of the digital twin framework.

Bond graph simulation of the drill string generates training data for the machine learning algorithm. Therefore, two pieces of information are required when adapting the digital twin framework illustrated in Figure 7.1 to a given application. As

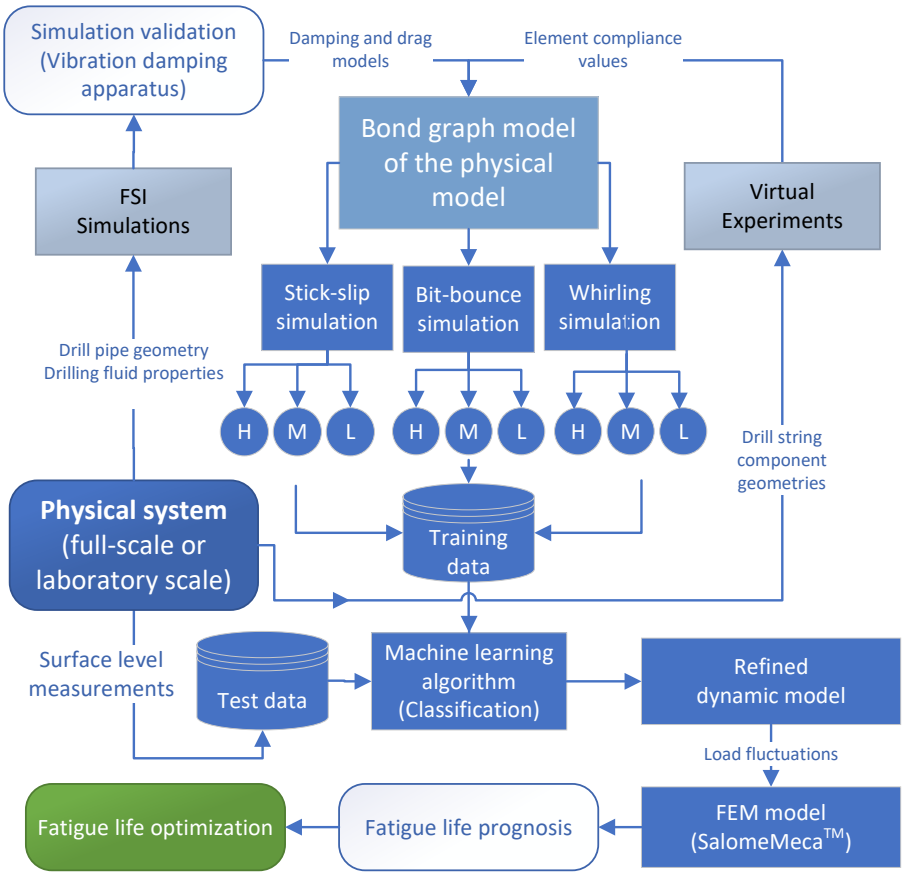

Figure 7.1: The generalized digital twin development framework

mentioned in Objective 1, they are 1.) the compliance values of the corresponding bond graph elements and 2.) the drilling fluid drag forces acting on the bond graph elements.

API 5D drill pipe and related structural components were selected for this study. Determining accurate stiffness values is not straightforward in both analytical and experimental approaches. Therefore, an FEM simulations-based methodology was introduced and applied to determine the compliance values for an API 5D drill pipe, a collar, and a stabilizer. The core of the methodology involves virtual experiments using finite element models and precision mapping of the results using drafting soft-

ware. As a verification of the methodology, it was applied to a tubular beam and compared with the analytical results for static and dynamic behaviour. The developed methodology is an efficient and accurate alternative to theoretical calculations with approximations and expensive experimental evaluation. These finding are presented in Chapters 4 and 5.

The second part of Objective 1, presented in Chapter 3, was to develop a methodology to determine the lateral and axial drag forces and apply the methodology to model the drag forces on an API 5D drill pipe BG element. The drill pipe geometry and the rheology of the drilling mud were considered in developing these models. An FSI simulations-based approach was taken with Design of Experiments, and the simulation was validated using a laboratory-scale experimental setup designed and fabricated in-house. The bond graph with drag force models implemented proved that the fluid damping effect should no longer be neglected as done in the literature and has a considerable effect on the drill string vibration and hence the failure due to fatigue.

7.2 Enabling the digital twin to capture vibrations in 3D space and equip with tools for fatigue prognosis

The developments represented by the block *'Bondgraph model of the physical twin'* of Figure 7.1 are presented in Chapter 5. They enable the digital twin framework to capture vibrations in 3D space. Although the 2D bond graph introduced in Chapter 4 is efficient in simulating bending vibrations, it omits the torsional and whirling vibrations, which are highly contributing factors to a fatigue failure of a drill string. This

also enables the simulation of stick-slip, bit-bounce, and forward-whirling vibrations with a comparatively low requirement of computation power.

Fatigue failure prognosis using the MNV approach is another major improvement introduced to the digital twin framework presented in Chapter 5. SalomeMeca™ was used and a detailed description of the workflow is presented for the benefit of future researchers.

7.3 Enabling the digital twin to detect and evaluate downhole vibrations using surface level measurements

Recently, a number of initiatives have been made to monitor drill string vibration behaviour from the surface. However, none of the research has employed a digital twin method to separate out various vibration types and their intensities, followed by an MNV fatigue study. The centre blocks of Figure 7.1 all the way to the block *'Fatigue life prognosis'* represent this value addition to the digital twin framework.

A bond graph, FEM, and machine learning-based digital twin was proposed for predicting the life of an oil well drill string. The proposed framework was implemented on a lab-scale apparatus, and the viability of the idea was demonstrated. The apparatus was designed and manufactured in-house. Surface level responses for down hole vibrations were captured using an accelerometer, an optical sensor, and a voltage measurement. They were used to measure the vertical acceleration, the angular speed, and the motor torque respectively. The identification of the characteristic responses related to downhole vibrations and the appropriate selection of the sensors to capture them were identified as key steps of the process. The machine learning

algorithm was trained using bond graph simulation-generated training data which is one of the unique features of this research. The testing data which are coming from the measurements were used by the machine learning algorithm to predict the downhole vibrations along with its severity.

7.4 Demonstrating the ability of the framework to be used as an optimization tool

Using the developed methodology, a fatigue life optimization of drill collars of a vertical drill string is presented in Chapter 5. The BHA of a vertical-well drill string was examined for maximum fatigue damage considering the location of two stabilizers by employing a 3D bond graph simulation and finite element MNV fatigue simulation using SalomeMeca™. It was found that the maximum fatigue damage of drill collars is principally controlled by the distance $D1$ from the drill bit to Stabilizer 1 in the scenario considered. This methodology has the potential to be used in minimizing the fatigue damage due to structural vibrations.

7.5 Further work

While this study achieved all the objectives listed in Chapter 1, it opens up several opportunities to conduct further research.

Only API 5D drill pipes were used in developing the damping and axial drag models that are described in Chapter 3. Further research can be done to estimate the damping effect on drill pipes with different geometries without completely re-deriving the models. In other words, the drill pipe diameter can be taken as one variable in addition to the five variables considered. This will be highly beneficial to the

community who are working with cascaded models to simulate fluid conveying pipe vibrations in an annular space. Dimensional analysis (DA) coupled with DOE can be utilized to reduce the number of experiments drastically while maintaining accuracy. Further, in addition to the validation of the FSI simulation, a complete experimental results-based model can be developed based on the similitude approach.

The experimental findings discussed in Chapter 3 offer some unique characteristics of a fluid-carrying pipe vibration damping. As demonstrated in Figures 3.21 and 3.14, respectively, the form of the damping curve with increasing velocity suggests a typical shape for both Newtonian and non-Newtonian fluids, which should be explored further. A vital contribution will also come from exploring the effect of different-sized rock cuttings on drill string damping. The effect of air bubbles is another important aspect that has never been studied. After enriching the damping models with the aforementioned improvements, the damping and axial drag models may be applied to a directional well bond graph model to further study the nature of vibrations.

The present study exclusively concentrates on optimizing fatigue life through strategic placement of stabilizers within drill collars. However, other factors may influence fatigue life, such as WOB and rotary speed of the drill string. A more comprehensive study incorporating these factors, followed by a DOE procedure and necessary fatigue life estimations, can be undertaken. Additionally, it would be intriguing to investigate the impact of the varying total length of the drill string and the rheological properties of the drilling fluid on fatigue damage by incorporating them in the design of experiments.

The fatigue prognosis does not yet incorporate the physical and chemical composition of the downhole environment, nor the washouts resulting from contact with the wellbore. However, SalomeMeca™ software has all the necessary capabilities for such advancements. This will create several opportunities for further research to improve

and develop the existing work into a commercially viable product. The entire process, including sensor configuration, classification, and fatigue failure prognosis, can be further refined and integrated into a single standalone software package. The data set produced by the bond graph for machine learning algorithm training and fatigue failure forecasting can be made easily accessible for fast processing and use in future research and industrial applications.

There is a lot of potential to increase the precision of the suggested digital twin framework with a deeper understanding of the hoist and rotary motor behaviours of a drilling rig. To mimic a more exact response of the motors to various downhole vibrations, a rigorous motor simulation is necessary. A comprehensive motor simulation can be used to refine the rotary effort source in the bond graph to get more sophisticated responses of the motors for different types of vibrations that occur at the downhole. This can be supported by employing software such as ANSYS Maxwell® . The induction motors can be effectively simulated based on vendor details and/or by doing physical measurements. Through the case study presented in Chapter 6, it was understood that the motor current fluctuation can give characteristic surface level responses even with the existing bond graph motor model. Further fine tuning of the motor model will give rise to better performance of the machine learning algorithm even in a more complex combined vibration situation.

***

Appendix (A): Matlab® Code for fatigue life prognosis

Matlab code for fatigue prognosis

```matlab
%%%%%%%%%%%%%%%%%%%%%%%%%%%%%%%%%%%%%%
Fatigue Life Prognosis Matlab Code
%%%%%%%%%%%%%%%%%%%%%%%%%%%%%%%%%%%%%%
%Preprocessing and normalizing of Axial and Bending force/Moment variation
load('InitialData.mat');
A = Tim_1_Axi_2_Ben_3;% Time, Axial, and Bending in the columns respectively
Norm_Ben = A(1:8940,3);%/abs(max(A(1:8940,3))); % The Bending moment CAN BE made to be oscillating about 1 and -1.
                        %But the FEM analysis is for 1 N m so need not to do here

%%%%%%%%%%%%%%%%%%%%%Enter the VM stress of the point of interest here%%%%%%%%%%%%%%%%%%%%%%%%%%
prompt = 'Enter the maximum von Mises stress of the point of interest here? You can enter 5.7353E5 Pa as it is already found from the FEM Model for 1 N load: ';
VM = input (prompt); % Ave Equivalent von-mises from FEM model {Pa}
VM_Ben =  Norm_Ben*VM; %Fluctuation of VM stress with varying BM
%%
%Apply rainflow counting
C_Ben = rainflow(VM_Ben);
TT_Ben = array2table(C_Ben,'VariableNames',{'Count','Range','Mean','Start','End'});
rainflow(VM_Ben)
```

```
19
20 %%
21 %Definitions
22 SIG_a_Ben = 1/2*C_Ben(:,2); %sigma_a = range/2
23
24 SIG_m_Ben = 1/2*C_Ben(:,3); %sigma_m = mean/2
25 S_ut = 4.6E8; % material Property
26
27 %%
28 % determination of a and b
29 f= 0.9; %This is the Fatigue Strength
      factor which is almost equal to 0.9
30           %(Shiegle's book Figure 6-18. S_ut = 500 MPa = 72
                kpsi)
31 S_e_raw = S_ut/2; % Approximately, the endurance limit is
      half of the S_ut (Ref: Engineering Toolbox)
32 a1 = 1.58;%(Table 6.2 Shiegley's)
33 b1 = -0.085;
34 d= 88.9;% diameter in mm
35 d_e = 0.37*d; %effective size of a round corresponding to
      a nonrotating solid or hollow round. (Equation 6-24)
36 k_a = a1*S_ut^b1; %Equation 6-19
37 k_b = 1.51*d_e^(-0.157); % Equation 6-20
38 k_c = 1;% because only bending
39 k_d = 1; % Because S_T/S_RT is almost 1 according to table
       6-4
40 k_e = 1; % Reliability factor (This is an assumed value
      from Table 6-5)
41 k_f = 1; % Miscelaneous
42
43 S_e = k_a*k_b*k_c*k_d*k_e*k_f*S_e_raw;
44
45 a = (f*S_ut)^2/S_e;
46 b = (-1/3)*log10(f*S_ut/S_e);
47
48 %%
49 % determination of the equivalent fully reversed stress
      for each mean and
50 % range
51
52 S_f = []; % equivalent fully reversed stress. Here the
      Gerber Criteria is used.
```

```
for i = 1:size(SIG_a_Ben,1)
    if SIG_m_Ben(i,1) > 0
        S_f = [S_f; SIG_a_Ben(i,1)/(1-(SIG_m_Ben (i,1)/
           S_ut)^2)];
    else
        S_f = [S_f; S_e];
    end
end


%%
N =[];
for i = 1:size(S_f,1)
    N = [N; (S_f(i,1)/a)^(1/b)]; % Equation 6-16
end

format shortE

%%
% Damage calculation

Damage = [];
for i =1:size(N,1)
   Damage =  [Damage; C_Ben(i,1)./N(i,1)];
end

Damage_Percentage = sum(Damage)*100
Remaining_Time_hrs = (10/(Damage_Percentage/100))/3600
```

Matlab code for fatigue prognosis (Manual Calculation)

```
%%%%%%%%%%%%%%%%%%%%%%%%%%%%%%%%%%%%%%%%%%%%%%%%%%%
Fatigue Life Prognosis Manual Calculation
%%%%%%%%%%%%%%%%%%%%%%%%%%%%%%%%%%%%%%%%%%%%%%%%%%%

%Preprocessing and normalizing of Axial and Bending force/
   Moment variation
sine1 = dsp.SineWave(0.175E3,9);
sine1.SamplesPerFrame = 9000;
A = sine1();

Norm_Ben = A; % Sinusoidal data set

%%%%%%%%%%%%%%%%%%%%%%Enter the VM stress of the point of
```

```
   interest here%%%%%%%%%%%%%%%%%%%%%%%%%%%%
VM = 5.7353E5; % Ave Equivalent von-Mises from FEM model {
   Pa}
VM_Ben =  Norm_Ben*VM; %Fluctuation of VM stress with
   varying BM

plot (VM_Ben)
n = size(findpeaks(VM_Ben),1); % Number of cycles. Number
   of peaks equals to the number of cycles
%Definitions
SIG_a_Ben = (max(VM_Ben)-min(VM_Ben))/2; %sigma_a = range
   /2

SIG_m_Ben = 0; %sigma_m = mean/2

%%determination of the equivalent fully reversed stress
   for each mean and range
S_ut = 4.6E8;

%%determination of a and b
f= 0.9; %This is the Fatigue Strength
   factor which is almost equal to 0.9
        %(Shiegle's book Figure 6-18. S_ut = 500 MPa = 72
           kpsi)
S_e_gross = S_ut/2; % Approximately, the endurance limit
   is half of the S_ut (Ref: Engineering Toolbox)
a1 = 1.58;%(Table 6.2 Shiegley's)
b1 = -0.085;
d= 88.9;% diameter in mm
d_e = 0.37*d; %effective size of a round corresponding to
   a nonrotating solid or hollow round. (Equation 6-24)
k_a = a1*S_ut^b1; %Equation 6-19
k_b = 1.51*d_e^(-0.157); % Equation 6-20
k_c = 1;% because only bending
k_d = 1; % Because S_T/S_RT is almost 1 according to table
    6-4
k_e = 1; % Reliability factor (This is an assumed value
   from Table 6-5)
k_f = 1; % Miscelaneous
S_e = k_a*k_b*k_c*k_d*k_e*k_f*S_e_gross;
a = (f*S_ut)^2/S_e;
b = (-1/3)*log10(f*S_ut/S_e);
```

```
43
44
45 N = (SIG_a_Ben/a)^(1/b);
46
47 format shortE
48
49 %%Damage calculation
50
51    Damage =  n/N;
52
53 Damage_Percentage = Damage*100
54 %Remaining_Time_hrs = (10/(Damage_Percentage/100))/3600
55 Remaining_Time_hrs_1 = (N/n)*10/3600
```

Appendix (B): MNV loading fatigue prognosis code with SalomeMeca™

Note: with non-linear frictional contacts

```
DEBUT(LANG='FR')
mesh3 = LIRE_MAILLAGE(identifier='0:1',
FORMAT='MED',
UNITE=20)
mesh4 = LIRE_MAILLAGE(identifier='1:1',
FORMAT='MED',
UNITE=2)
mesh0 = ASSE_MAILLAGE(identifier='2:1',
MAILLAGE_1=mesh3,
MAILLAGE_2=mesh4,
OPERATION='SUPERPOSE')
mesh0 = MODI_MAILLAGE(identifier='3:1',
reuse=mesh0,
MAILLAGE=mesh0,
ORIE_PEAU=(_F(GROUP_MA_INTERNE=('pin', ),
GROUP_MA_PEAU=('Load', 'pt', 'pb')),
_F(GROUP_MA_INTERNE=('box', ),
GROUP_MA_PEAU=('Fix', 'bt', 'bp'))))
model = AFFE_MODELE(identifier='4:1',
AFFE=_F(MODELISATION='3D',
PHENOMENE='MECANIQUE',
TOUT='OUI'),
MAILLAGE=mesh0)
Steel = DEFI_MATERIAU(identifier='5:1',
ECRO_LINE=_F(D_SIGM_EPSI=1100000000.0,
SIGM_LIM=900000000.0,
SY=700000000.0),
ELAS=_F(E=210000000000.0,
```

```
NU=0.285,
RHO=7850.0),
FATIGUE=_F(A_BASQUIN=1457000000.0,
BETA_BASQUIN=-0.085),
RCCM=_F(SU=900000000.0))
fieldmat = AFFE_MATERIAU(identifier='6:1',
AFFE=_F(MATER=(Steel, ),
TOUT='OUI'),
MODELE=model)
loadf = DEFI_FONCTION(identifier='7:1',
NOM_PARA='INST',
PROL_DROITE='CONSTANT',
PROL_GAUCHE='EXCLU',
VALE=(0.0, 5.0, 0.25, 10.0, 0.5, 1.0, 0.75, 0.0, 1.0,
   10.0))
listr = DEFI_LIST_REEL(identifier='8:1',
DEBUT=0.0,
INTERVALLE=_F(JUSQU_A=1.0,
PAS=0.25))
ldf = AFFE_CHAR_MECA_F(identifier='9:1',
FORCE_FACE=_F(FX=loadf,
GROUP_MA=('Load', )),
MODELE=model)
load = AFFE_CHAR_MECA(identifier='10:1',
FACE_IMPO=(_F(DX=0.0,
DY=0.0,
DZ=0.0,
GROUP_MA=('Fix', )),
_F(DY=0.0,
DZ=0.0,
GROUP_MA=('Load', ))),
MODELE=model)
contact = DEFI_CONTACT(identifier='11:1',
FORMULATION='CONTINUE',
LISSAGE='OUI',
MODELE=model,
REAC_GEOM='SANS',
ZONE=(_F(ALGO_CONT='PENALISATION',
COEF_PENA_CONT=20000000000.0,
GROUP_MA_ESCL=('bp', ),
GROUP_MA_MAIT=('pb', )),
_F(ALGO_CONT='PENALISATION',
```

```
COEF_PENA_CONT=20000000000.0,
GROUP_MA_ESCL=('pt', ),
GROUP_MA_MAIT=('bt', ))))
resnonl = STAT_NON_LINE(identifier='12:1',
CHAM_MATER=fieldmat,
COMPORTEMENT=_F(DEFORMATION='GROT_GDEP'),
CONTACT=contact,
CONVERGENCE=_F(ITER_GLOB_MAXI=30,
RESI_GLOB_MAXI=0.0001,
RESI_GLOB_RELA=0.0001),
EXCIT=(_F(CHARGE=ldf),
_F(CHARGE=load)),
INCREMENT=_F(LIST_INST=listr),
MODELE=model,
NEWTON=_F(MATRICE='TANGENTE',
PREDICTION='TANGENTE'))
resnonl = CALC_CHAMP(identifier='13:1',
reuse=resnonl,
CRITERES=('SIEQ_ELGA', ),
RESULTAT=resnonl)
field = CALC_FATIGUE(identifier='14:1',
DOMMAGE='WOHLER',
HISTOIRE=_F(EQUI_GD='VMIS_SG',
RESULTAT=resnonl),
MATER=Steel,
OPTION='DOMA_ELGA_SIGM',
TYPE_CALCUL='CUMUL_DOMMAGE')
table = POST_FATIGUE(identifier='15:1',
COEF_MULT=_F(KT=2.0),
COMPTAGE='NATUREL',
CORR_SIGM_MOYE='GOODMAN',
CUMUL='LINEAIRE',
DOMMAGE='WOHLER',
HISTOIRE=_F(SIGM=loadf),
MATER=Steel)
IMPR_RESU(identifier='16:1',
FORMAT='MED',
RESU=_F(CHAM_GD=field),
UNITE=3,
VERSION_MED='4.0.0')
IMPR_TABLE(identifier='17:1',
FORMAT='TABLEAU',
```

```
TABLE=table,
UNITE=4)
IMPR_RESU(identifier='18:1',
RESU=_F(RESULTAT=resnonl),
UNITE=5)
FIN()
```

Appendix (C): Matlab® code for vibration classification

Note: Vibration type and severity classification

```
%%
%The Bond Graph Digital Twin generates training data (TD) to train the ML
%algorithm. The data is for Stick Slip (SS), Bit Bounce (BB), and Whirling (WH) and their
%3 levels high (H), medium (M) and low (L)
%%%%%%%%%%%%%%%%%%%%%%%%%%%%%%%%%%%%%%%% Stick-Slip (SS) %%%%%%%%%%%%%%%%%%%%%%%%%%%%
%% Training for High Stick-Slip (TR_SS_H)
addpath(genpath('C:\Users\HMMall')) %  b
data_1 = [TR_SS_H]';% Training Data High Stick-Slip
T_1 = size(data_1,2); % The number of observation sequences. In other words, How many data sample strings? or the number of raws
O_1 = size(data_1,1); % The number of sensor data in a given sequence i.e. Motor Current, Accelerometer, and ang speed or teh number of columns
nex_1 = 1; % the different layers of data in the 3D matrix. (May be the data from another similar process line)
M_1 = 2; %Number of mixtures of Gaussians
Q_1 = 4; % Number of hidden states.
left_right_1 = 0; %Left-right architecture of the HMM model, 'yes' or 'no'
prior0_1 = normalise(rand(Q_1,1));% Initial guess of state probabilities
transmat0_1 = mk_stochastic(rand(Q_1,Q_1));% Initial guess of transition probabilities
[mu0_1, Sigma0_1] = mixgauss_init(Q_1*M_1, reshape(data_1, [O_1 T_1*nex_1]), 'full');
mu0_1 = reshape(mu0_1, [O_1 Q_1 M_1]);
```

```
Sigma0_1 = reshape(Sigma0_1, [O_1 O_1 Q_1 M_1]);
mixmat0_1 = mk_stochastic(rand(Q_1,M_1));
%Finally, let us improve these parameter estimates using
   Expectation Maximization Algorithm.
[LL_1, prior1_1, transmat1_1, mu1_1, Sigma1_1, mixmat1_1]
   = b@x...
mhmm_em(data_1, prior0_1, transmat0_1, mu0_1, Sigma0_1,
   mixmat0_1, 'max_iter', 40);
%
plot (LL_1) % Plotting the improvement of the Log
   Likelihood after 5 iterations. the learning curve.
xlabel ('Number of data strings')
ylabel ('Log-likelihood')
%
disp('Log-likelihood becomes consistent. SS_H Trained!')
%
%% Training for Medium Stick-Slip (TR_SS_M)
addpath(genpath('C:\Users\HMMall'))
data_2 = [TR_SS_M]';% Training Data High Stick-Slip
T_2 = size(data_2,2); % The number of observation
   sequences. In other words, How many data sample
   strings? or the number of raws
O_2 = size(data_2,1); % The number of sensor data in a
   given sequence i.e. Motor Current, Accelerometer, and
   ang speed or teh number of columns
nex_2 = 1; % the different layers of data in the 3D matrix
   . (May be the data from another similar process line)
M_2 = 2; %Number of mixtures of Gaussians
Q_2 = 4; % Number of hidden states.
left_right_2 = 0; %Left-right architecture of the HMM
   model, 'yes' or 'no'
prior0_2 = normalise(rand(Q_2,1));% Initial guess of state
    probabilities
transmat0_2 = mk_stochastic(rand(Q_2,Q_2));% Initial guess
    of transition probabilities
[mu0_2, Sigma0_2] = mixgauss_init(Q_2*M_2, reshape(data_2,
    [O_2 T_2*nex_2]), 'full');
mu0_2 = reshape(mu0_2, [O_2 Q_2 M_2]);
Sigma0_2 = reshape(Sigma0_2, [O_2 O_2 Q_2 M_2]);
mixmat0_2 = mk_stochastic(rand(Q_2,M_2));
%Finally, let us improve these parameter estimates using
   Expectation Maximization Algorithm.
```

```
47 [LL_2, prior1_2, transmat1_2, mu1_2, Sigma1_2, mixmat1_2]
      = mhmm_em(data_2, prior0_2, transmat0_2, mu0_2,
      Sigma0_2, mixmat0_2, 'max_iter', 40);
48 %
49 plot (LL_2) % Plotting the improvement of the Log
      Likelihood after 5 iterations. the learning curve.
50 xlabel ('Number of data strings')
51 ylabel ('Log-likelihood')
52
53 disp('Log-likelihood becomes consistent. SS_M Trained!')
54 %% Training for Low Stick-Slip (TR_SS_L)
55 addpath(genpath('C:\Users\HMMall'))
56 data_3 = [TR_SS_L]';% Training Data Low Stick-Slip
57 T_3 = size(data_3,2); % The number of observation
      sequences. In other words, How many data sample
      strings? or the number of raws
58 O_3 = size(data_3,1); % The number of sensor data in a
      given sequence i.e. Motor Current, Accelerometer, and
      ang speed or teh number of columns
59 nex_3 = 1; % the different layers of data in the 3D matrix
      . (May be the data from another similar process line)
60 M_3 = 2; %Number of mixtures of Gaussians
61 Q_3 = 4; % Number of hidden states.
62 left_right_3 = 0; %Left-right architecture of the HMM
      model, 'yes' or 'no'
63 prior0_3 = normalise(rand(Q_3,1));% Initial guess of state
       probabilities
64 transmat0_3 = mk_stochastic(rand(Q_3,Q_3));% Initial guess
       of transition probabilities
65 [mu0_3, Sigma0_3] = mixgauss_init(Q_3*M_3, reshape(data_3,
       [O_3 T_3*nex_3]), 'full');
66 mu0_3 = reshape(mu0_3, [O_3 Q_3 M_3]);
67 Sigma0_3 = reshape(Sigma0_3, [O_3 O_3 Q_3 M_3]);
68 mixmat0_3 = mk_stochastic(rand(Q_3,M_3));
69 %Finally, let us improve these parameter estimates using
      Expectation Maximization Algorithm.
70 [LL_3, prior1_3, transmat1_3, mu1_3, Sigma1_3, mixmat1_3]
      = ...
71 mhmm_em(data_3, prior0_3, transmat0_3, mu0_3, Sigma0_3,
      mixmat0_3, 'max_iter', 40);
72 %
73 plot (LL_3) % Plotting the improvement of the Log
```

```
   Likelihood after 5 iterations. the learning curve.
xlabel ('Number of data strings')
ylabel ('Log-likelihood')

disp('Log-likelihood becomes consistent. SS_L Trained!')

%%%%%%%%%%%%%%%%%%%%%%%%%%%%%%%%%%%% Bit-Bounce (BB)
   %%%%%%%%%%%%%%%%%%%%%%%%%%

%% Training for High Bit Bounce (TR_BB_H)
addpath(genpath('C:\Users\HMMall'))
data_4 = [TR_BB_H]';% Training Data High Bit Bounce
T_4 = size(data_4,2); % The number of observation
   sequences. In other words, How many data sample
   strings? or the number of raws
O_4 = size(data_4,1); % The number of sensor data in a
   given sequence i.e. Motor Current, Accelerometer, and
   ang speed or teh number of columns
nex_4 = 1; % the different layers of data in the 3D matrix
   . (May be the data from another similar process line)
M_4 = 2; %Number of mixtures of Gaussians
Q_4 = 4; % Number of hidden states.
left_right_4 = 0; %Left-right architecture of the HMM
   model, 'yes' or 'no'
prior0_4 = normalise(rand(Q_4,1));% Initial guess of state
    probabilities
transmat0_4 = mk_stochastic(rand(Q_4,Q_4));% Initial guess
    of transition probabilities
[mu0_4, Sigma0_4] = mixgauss_init(Q_4*M_4, reshape(data_4,
    [O_4 T_4*nex_4]), 'full');
mu0_4 = reshape(mu0_4, [O_4 Q_4 M_4]);
Sigma0_4 = reshape(Sigma0_4, [O_4 O_4 Q_4 M_4]);
mixmat0_4 = mk_stochastic(rand(Q_4,M_4));
%Finally, let us improve these parameter estimates using
   Expectation Maximization Algorithm.
[LL_4, prior1_4, transmat1_4, mu1_4, Sigma1_4, mixmat1_4]
   = ...
mhmm_em(data_4, prior0_4, transmat0_4, mu0_4, Sigma0_4,
   mixmat0_4, 'max_iter', 40);

plot (LL_4) % Plotting the improvement of the Log
   Likelihood after 5 iterations. the learning curve.
```

```
xlabel ('Number of data strings')
ylabel ('Log-likelihood')

disp('Log-likelihood becomes consistent. BB_H Trained!')

%% Training for High Bit Bounce (TR_BB_M)
addpath(genpath('C:\Users\HMMall'))
data_5 = [TR_BB_M]';% Training Data High Bit Bounce
T_5 = size(data_5,2); % The number of observation
   sequences. In other words, How many data sample
   strings? or the number of raws
O_5 = size(data_5,1); % The number of sensor data in a
   given sequence i.e. Motor Current, Accelerometer, and
   ang speed or teh number of columns
nex_5 = 1; % the different layers of data in the 3D matrix
   . (May be the data from another similar process line)
M_5 = 2; %Number of mixtures of Gaussians
Q_5 = 4; % Number of hidden states.
left_right_5 = 0; %Left-right architecture of the HMM
   model, 'yes' or 'no'
prior0_5 = normalise(rand(Q_5,1));% Initial guess of state
    probabilities
transmat0_5 = mk_stochastic(rand(Q_5,Q_5));% Initial guess
    of transition probabilities
[mu0_5, Sigma0_5] = mixgauss_init(Q_5*M_5, reshape(data_5,
    [O_5 T_5*nex_5]), 'full');
mu0_5 = reshape(mu0_5, [O_5 Q_5 M_5]);
Sigma0_5 = reshape(Sigma0_5, [O_5 O_5 Q_5 M_5]);
mixmat0_5 = mk_stochastic(rand(Q_5,M_5));
%Finally, let us improve these parameter estimates using
   Expectation Maximization Algorithm.
[LL_5, prior1_5, transmat1_5, mu1_5, Sigma1_5, mixmat1_5]
   = ...
mhmm_em(data_5, prior0_5, transmat0_5, mu0_5, Sigma0_5,
   mixmat0_5, 'max_iter', 40);

plot (LL_5) % Plotting the improvement of the Log
   Likelihood after 5 iterations. the learning curve.
xlabel ('Number of data strings')
ylabel ('Log-likelihood')
%
disp('Log-likelihood becomes consistent. BB_M Trained!')
```

```
%
%% Training for Low Bit-Bounce (TR_BB_L)
addpath(genpath('C:\Users\HMMall'))
data_6 = [TR_BB_L]';% Training Data Low Bit-Bounce
T_6 = size(data_6,2); % The number of observation
   sequences. In other words, How many data sample
   strings? or the number of raws
O_6 = size(data_6,1); % The number of sensor data in a
   given sequence i.e. Motor Current, Accelerometer, and
   ang speed or teh number of columns
nex_6 = 1; % the different layers of data in the 3D matrix
   . (May be the data from another similar process line)
M_6 = 2; %Number of mixtures of Gaussians
Q_6 = 4; % Number of hidden states.
left_right_6 = 0; %Left-right architecture of the HMM
   model, 'yes' or 'no'
prior0_6 = normalise(rand(Q_6,1));% Initial guess of state
    probabilities
transmat0_6 = mk_stochastic(rand(Q_6,Q_6));% Initial guess
    of transition probabilities
[mu0_6, Sigma0_6] = mixgauss_init(Q_6*M_6, reshape(data_6,
    [O_6 T_6*nex_6]), 'full');
mu0_6 = reshape(mu0_6, [O_6 Q_6 M_6]);
Sigma0_6 = reshape(Sigma0_6, [O_6 O_6 Q_6 M_6]);
mixmat0_6 = mk_stochastic(rand(Q_6,M_6));
%Finally, let us improve these parameter estimates using
   Expectation Maximization Algorithm.
[LL_6, prior1_6, transmat1_6, mu1_6, Sigma1_6, mixmat1_6]
   = ...
mhmm_em(data_6, prior0_6, transmat0_6, mu0_6, Sigma0_6,
   mixmat0_6, 'max_iter', 40);

plot (LL_6) % Plotting the improvement of the Log
   Likelihood after 5 iterations. the learning curve.
xlabel ('Number of data strings')
ylabel ('Log-likelihood')

disp('Log-likelihood becomes consistent. BB_L Trained!')

%%%%%%%%%%%%%%%%%%%%%%%%%%%%%%%%%%%% Whirling (Forward) (
   WH) %%%%%%%%%%%%%%%%%%%%%%%%%%
```

```
%% Training for High Whirling (TR_WH_H)
addpath(genpath('C:\Users\HMMall'))
data_7 = [TR_WH_H]';% Training Data High Bit Bounce
T_7 = size(data_7,2); % The number of observation
   sequences. In other words, How many data sample
   strings? or the number of raws
O_7 = size(data_7,1); % The number of sensor data in a
   given sequence i.e. Motor Current, Accelerometer, and
   ang speed or teh number of columns
nex_7 = 1; % the different layers of data in the 3D matrix
   . (May be the data from another similar process line)
M_7 = 2; %Number of mixtures of Gaussians
Q_7 = 4; % Number of hidden states.
left_right_7 = 0; %Left-right architecture of the HMM
   model, 'yes' or 'no'
prior0_7 = normalise(rand(Q_7,1));% Initial guess of state
    probabilities
transmat0_7 = mk_stochastic(rand(Q_7,Q_7));% Initial guess
    of transition probabilities
[mu0_7, Sigma0_7] = mixgauss_init(Q_7*M_7, reshape(data_7,
    [O_7 T_7*nex_7]), 'full');
mu0_7 = reshape(mu0_7, [O_7 Q_7 M_7]);
Sigma0_7 = reshape(Sigma0_7, [O_7 O_7 Q_7 M_7]);
mixmat0_7 = mk_stochastic(rand(Q_7,M_7));
%Finally, let us improve these parameter estimates using
   Expectation Maximization Algorithm.
[LL_7, prior1_7, transmat1_7, mu1_7, Sigma1_7, mixmat1_7]
   = ...
mhmm_em(data_7, prior0_7, transmat0_7, mu0_7, Sigma0_7,
   mixmat0_7, 'max_iter', 40);

plot (LL_7) % Plotting the improvement of the Log
   Likelihood after 5 iterations. the learning curve.
xlabel ('Number of data strings')
ylabel ('Log-likelihood')

disp('Log-likelihood becomes consistent. WH_H Trained!')

%% Training for Medium Whirling  (TR_WH_M)
addpath(genpath('C:\Users\HMMall'))
data_8 = [TR_WH_M]';% Training Data Medium Whrling
T_8 = size(data_8,2); % The number of observation
```

```
   sequences. In other words, How many data sample
   strings? or the number of raws
O_8 = size(data_8,1); % The number of sensor data in a
   given sequence i.e. Motor Current, Accelerometer, and
   ang speed or teh number of columns
nex_8 = 1; % the different layers of data in the 3D matrix
   . (May be the data from another similar process line)
M_8 = 2; %Number of mixtures of Gaussians
Q_8 = 4; % Number of hidden states.
left_right_8 = 0; %Left-right architecture of the HMM
   model, 'yes' or 'no'
prior0_8 = normalise(rand(Q_8,1));% Initial guess of state
    probabilities
transmat0_8 = mk_stochastic(rand(Q_8,Q_8));% Initial guess
    of transition probabilities
[mu0_8, Sigma0_8] = mixgauss_init(Q_8*M_8, reshape(data_8,
    [O_8 T_8*nex_8]), 'full');
mu0_8 = reshape(mu0_8, [O_8 Q_8 M_8]);
Sigma0_8 = reshape(Sigma0_8, [O_8 O_8 Q_8 M_8]);
mixmat0_8 = mk_stochastic(rand(Q_8,M_8));
%Finally, let us improve these parameter estimates using
   Expectation Maximization Algorithm.
[LL_8, prior1_8, transmat1_8, mu1_8, Sigma1_8, mixmat1_8]
   = ...
mhmm_em(data_8, prior0_8, transmat0_8, mu0_8, Sigma0_8,
   mixmat0_8, 'max_iter', 40);

plot (LL_8) % Plotting the improvement of the Log
   Likelihood after 5 iterations. the learning curve.
xlabel ('Number of data strings')
ylabel ('Log-likelihood')

disp('Log-likelihood becomes consistent. WH_M Trained!')

%% Training for Low Whirling (TR_WH_L)
addpath(genpath('C:\Users\HMMall'))
data_9 = [TR_WH_L]';% Training Data Low Whirling
T_9 = size(data_9,2); % The number of observation
   sequences. In other words, How many data sample
   strings? or the number of raws
O_9 = size(data_9,1); % The number of sensor data in a
   given sequence i.e. Motor Current, Accelerometer, and
   ang speed or teh number of columns
```

```
nex_9 = 1; % the different layers of data in the 3D matrix. (May be the data from another similar process line)
M_9 = 2; %Number of mixtures of Gaussians
Q_9 = 4; % Number of hidden states.
left_right_9 = 0; %Left-right architecture of the HMM model, 'yes' or 'no'
prior0_9 = normalise(rand(Q_9,1));% Initial guess of state probabilities
transmat0_9 = mk_stochastic(rand(Q_9,Q_9));% Initial guess of transition probabilities
[mu0_9, Sigma0_9] = mixgauss_init(Q_9*M_9, reshape(data_9, [O_9 T_9*nex_9]), 'full');
mu0_9 = reshape(mu0_9, [O_9 Q_9 M_9]);
Sigma0_9 = reshape(Sigma0_9, [O_9 O_9 Q_9 M_9]);
mixmat0_9 = mk_stochastic(rand(Q_9,M_9));
%Finally, let us improve these parameter estimates using Expectation Maximization Algorithm.
[LL_9, prior1_9, transmat1_9, mu1_9, Sigma1_9, mixmat1_9] = ...
mhmm_em(data_9, prior0_9, transmat0_9, mu0_9, Sigma0_9, mixmat0_9, 'max_iter', 40);

plot (LL_9) % Plotting the improvement of the Log Likelihood after 5 iterations. the learning curve.
xlabel ('Number of data strings')
ylabel ('Log-likelihood')

disp('Log-likelihood becomes consistent. WH_L Trained!')


%% Vibration type and severity classification
%%%%%%%%%%%% Input the testing data here %%%%%%%%%%%%%%%%%%%%
testdata = [TST_SS_H(1:100,:)]';
% %%%%%%%%%%%%%%%%%%%%%%%%%%%%%%%%%%%%%%%%%%%%%%%%%%%%%%%%%%%

%%
LLike_1 = [];
for i=1:1:size(testdata,2)
loglik_1 = mhmm_logprob(testdata(:,i), prior1_1, transmat1_1, mu1_1, Sigma1_1, mixmat1_1);
```

```
LLike_1 = [LLike_1; loglik_1];
end

MEAN_1 = mean (LLike_1);
%%

LLike_2 = [];
for i=1:1:size(testdata,2)
loglik_2 = mhmm_logprob(testdata(:,i), prior1_2,
   transmat1_2, mu1_2, Sigma1_2, mixmat1_2);
LLike_2 = [LLike_2; loglik_2];
end

MEAN_2 = mean (LLike_2);
%%

LLike_3 = [];
for i=1:1:size(testdata,2)
loglik_3 = mhmm_logprob(testdata(:,i), prior1_3,
   transmat1_3, mu1_3, Sigma1_3, mixmat1_3);
LLike_3 = [LLike_3; loglik_3];
end

MEAN_3 = mean (LLike_3);
%%
LLike_4 = [];
for i=1:1:size(testdata,2)
loglik_4 = mhmm_logprob(testdata(:,i), prior1_4,
   transmat1_4, mu1_4, Sigma1_4, mixmat1_4);
LLike_4 = [LLike_4; loglik_4];
end

MEAN_4 = mean (LLike_4);
%%
LLike_5 = [];
for i=1:1:size(testdata,2)
loglik_5 = mhmm_logprob(testdata(:,i), prior1_5,
   transmat1_5, mu1_5, Sigma1_5, mixmat1_5);
LLike_5 = [LLike_5; loglik_5];
end

MEAN_5 = mean (LLike_5);
```

```
%%
LLike_6 = [];
for i=1:1:size(testdata,2)
loglik_6 = mhmm_logprob(testdata(:,i), prior1_6,
   transmat1_6, mu1_6, Sigma1_6, mixmat1_6);
LLike_6 = [LLike_6; loglik_6];
end

MEAN_6 = mean (LLike_6);
%%

LLike_7 = [];
for i=1:1:size(testdata,2)
loglik_7 = mhmm_logprob(testdata(:,i), prior1_7,
   transmat1_7, mu1_7, Sigma1_7, mixmat1_7);
LLike_7 = [LLike_7; loglik_7];
end

MEAN_7 = mean (LLike_7);
%%
LLike_8 = [];
for i=1:1:size(testdata,2)
loglik_8 = mhmm_logprob(testdata(:,i), prior1_8,
   transmat1_8, mu1_8, Sigma1_8, mixmat1_8);
LLike_8 = [LLike_8; loglik_8];
end

MEAN_8 = mean (LLike_8);
%%
LLike_9 = [];
for i=1:1:size(testdata,2)
loglik_9 = mhmm_logprob(testdata(:,i), prior1_9,
   transmat1_9, mu1_9, Sigma1_9, mixmat1_9);
LLike_9 = [LLike_9; loglik_9];
end

MEAN_9 = mean (LLike_9);
%%

MEANS = [MEAN_1 MEAN_2 MEAN_3 MEAN_4 MEAN_5 MEAN_6 MEAN_7
   MEAN_8 MEAN_8];

```

```
317 if max (MEANS) == MEAN_1
318     disp('Stick Slip - High')
319 end
320
321 if max (MEANS) == MEAN_2
322     disp('Stick Slip - Medium')
323 end
324
325 if max (MEANS) == MEAN_3
326     disp('Stick Slip - Low')
327 end
328
329 if max (MEANS) == MEAN_4
330     disp('Bit Bounce- High')
331 end
332
333 if max (MEANS) == MEAN_5
334     disp('Bit Bounce- Medium')
335 end
336
337 if max (MEANS) == MEAN_6
338     disp('Bit Bounce- Low')
339 end
340
341 if max (MEANS) == MEAN_7
342     disp('Whirling- High')
343 end
344
345 if max (MEANS) == MEAN_8
346     disp('Whirling- Medium')
347 end
348
349 if max (MEANS) == MEAN_9
350     disp('Whirling- Low')
351 end
352
353 figure(1)
354
355 subplot(3,3,1)
356 plot(LLike_1)
357 xlabel ('Number of data strings')
358 ylabel ('Log-likelihood')
```

```
359
360 subplot(3,3,2)
361 plot(LLike_2)
362 xlabel ('Number of data strings')
363 ylabel ('Log-likelihood')
364
365 subplot(3,3,3)
366 plot(LLike_3)
367 xlabel ('Number of data strings')
368 ylabel ('Log-likelihood')
369
370 subplot(3,3,4)
371 plot(LLike_4)
372 xlabel ('Number of data strings')
373 ylabel ('Log-likelihood')
374
375 subplot(3,3,5)
376 plot(LLike_5)
377 xlabel ('Number of data strings')
378 ylabel ('Log-likelihood')
379
380 subplot(3,3,6)
381 plot(LLike_6)
382 xlabel ('Number of data strings')
383 ylabel ('Log-likelihood')
384
385 subplot(3,3,7)
386 plot(LLike_7)
387 xlabel ('Number of data strings')
388 ylabel ('Log-likelihood')
389
390 subplot(3,3,8)
391 plot(LLike_8)
392 xlabel ('Number of data strings')
393 ylabel ('Log-likelihood')
394
395 subplot(3,3,9)
396 plot(LLike_9)
397 xlabel ('Number of data strings')
398 ylabel ('Log-likelihood')
```